공학박사학위논문

HYDROGEN SORPTION PROPERTIES OF $Ca(BH_4)_2$ AND $Ca(BH_4)_2 + MgH_2$ COMPOSITE

$Ca(BH_4)_2$와 $Ca(BH_4)_2$+ MgH_2의 수소 흡방출 특성연구

2013년 **2**월

서울대학교 대학원

재료공학부

김 윤 영

HYDROGEN SORPTION PROPERTIES OF $Ca(BH_4)_2$ AND $Ca(BH_4)_2$+MgH_2 COMPOSITE

$Ca(BH_4)_2$와 $Ca(BH_4)_2$+ MgH_2의 수소 흡방출 특성연구

지도교수 한 흥 남

이 논문을 공학박사학위논문으로 제출함
2012년 11월

서울대학교 대학원
재료공학부
김 윤 영

김윤영의 박사학위논문을 인준함
2012년 12월

위 원 장 오 규 환 (인)
부 위 원 장 한 흥 남 (인)
위 원 이 경 우 (인)
위 원 조 영 환 (인)
위 원 이 준 호 (인)

ABSTRACT

Light metal borohydrides are considered to be promising materials as solid state hydrogen storage due to their high hydrogen contents. Among them, $Ca(BH_4)_2$ has high gravimetric (11.5 wt%) and volumetric (~130 kg/m^3) hydrogen content. $Ca(BH_4)_2$ releases max. 9.6 wt% hydrogen assuming the following overall decomposition reaction:

$$Ca(BH_4)_2 \rightarrow 2/3\ CaH_2 + 1/3\ CaB_6 + 10/3\ H_2$$

However, the exact mechanism of dehydrogenation has not known yet. Several intermediate phases such as CaB_2H_x, amorphous phase(s), and $CaB_{12}H_{12}$ have been observed during the dehydrogenation of $Ca(BH_4)_2$. For that reason, we investigated here the dehydrogenation and rehydrogenation reactions of $Ca(BH_4)_2$ under precisely controlled experimental conditions (H_2 partial pressure and temperatures).

First, the dehydrogenation reaction pathway of $Ca(BH_4)_2$ has been investigated under an isobaric condition of 1 bar hydrogen. β-$Ca(BH_4)_2$ gradually transforms into amorphous phase at the initial decomposition stage. Upon further heating, it decomposes into CaB_2H_x or $CaB_{12}H_{12}$, indicating that there is a subtle competition between two different dehydrogenation routes; ⅰ) $Ca(BH_4)_2 \rightarrow$ amorphous phase $\rightarrow CaB_2H_x + (8\text{-}x)/2\ H_2 \rightarrow 2/3\ CaH_2 + 1/3\ CaB_6 + 10/3H_2$ and ⅱ) $Ca(BH_4)_2 \rightarrow$ amorphous phases $\rightarrow 1/6CaB_{12}H_{12} + 5/6$

CaH_2 + 13/6 H_2. Among dehydrogenated phases, CaB_2H_x as well as CaB_6 + CaH_2 mixture can be rehydrogenated at 330℃ under 90 bar hydrogen without any catalytic additive, whereas $CaB_{12}H_{12}$ hardly rehydrogenated under the same condition.

Second, during dehydrogenation of $Ca(BH_4)_2$, several intermediate phases such as an amorphous phase(s), CaB_2H_x, and $CaB_{12}H_{12}$ have been observed. Among intermediate phases, $CaB_{12}H_{12}$ is known as a relatively stable compound. If the formation of the very stable phases $CaB_{12}H_{12}$ can be avoided during dehydrogenation, $Ca(BH_4)_2$ can be fully rehydrogenated from CaH_2 and CaB_6 under mild conditions. To control the dehydrogenation reaction path and suppress the formation of the stable intermediate compounds, we apply three different hydrogen pressures during heating of $Ca(BH_4)_2$. The decomposition reaction of $Ca(BH_4)_2$ is sensitive to the H_2 back pressure. At 1 bar H_2 pressure, $Ca(BH_4)_2$ decomposes via two competitive dehydrogenation reaction routes to form CaB_2H_x or $CaB_{12}H_{12}$. At 20 bar hydrogen pressure, amorphous elemental boron is formed as a final dehydrogenation product and the formation of CaB_2H_x phases is suppressed. Three possible routes to form CaH_2 are also described in the present work.

Lastly, the dehydrogenation and rehydrogenation reactions of $Ca(BH_4)_2$ + MgH_2 composite were investigated under hydrogen back pressures. The dehydrogenation reaction sequence is: i) $6Ca(BH_4)_2 + 3MgH_2 \rightarrow$

$Ca4Mg_3H_{14} + 2CaB_6 + 20\ H_2$, ii) $Ca_4Mg_3H_{14} \rightarrow 4CaH_2 + 3\ Mg + 3H_2$. The rehydrogenation reactions takes place in reverse order, and about 60% reversibility was achieved after rehydrogenation for 24 h under 90 bar hydrogen pressure at 350 ℃ even without the help of catalysts.

From this study, the dehydrogenation and rehydrogenation reactions of $Ca(BH_4)_2$ and $Ca(BH_4)_2$+MgH_2 composite were clarified under several different hydrogen pressures. The suggested reactions are validated by crystallographic (XRD and in-situ XRD) and spectroscopic (FT-IR, Raman, and NMR) analyses on the various dehydrogenated samples and comparisons with calculation results.

Keywords: Hydrogen storage, calcium borohydrides, thermodynamic tuning, X-ray diffraction, in situ X-ray synchrotron powder diffraction, Infrared Spectrum, Raman Spectrum, Dehydrogenation reactions, Rehydrogenation reaction, Nuclear Magnetic Resonance Spectrum, Pressure-Component-Isotherm, Van't hoff equation, Hydrogen absorption, Hydrogen desorption

Student number: 2009-30147

Contents

Chapter 2

Dehydrogenation reactions of $Ca(BH_4)_2$

Chapter 4

Reversibility of rehydrogenation/dehydrogenation reactions of both $Ca(BH_4)_2$ and $Ca(BH_4)_2 + MgH_2$ composite

LIST OF TABLES

LIST OF FIGURES

380 °C. Symbols: #, ●, and * represent β-$Ca(BH_4)_2$, CaB_2H_x, and CaH_2, respectively.

Fig. 2.12. XRD patterns of as-received $Ca(BH_4)_2$ and samples dehydrogenated at 340, 345, 350, and 500 °C. β, cross, and inverted triangle symbols represent β-$Ca(BH_4)_2$, CaB_2H_x, and CaH_2, respectively.

Fig. 2.13. Raman spectra of $Ca(BH_4)_2$ after dehydrogenation under 1 bar H_2 pressure (a) at 345 °C and (b) at 500 °C. The Raman spectrum of CaB_6 reference is compared in (c).

Fig. 2.14. ^{11}B MAS NMR spectra of (a) as-received $Ca(BH_4)_2$, samples at dehydrogenated at (b) 340 °C, (c) 345 °C, (d) 350 °C, (e) 500 °C, and (f) spectrum (b) decomposed into four peaks. The spinning rate is 15 kHz.

Fig. 2. 15. Solution ^{11}B spectra of products resulting from dehydrogenated $Ca(BH_4)_2$ dissolved in aqueous solution showing various species formed during dehydrogenation and hydrolysis. (a) H-coupled ^{11}B NMR spectra and (b) H-decoupled ^{11}B NMR spectra of the dehydrogenated sample at 340 °C. The rehydrogenated sample (α-, β-$Ca(BH_4)_2$, amorphous phase, CaH_2, CaB_6, and $CaB_{12}H_{12}$) is dissolved in water. ^{11}B NMR spectra are measured at different time after mixing water: (c) 7 hours, (d) 2 hours, and (e) 0 hour.

Fig. 2. 16. *In situ* SR-PXD of $Ca(BH_4)_2$ in the temperature 310-400 °C under (a) 10 bar H_2, and (b) 20 bar H_2. Symbols; #, ●, and ● represent β-$Ca(BH_4)_2$, CaB_2H_x and CaH_2, respectively.

Fig. 2. 17. Normalized intensities of the *in situ* SR-PXD data measured for $Ca(BH_4)_2$ under three different pressures. The open circles, triangles, and solid cicles represent measurements under $p(H_2)$ = 1, 10, and 20 bar, respectively. Additionally, the black, blue, and red lines represent the quantity of the β-$Ca(BH_4)_2$,CaB_2H_x, and CaH_2 phases, respectively.

Fig. 2. 18. *Ex situ* XRD data of four dehydrogenated samples at 420 °C under (a) $p(H_2)$= 1 bar, (b) $p(H_2)$=5 bar, (c) $p(H_2)$=10 bar, and (d) $p(H_2)$ = 20 bar.

Fig. 2. 19. (A) NMR data of three dehydrogenated samples at 420 °C under (a) $p(H_2)$=1 bar, (b) $p(H_2)$=5 bar, (c) $p(H_2)$=10 bar, and (d) $p(H_2)$=20 bar. Broken lines represent ^{11}B CPMAS NMR spectra obtained using 0.075 ms of cross polarization contact time. (B) Relative composition of boron species obtained from the spectral decomposition of ^{11}B spectra in (A) as a function of hydrogen back pressure in the thermal decomposition of $Ca(BH_4)_2$.

Fig. 2. 20. ^{11}B MAS NMR spectra with the decomposition into CaB_6 (broken line at 14 ppm), elemental boron (blue solid line at 4.5 ppm and -16 ppm),

Fig. 4.2. DSC curves of the first dehydrogenation of (a) $Ca(BH_4)_2 + MgH_2$ and (b) $Ca(BH_4)_2$ + 0.2 Mg composite. TGA curves of (c) first and (d) second dehydrogenation of $Ca(BH_4)_2$ composite; rehydrogenation was done under 90 bar H_2 pressure at 350 °C for 24 h.

Fig. 4.3. Room temperature XRD patterns of mixed $CaH_2 + CaB_6$ + Mg samples that had been heated under 90 bar H_2 at 350 °C for different durations.

Fig. 4.4. TG curves of samples 2,3, and 4 were given together with the $Ca(BH_4)_2 + MgH_2$ mixture.

Fig. 4.5. Raman spectra of (a) sample 1 dehrogenated at 450 °C, (b) sample 2 dehydrogenated at 400 °C, (c) sample 2 hydrogenated at 350 °C, and (d) reference CaB_6

Fig. 4.6. XRD pattern after rehydrogenation at 90 bar of hydrogen and 330 °C for 24h. The sample was initially dehydrogenated at 345 °C. Symbols α and β represent α- and β-$Ca(BH_4)_2$, respectively. The inverted triangle and cross symbols represent CaH_2 and $Ca_3(BH_4)_3(BO_3)$, respectively.

Fig. 4.7. ^{11}B MAS NMR spectra of (a) β- $Ca(BH_4)_2$, (b)after desorption, and c)after reabsorption.

Chapter 1

Introduction

1.1. Hydrogen : a clean & sustainable energy carrier

The worldwide average energy consumption is approximately 1.2×10^{14} kWh/year.[1] The energy consumption for last four decades is shown in Figure 1.1. The world energy consumption have increased continuously from 1860 to today, and more than 80 % of the energy consumption depends on fossil fuel, such as oil, coal, and gas. However, the amount of energy stored in fossile fuel is about 2.5×10^{13} kWh,[2] which means that the world is facing energy shortage. Furthermore, the consumption of fossil fuels leads to the formation of greenhouse gas, CO_2, and it is now widely accepted that this may give rise to an increase in the average temperature of the earth and to climatic change. For these reasons, so many other alternative sources of energy such as solar, wind, geothermal, tides, nuclear, and hydrogen have been researched.

Among alternative energy sources, hydrogen is considered a promising future energy carrier due to its high abundance, light weight, and a high energy density by weight. However, only less than 1% of hyodrogen exists as a molecular hydrogen gas H_2 in the air. So, most of the hydrogen we

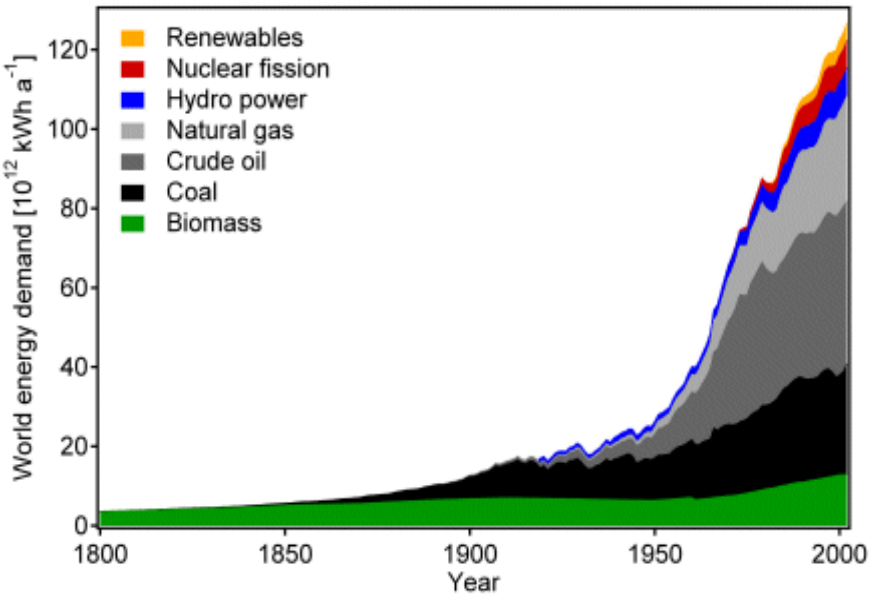

Fig. 1.1. Worldwide annual energy consumption for last four decades[3]

use are obtained from hydrocarbons through a process known as reforming. Many other methods of hydrogen production are known including electrolysis, thermolysis, photocatalytic, photobiological, and biocatalysed electrolysis. This isolated hydrogen can be storaged in the form as a gas, liquid, or solid type such as chemical compound, and then converted into energy through fuel cells. Fuel cells are characterized by their electrolyte, operating temperature, and level of hydrogen purity required. Among fuel cells, proton exchange membrane fuel cells (PEMFC) are developed for use in tranportaion, stationary, and portable application, and its operating temperature ranges from 60 to 100 °C. Operating fuel cell is quiet and has high efficiencies and environmental advantage. For these reasons, the development of hydrogen storage desorbing and absorbing hydrogen at an operating temperature of PEMFC is required.

Hydrogen society, including hydrogen production-hydrogen storage-fuel cell, could be a key to a clean, sustainable energy system. The infrastructure of hydrogen energy is shown in Figure 1.2. The use of hydrogen as an energy carrier requires development in several parts, including production, delivery, storage, conversion, and end-use. To transfer to a hydrogen economy, all technological advances are required at the same time, but a major challenge in a future 'hydrogen economy' is the development of safe, compact, and efficient means of hydrogen storage.[4] Most research into

hydrogen storage is focused on storing hydrogen as a lightweight, compact energy carrier for mobile applications.

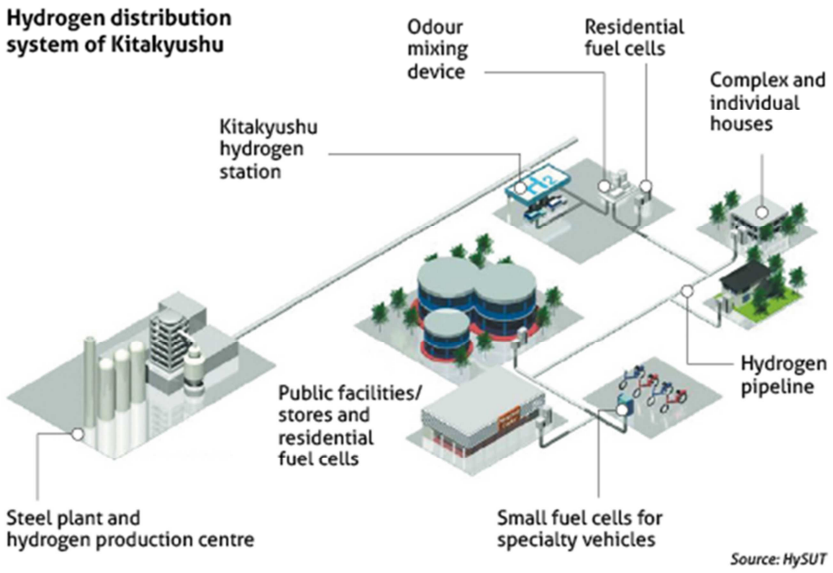

Fig. 1.2. Hydrogen energy social infrastructure of a hydrogen society[5]

1.2. Hydrogen Storage

Hydrogen, the lightese element, has a large gravimetric energy density of 120 MJ/kg, which is approximately three times higher than that of gasoline. The volumetric energy densities of hydrogen are 0.089 and 71 g/L, at 25 and -252 ˚C in gaseous and liquid state, respectively.[6] Volumetric and gravimetric hydrogen densities of different hydrogen storage forms are shown in Figure 1.3. Hydrogen can be stored in three forms; gas, liquid or a solid combined with a metal hydride. Conventional method of storing hydrogen is compressed hydrogen storage, but the gravimetric density of gaseous hydrogens is lowerd when compressed pressure is increased because hydrogen tank is heavier. Furthermore, the volumetric densities of gaseous hydrogen can not exceed those of liquid hydrogen. In the past, liquid hydrogen was also regarded to be a viable option for the automobile. However, due to cryogenic storage, liquefaction requires a large energy loss, and to prevent boil off, the related technology challenges could not be solved satisfyingly. Therefore, physical storage of high pressure and liquid are not suitable way for a practical vehicular application due to their low energy density and also due to safety reasons associated with them. On the other hand, solid state hydrogen storage is advantageous concerning safety and density compared to the liquid and compressed gas technology.

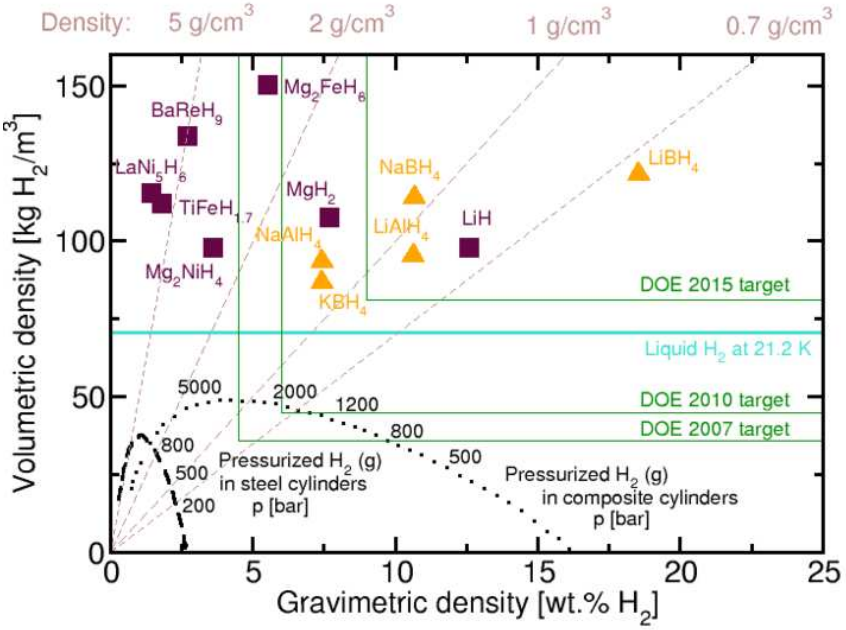

Fig. 1.3. Volumetric and gravimetric hydrogen densities of different hydrogen storage forms[7]

1.3. Solid Hydrogen Storage

1.3.1. Metal Hydrides and Complex hydrides

Metal hydrides are promising candidates for many stationary and mobile hydrogen storage applications. The main advantages of storing hydrogen in a metal hydride are the high hydrogen volumetric densities and the possibility to absorb and desorb hydrogen with a small change in hydrogen pressure.[8] However, even though the first metal hydride was discovered more than 100 years ago, intensive research on this class of materials is relatively new. Recently, a number of review papers have been published targeted on metal hydrides for hydrogen storage.[9-23]

Simple binary metal hydrides can be grouped into three basic types according to the nature of the metal-hydrogen bond[24] as follows: ionic, covalent, and metallic hydrides. Ionic hydrides include the binary hydrides of all alkali metals, or of alkaline earth metals from calcium through barium.[25] In general, the binary ionic hydrides are too stable for hydrogen storage application. Among these compounds, however, magnesium hydride is not a completely ionic hydride, and the interaction between hydrogen and magnesium is partly ionic and partly covalent. Thus, magnesium hydride should be considered to be a transition hydride between ionic and covalent hydrides, and has relatively lower thermal stability than other ionic binary hydrides. So, magnesium hydride has been studied as a candidate for

hydrogen storage material.[26] Covalent hydrides such as carbonhydrides and ammonia are liquid or gaseous at room temperature and those that are solid are thermally unstable.[27] These hydrides are not considered as a hydrogen storage material, because it is difficult to break covalent bond in compounds. Metallic hydrides are formed by transition metals including the rare earth and actinide series. In these hydrides, hydrogen acts as a metal and forms a metallic bond. They have high thermal and electrical conductivities, but are not suitable for a hydrogen storage application due to their low hydrogen contents.

Complex hydrides are salt-like materials in which hydrogen is covalently bound to the central atoms, in this way a crystal structure consisting of so-call “complex anions” is formed. Complex metal hydrides have been known for more than 50 years, but for many years they were not considered for reversible hydrogen storage due to the high kinetic barriers of the decomposition requiring high temperatures. However, since Bogdanovic and Schwickardi[28] discovered that the kinetic barrier of the decomposition of the complex metal hydride, $NaAlH_4$, can be lowered by the addition of Ti catalysts and that these materials become reversibly close to acceptable technical conditions, complex hydrides intensively researched. Complex hydrides such as $M_x(BH_4)_y$ or $M_m(AlH_4)_n$ have been intensively investigate as the hydrogen storage materials. Unfortunately, so far, most tetrahydroborates show rather sluggish kinetics and poor reversibility. The slow kinetics is

linked to the high energy barrier that needs to be overcome to break or (re)form the strong B-H bond within the [BH_4^-] anion. So, it is important to understand the exact dehydrogenation and control the reaction paths for applications.

1.3.2. Thermodynamic Assessment of Hydrides

As most of the hydrides are formed by direct reaction with gaseous hydrogen, it is important point to discuss the thermodynamics of hydride formation. When exposed to hydrogen, a hydride-forming metal (M) will form a metal hydride following the reaction:

$$M + x/2\ H_2 \leftrightarrow MH + Q$$

Q is the heat of reaction of hydride formation. The thermodynamic aspect of this reaction is conveniently described experimentally by pressure-composition isotherms (PCI). A schematic PCI curve[29] is shown in Figure 1.4. At low concentration, hydrogen first dissolves in the metal lattice and forms a solid solution phase (α phase). Hydrogen is then randomly distributed in the metal host lattice and the concentration varies slowly with temperature. The α phase has the same crystal structure as the bare metal. At the hydrogen pressure increases, the concentration also increases until the attractive H-H interaction becomes important.[30] At this point, nucleation of a higher concentration phase (β phase) occurs. The system now has three phase (α, β, and hydrogen gas) and two components (metal and hydrogen). The equilibrium pressure P_{eq} at the α→β phase transformation is given by the Van't Hoff law.

$$\ln P_0 = -\frac{\Delta S^0}{R} + \frac{\Delta H^0}{RT}.$$

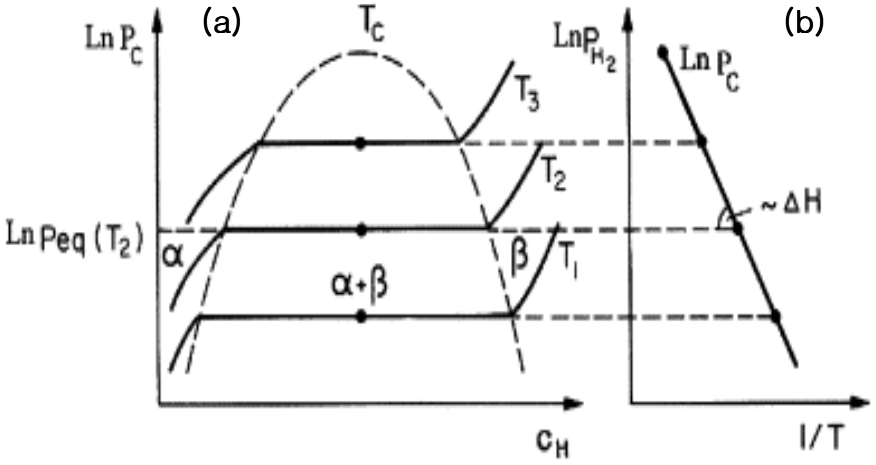

Fig. 1.4. (a) Schematic of a pressure-composition isotherm: α is the solid solution of hydrogen β is the hydride phase. (b) Van't Hoff plot giving the P_o, ΔH_o, and ΔS_o are, respectively, the equilibrium pressure, enthalpy, and entropy of the α→β transition.

So, we can plot Van't Hoff curve for measuring P_{eq} at least at three temperatures of PCI curves. The slope at this curve means the enthalpy change of the corresponding reaction. In general, the entropy change is mainly given by the loss of standard entropy of the hydrogen gas as it enters the metal lattices. This means that the entropy term does not depend significantly on the nature of the metal and that the ΔS term can be considered almost constant.[31] The entropies of metal borohydrides, for example, are the range of 100-120 J/K mol H_2. Among the methods for the estimation of enthalpy, PCI curve is the best way to measure the enthalpy of transition experimentally. However, the complex phenomenon, such as hysteresis or plateau slope, is usually observed in a "real" PCI curve. Metal borohydrides, especially, shows the slow kinetic in rehydrogenation reactions, which can produce a hysteresis. Another methods to measure the enthalpy of transition experimentally is using DSC by integrating the peak corresponding to a given transition. However, the estimation of enthalpy change in the case of involving several rections at the same time could be hard. Using first-principles calculations, the thermodynamical stabilities for the series of metal borohydrides have been systematically investigated.[32] Recently, Miwa et al.[33] reported that the bonding characteristics and the properties of metal borohydrides system strongly depend on the electronegativity difference between the metal atom and boron, which agrees well with the calculated results by using DFT and

SGTE. However, because first-principle calculation has also its own limitation, it is required the enthalpy of transition is estimated by combining above mentioned three methods.

1.3.3. Kinetic Assessment of Hydrides

A very important problem for practical applications of metal hydrides is the fact that the surfaces of metals are usually covered with oxide of various thicknesses, depending on the formation process of each particular metal. This will most probably be the case for all industrial means of production of metal hydrides. This oxide layer acts as a hydrogen barrier and must be broken in order for the gaseous hydrogen to access the bare metal. Therefore, the first hydrogenation is usually performed at high temperature and hydrogen pressure in order to force the hydrogen through the oxide layer. Upon hydrogenation, the lattice volume increases significantly. This expansion-contraction breaks the metal particles, exposing fresh metal surface and reducing particle size.[31]

For complex borohydrides, the evaluation of the activation energy (Ea) of solid state reaction is usually performed by a Kissinger plot[34] :

$$\ln\left(\frac{\beta}{T_p^2}\right) = \text{Const.} - \frac{E}{RT_p}$$

where T_p is the temperature at the maximum of the decomposition rate, β is scanning rate, and R is the gas constant. However, in many cases, several dehydrogenation routs occur at the same time during heating complex borohydrides, thus, this method shold be carefully used.

1.4. Thesis Motivations

Light metal borohydrides are considered to be promising materials as solid state hydrogen storage due to their high hydrogen content. Among them, $Ca(BH_4)_2$ has high gravimetric (11.5 wt%) and volumetric (~130 kg/m^3) hydrogen content. However, the exact mechanism of dehydrogenation of $Ca(BH_4)_2$ is still controversial. The possible dehydrogenation reactions of $Ca(BH_4)_2$ are listed as follows:

$$Ca(BH_4)_2 \rightarrow CaH_2 + 2\,B + 3\,H_2$$

$$Ca(BH_4)_2 \rightarrow 2/3\,CaH_2 + 1/3\,CaB_6 + 10/3\,H_2$$

$$Ca(BH_4)_2 \rightarrow 1/6\,CaB_{12}H_{12} + 5/6\,CaH_2 + 13/6\,H_2$$

CaH_2 has been commonly observed in the final dehydrogenation products, but several intermediate phases such as CaB_2H_x, amorphous phase(s), and $CaB_{12}H_{12}$ have been observed during the dehydrogenation of $Ca(BH_4)_2$. In the previous literature, no uniform experimental protocol has been proposed for this complex hydride, so widely different experimental dehydrogenation conditions (H_2 partial pressures and temperatures) have been investigated.[2, 35-42] We believe that this is one possible reason why different reaction intermediate phases were observed. The pressure control that most studies have employed is dehydrogenation under dynamic or static vacuum, which may not be a well-defined or suitable condition. For that reason, we investigated here the dehydrogenation reactions of $Ca(BH_4)_2$ under precisely

controlled experimental conditions (H_2 partial pressure and temperatures)

In this study, first, the dehydrogenation reaction pathway of $Ca(BH_4)_2$ has been investigated under an isobaric condition of 1 bar hydrogen. Furthermore, to control the dehydrogenation reaction path and suppress the formation of the stable intermediate compounds, we apply three different hydrogen pressures. The decomposition reactions of $Ca(BH_4)_2$ under different hydrogen pressure are also investigated. The reaction routes to form final dehydrogenation and therdynamic assessment for the theese reaction routes are also described in the present work.

Second, since no single metal hydride could be found that satisfies both the energy density and efficiency criteria, research has been concentrated on reactive hydride composite. In this respect, the unique kinetic property of MgB_2 has been reported.[43-45] Barkhordarian et al.[46] successfully obtained $Ca(BH_4)_2$+MgH_2 starting from CaH_2+MgB_2. However, upon dehydrogenation, Mg instead of MgB_2 was produced implying that the unique kinetic effect of MgB_2 might not be easily maintained during cycling. Therefore, the dehydrogenation routes of $Ca(BH_4)_2$ + MgH_2 composite is investigated in this study, and the experimental conditions are controlled systematically.

For borohydrides, it is often the case that reversibility is dominated by slow kinetics even without thermodynamic restriction. One of the routes to enhance kinetics is by reducing particle size or changing morphology. Smaller

particle size will naturally provide larger area for the reactions to proceed, and in extreme cases, such as nanoconfinement could even modify thermodynamics. To control the particle size is not an obvious task since each and every step, e.g., ball-milling conditions, reaction temperature and time, could all play a role in determining the final particle size. Therefore, we investigated on how the reaction kinetics is affected by changing reaction conditions together with clarifying the rehydrogenation reaction path.

Chapter 2

Dehydrogenation Reactions of $Ca(BH_4)_2$

2.1. Introduction

Light metal borohydrides are considered promising materials for solid-state hydrogen storage due to their high hydrogen content. For borohydrides, however, slow kinetics poses a more serious problem compared to alanates since B-B (T_m = 2076 °C) bonding is strong, and one can easily suppose that once B-B bonding is formed it would be very difficult to regenerate to the $[BH_4^-]$ unit. For example, rehydrogenation of LiH + B to reproduce $LiBH_4$ has been carried out at 600 °C and under a hydrogen pressure of higher than 150 bar.[47, 48] Interestingly, the approach to introduce a second compound to control the thermodynamics of hydrogen absorption and desorption offers a way to improve reversibility by changing the dehydrogenated products.[49] The case of $LiBH_4$ is a good example: in its pristine form, LiH and amorphous B[47, 50] is formed after dehydrogenation, and rehydrogenation is only possible under very high temperature and pressure conditions. However, when a second compound, such as MgH_2, Al, CaH_2, and CeH_2, is mixed together, boron combines with the metal in the second compound to form diborides (MgB_2, or AlB_2) or hexaborides (CaB_6 or CeB_6) instead of a-B, and

reversibility improves significantly as a result.[51-57] For this reason, it is of great importance to identify the products of dehydrogenation.

$Ca(BH_4)_2$ has high gravimetric (11.5 wt%) and volumetric (130 kg/m^3) hydrogen content. However, the actual dehydrogenation reaction pathway is still controversial. The two most likely dehydrogenation paths of $Ca(BH_4)_2$ are the following:

$$Ca(BH_4)_2 \rightarrow 2/3\ CaH_2 + 1/3\ CaB_6 + 10/3\ H_2 \qquad 9.6\ wt\ \%\ H_2 \qquad (1)$$

$$Ca(BH_4)_2 \rightarrow CaH_2 + 2B + 3H_2 \qquad 8.7\ wt\ \%\ H_2 \qquad (2)$$

To our knowledge, the final form of boron has never been identified experimentally. The amount of hydrogen relased serves as an indirect evidence of formation of CaB_6.[58, 59] Furthermore, several intermediate phases, such as CaB_2H_x,[59-61] and $CaB_{12}H_{12}$,[62] have been observed during the thermal dehydrogenation of $Ca(BH_4)_2$. Interestingly, both intermediate phases have not been observed simultaneously or consecutively during the dehydrogenation of $Ca(BH_4)_2$. Note that, in the literature, no uniform experimental protocol has been propsed for this complex hydride, so widely different experimental dehydrogenation conditions (H_2 partial pressures and temperatues) have been investigated. We believe that this is one possible reason why different reaction intermediate phses were observed. The pressure control that most studies have employed in the pase is dehydrogenation under dynamic or static vacuum, which may not be a well-defined or suitable condition.

In this study, we explore the dehydrogenation reactions of $Ca(BH_4)_2$ under isobaric conditions. Based on experimental results and theoretical calculations, we identify the dehydrogenated product of $Ca(BH_4)_2$ and discuss possible decomposition routes. The analysis of dehydrogenated samples is performed using various characterization techniques such as, *in situ* synchrotron powder X-ray diffraction (SR-PXD), *ex situ* X-ray diffraction (XRD), nuclear magnetic resonance (NMR), Raman spectroscopy, IR spectroscopy, thermogravimetric analysis (TGA), differential scanning calorimetry (DSC), and mass spectroscopy (MS).

2.2. Experimental Procedure

2.2.1. Sample Preparation

$Ca(BH_4)_2 \cdot 2THF$ (assay 98 %, Sigma-Aldrich) was used as a starting material. The powder was handled in an argon-filled glovebox (LAB star, MBraun or Woosung Hi-Vac) where water and oxygen levels were kept below 1 ppm. Adduct-free $Ca(BH_4)_2$ was prepared by drying the commercial powder at around 100 °C. This process usually produces a mixture of α- and γ-$Ca(BH_4)_2$ with a small fraction of β-$Ca(BH_4)_2$. Drying at higher temperature at around 200 °C gives mostly β-$Ca(BH_4)_2$. The dehydrogenated samples of $Ca(BH_4)_2$ was obtained using a Sievert's apparatus. One hundred milligrams of $Ca(BH_4)_2$ was charged into a stainless steel tube reator. The temperature was raised to the target point with a scanning rate of 0.2 °C/min. An isobaric condition was maintained during the dehydrogenation reaction.

2.2.2. Crystallographic and Spectroscopic Analysis

In situ synchrotron radiation powder X-ray diffraction (SR-PXD) measurements were carried out at the 10B XRD KIST-PAL beamline in the Pohang Accelerator Laboratory (Pohang, Korea). The selected X-ray wavelength was 1.00001 Å, and sapphire capillary tubes with a 1.07 mm inner diameter were used. $Ca(BH_4)_2$ samples were heated from room temperature to

300 °C in 30 minutes and then heated to 420 °C at a rate of 0.2 °C/min. The hydrogen pressure of each sample was maintained at 1, 10, and 20 bar during measurements, respectively. XRD patterns were collected every 147 s during the *in situ* measurements using a MAR 345 image plate detector. The two-dimensional (2D) images were converted into normal diffraction patterns by the FIT2D program. *Ex situ* XRD data were obtained at room temperature using a Bruker D8 Advance powder diffractometer with Cu Kα radiation (1.5418 Å) and a focusing Göbel mirror. Two types of sample holders were used. A dome-shaped, vacuum tight, sample holder was used to measure the dehydrogenated samples. To prevent air exposure of the samples, borosilicate capillary tubes with 0.7 mm inner diameter were also used. XRD data were analyzed by Rietveld refinement using the TOPAS and EVA software.[63]

Raman spectroscopy was performed on the dehydrogenated samples at room temperature usinga Renishaw InVia reflex spectrometer, with a 633 nm excitation laser, and an Instec HCS621V sample hotstatge that allowed inert loading. The Raman spectrum of CaB_6 (Sigma-Aldrich) was obtained and used as a reference. The Reman measurements were done by collatorate work with Birmingham University.

Solid state nuclear magnetic resonance (NMR) experiments were performed using a Bruker DSX-500 spectrometer and a boron free Bruker 4 mm magic angle spinning (MAS) probe. Samples in powder form were

packed into 4 mm ZrO_2 rotors and were sealed with tightly fitting kel-F caps inside of an Ar-filled glovebox. Sample spinning was performed under dry nitrogen gas to avoid exposure to oxygen or moisture. ^{11}B MAS NMR spectra were recorded after a short $\pi/12$ pulse with strong ^{1}H decoupling at a spinning rate of 15 kHz. The operating frequency of ^{1}H and ^{11}B MAS NMR spectra was 500.2 and 160.5 MHz respectively. ^{11}B cross-polarization (CP) MAS experiments were performed using weak radio frequency (rf) pulse powers for the Harman-Hahn matching condition as described in the literature.[64] The spectra were referenced to external standards of tetramethylsilane (TMS) for ^{1}H and $BF_3 \cdot O(CH_2CH_3)_2$ at 0 ppm for ^{11}B nuclei. The measurement was performed by the collaborate work with California Institute of Technology.

Fourier Transfer - Infrared Spectra (FT-IR) were collected using Bruker ALPHA FT-IR spectrometer. The measurements were done in an argon-filled glovebox. The FT-IR spectra waere analyzed by using a OPUS software.

Mass spectrometry (Metzsch QMS 403 C) was carried out to analyze the gas during heating samples. Mass spectrometer was coupled with TGA, and ca. 3 mg of samples was loaded into Al crucible.

2.2.3. Thermal analysis

The dehydrogenation paths of the samples were characterized using a differential scanning calorimeter (Netzsch HP-DSC Phonix) and a thermogravimetric analyzer (Netzsch TG 209 F1). For both differential scanning calorimetry (DSC) and thermogravimetric analysis (TGA), ca. 3 mg of sample was heated to 500 ˚C at a scanning rate of 2 or 5 ˚C/min under flowing argon conditions (assay 99.9999 %, 50 mL/min).

2.3. Polymorphs of $Ca(BH_4)_2$

To prepare pure $Ca(BH_4)_2$, commercially available $Ca(BH_4)_2 \cdot 2THF$ is desolvated by heating under vacuum. Removing adducted tetrahydrofuran (THF) molecules is performed based on the TG result of $Ca(BH_4)_2 \cdot 2THF$. (see Figure 2.1) The reactions occur in two steps as follows:

$$Ca(BH_4)_2 \cdot 2THF \rightarrow Ca(BH_4)_2 \cdot THF \rightarrow Ca(BH_4)_2 \qquad (3)$$

Two THF molecules were removed consecutively at 100 °C, and 170 °C, respectively. The THF removing procedures seem to be simple reactions, but the reaction is so sensitive that the powders easily jumped up during a vacuum heating of $Ca(BH_4)_2 \cdot 2THF$. In this case, some organic residues could remain in the sample, and due to this organic molecules, the dehydrogenation reaction routes can be changed by forming unexpected products, such as $Ca_3(BH_4)_3(BO_3)$.[65] Figure 2.2 shows the XRD and NMR data of an oxidezed phase observed during dehydrogenation of $Ca(BH_4)_2$. This material has not been reported before, so the structure and chemical formula of material was unknown. Figure 2.3 represents the XRD and NMR data of recently resolved structure[65] of $Ca_3(BH_4)_3(BO_3)$. ^{11}B NMR of the oxide should not be much different from the rest of oxide signal, appearing as broad peaks near 20 – 0 ppm range. Note that the sharp peak at 0 ppm is tetrahedral boron oxides, such as $Ca[B(OH)_4]_2$. By comparing ^{11}B MAS NMR of two oxides (trigonally coordinated), it is possible to extract a shape of BO_3 of

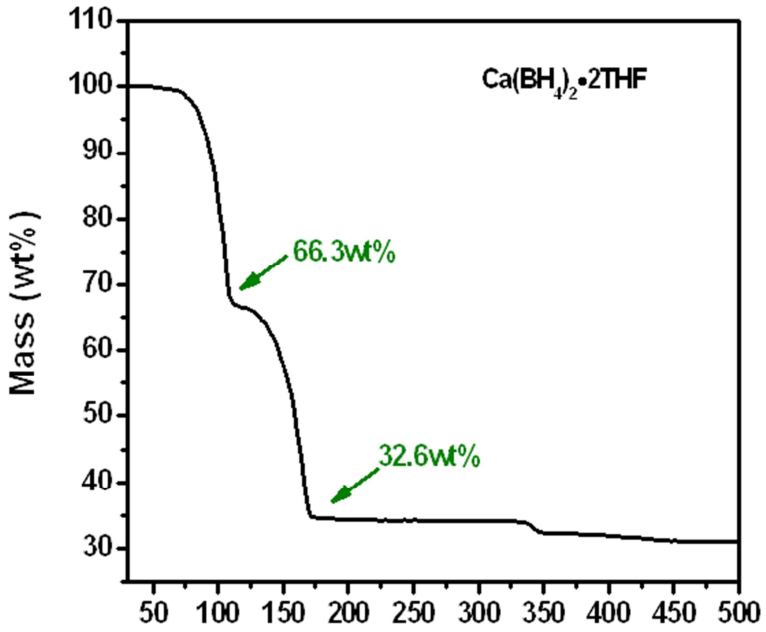

Fig. 2.1. TG curve of $Ca(BH_4)_2 \cdot 2THF$ is measured with flowing 50 mL/min Ar. The sample was heated to 500 °C at a scanning rate of 2 °C /min.

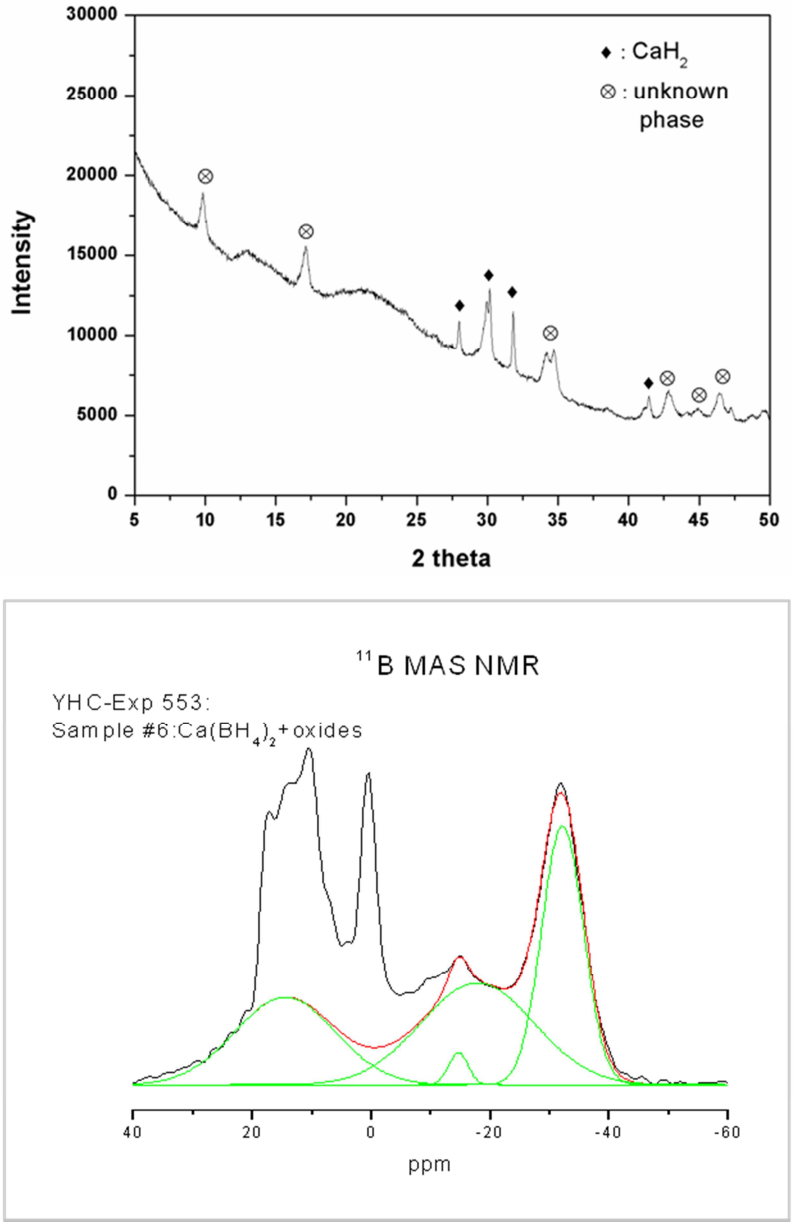

Fig. 2.2. XRD and NMR data of an unknown phase observed during the dehydrogenation of $Ca(BH_4)_2$

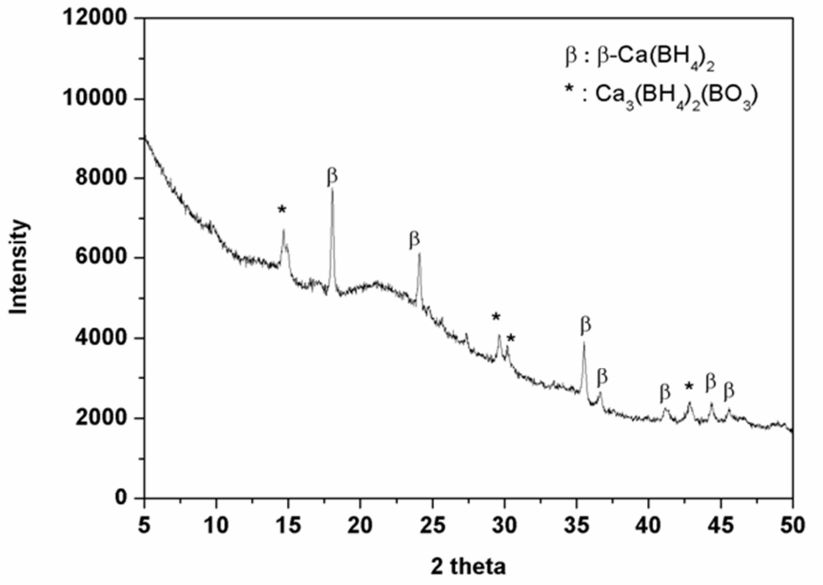

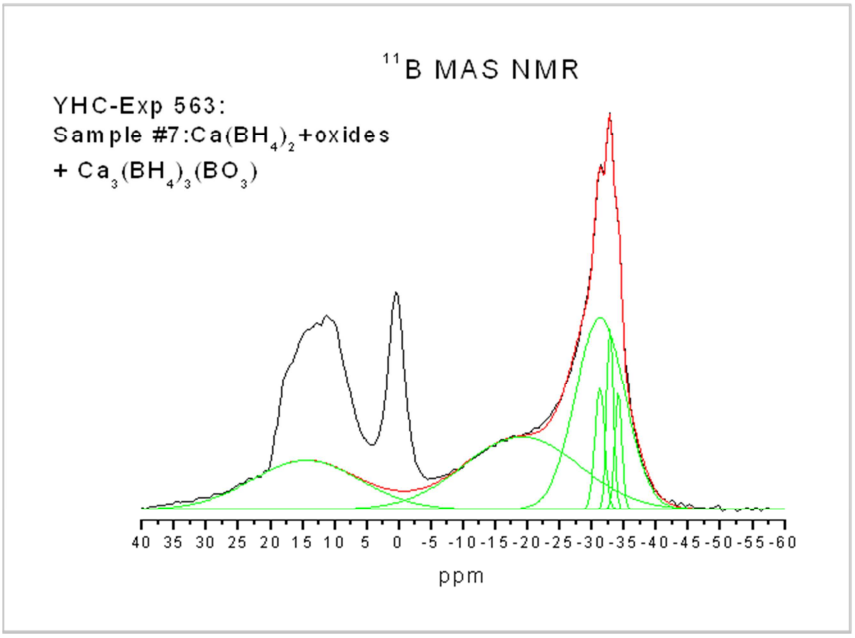

Fig. 2.3. XRD and NMR data of $Ca_3(BH_4)_3(BO_3)$ observed during the dehydrogenation of $Ca(BH_4)_2$

$Ca_3(BH_4)_3(BO_3)$.

The green spectrum excluding the 0 ppm peak can be a tentative shape representing BO_3 unit, appearing as planar geometry. However, it should be further investigated with a pure form of the material (if possible). As shown in Figure 2.2 and 2.3, the signals at around 20-0 ppm of both NMR spectra is the evidence of the existence of B-O bonding in samples, while the presence of B-H bonding also confirms from the peaks at -20~-40 ppm. The results tell the formation of partially oxidized phases, and in this case, the intermediate phase, CaB_2H_x, was not detected, indicating that the dehydrogenation path was changed.

As discussed above, although the sample contains a small amount of oxygen, it may cause confusion understanding the dehydrogenation reactions of material. Therefore, a slow heating rate of 1 °C/min and maintaining a pressure of 5×10^{-2} torr are required when we prepare pure $Ca(BH_4)_2$ samples.

Figure 2.4 shows a two-step reaction of removing the coordinated THF molecules from $Ca(BH_4)_2\cdot2THF$. The structure of materials is changed by the number of coordinated THF molecules. As shown Figure 2.4c, although XRD pattern presents adduct free $Ca(BH_4)_2$, some organic molecules could be remained in the sample. To conform adduct-free $Ca(BH_4)_2$, FT-IR was measured. (Figure 2.5) IR modes caused by the THF adduct are clearly observed at around 600 - 900 and 2800 – 3000 cm^{-1}. Other major peaks are

found from 2200 to 2500 cm^{-1}, which can be assigned to internal B-H stretching vibration of BH_4 complex.[66-68] On the other hand, IR modes orginated from the THF adduct disappear for the dryed $Ca(BH_4)_2$ sample, keeping the IR peaks around 2200-2500 cm^{-1}. This indicated that the purification process successfully removes the THF adduct from the purchase sample. IR spectra observed at around 100-1400 cm^{-1} for dried $Ca(BH_4)_2$ are due to internal B-H bending vibrations of BH_4, which overlap with those of the THF adduct in $Ca(BH_4)_2 \cdot 2THF$. [66-68]

XRD patterns of purified $Ca(BH_4)_2$ are shown in Figure 2.6. Four different polymorphs[69-72] of $Ca(BH_4)_2$ have been reported up to now, which complicate and are not fully understood. The structure of the low-temperature α-$Ca(BH_4)_2$ phase was resolved by Miwa *et al.,*[67] who assigned it to the face-centered orthorhombic *Fddd* symmetry group. Recently, Buchter et al. resolved the structure of the high-temperature β-$Ca(BH_4)_2$ phase,[70] they assigned it the space-group $P4_2/m$. Another polymorph designated γ-$Ca(BH_4)_2$ has also been observed at room temperature.[66, 70, 73] The space group of γ-$Ca(BH_4)_2$ has been reported as *Pbca*,[70] but there have been no reports to date of the full crystal structure for this phase. Flinchuk et al.[71] recently identified another polymorph α'-$Ca(BH_4)_2$, which forms to β-$Ca(BH_4)_2$ at elevated temperature.

Our experimental results tell that the different drying temperatures give the formation of different polymorphs of $Ca(BH_4)_2$. Drying at around

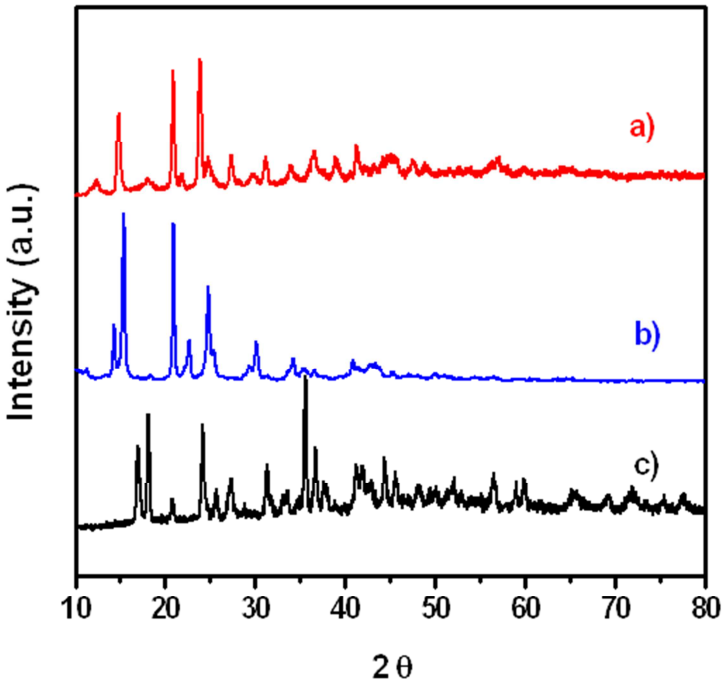

Fig. 2.4. XRD patterns of (a) $Ca(BH_4)_2 \cdot 2THF$, (b) $Ca(BH_4)_2 \cdot THF$, and (c) $Ca(BH_4)_2$

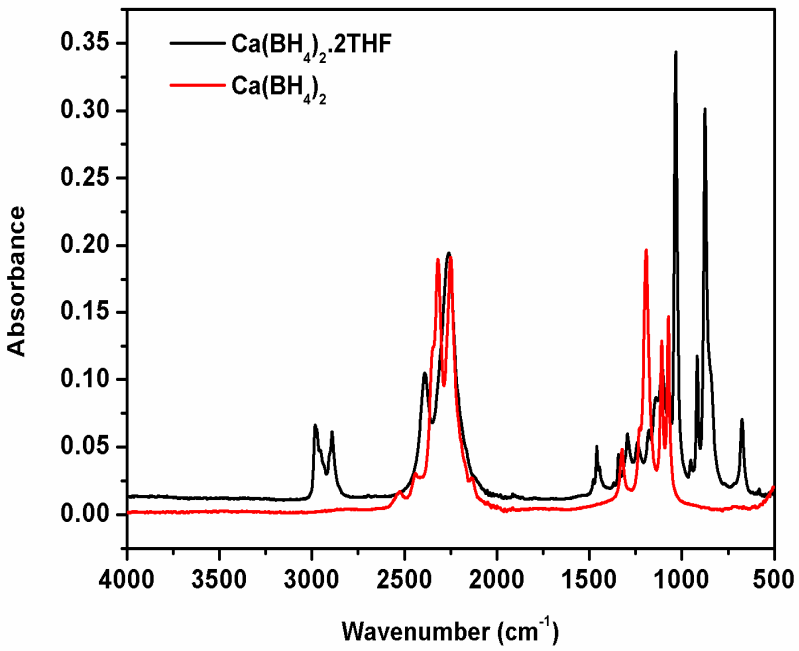

Fig. 2.5. FT-IR absorption spectra of $Ca(BH_4)_2 \cdot 2THF$ (black line) and dried $Ca(BH_4)_2$ (red line)

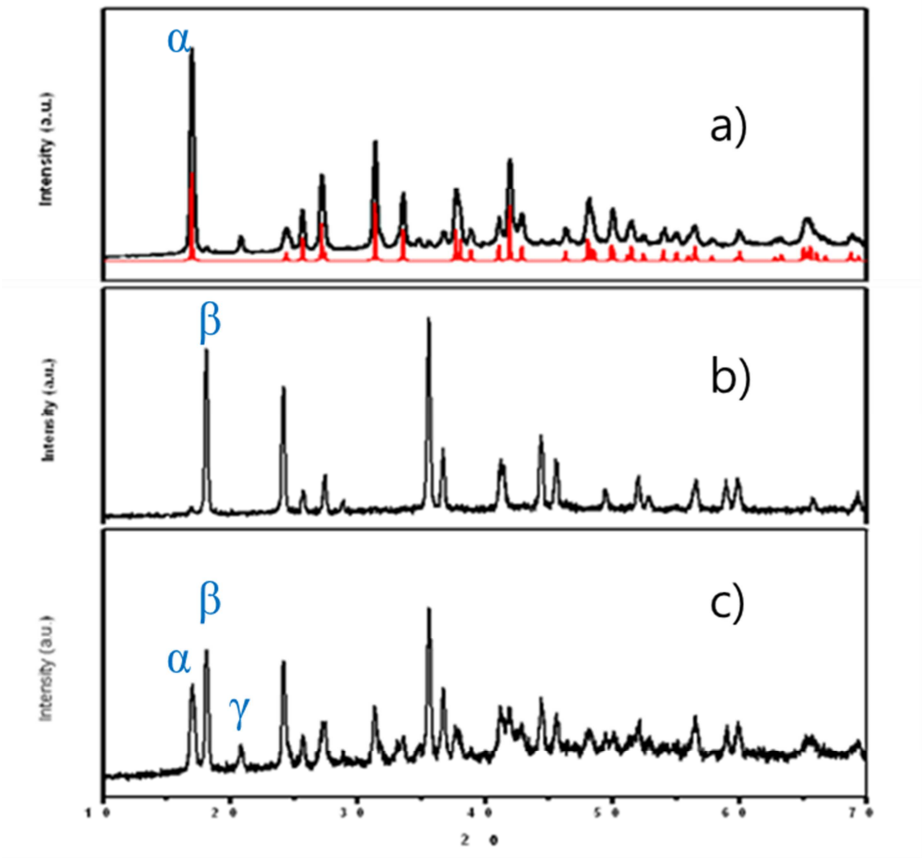

Fig. 2.6. XRD patterns of (a) α-$Ca(BH_4)_2$, (b)β-$Ca(BH_4)_2$, and (c) the mixture of α-, β-, and γ-$Ca(BH_4)_2$. α-$Ca(BH_4)_2$ (red line, the calculated pattern[67]) is inserted by comparison.

100 ˚C usually produces a mixture of α- and γ- $Ca(BH_4)_2$, while drying at higher temperature at around 200 ˚C gives mostly β-$Ca(BH_4)_2$.

Interestingly, ball-milling with other material, such as $LiBH_4$[60] gives a mixture of α-$Ca(BH_4)_2$,[67] and γ-$Ca(BH_4)_2$,[70, 74] but no bragg reflection can be assigned to β-$Ca(BH_4)_2$.[70] At room temperature, mixures of α-, β-, and γ-$Ca(BH_4)_2$ are usually found, as shown in Figure 2.6c, and the proportion of each phases is very sensitive to the preparation conditions.[58, 59, 66, 69, 71, 73] Several *in situ* XRD experiments have shown that α- and γ-$Ca(BH_4)_2$ transform to β-$Ca(BH_4)_2$ at elevated temperatures. Majzoub et al.[74] predicted that γ-$Ca(BH_4)_2$ is metastable, but this point has not been proven experimentally. Recently, I. Llamas-Jansa et al. reported the relation between the structure and decomposition behavior of the α, β, and γ polymorphs of $Ca(BH_4)_2$.[75] the results illustrate that the pure $Ca(BH_4)_2$ polymorphs have slightly differnet kinetic barriers and that the polymorphic content determines the decomposition kinetics of the samples. Thus, when $Ca(BH_4)_2$ decomposes, fast heating rate to the decomposition temperature before finishing completely the phase transition to β - $Ca(BH_4)_2$ may produce confusion understanding the dehydrogenation reaction pathway.

Therfore, the preparation of oxygen-free $Ca(BH_4)_2$ and a slow heating rate to β-$Ca(BH_4)_2$ play an important role for the investigation of the dehydrogenation reactions.

2.4. Dehydrogenation Reactions of $Ca(BH_4)_2$

2.4.1. Thermal Analysis of $Ca(BH_4)_2$

The DSC and TGA curves of $Ca(BH_4)_2$ are shown in Figure 2.7. Earlier studies have found the temperature of the polymorphic transformation from is α-$Ca(BH_4)_2$ to β-$Ca(BH_4)_2$ to be about 130-170 ˚C.[46, 58, 59, 76] However, this polymorphic transformation is not clearly seen in our DSC curve. The reason can be explained that the starting $Ca(BH_4)_2$ was a mixture of α, β, and γ-$Ca(BH_4)_2$ instead of a phase-pure α-$Ca(BH_4)_2$. As mentionte in section 2.3, different polymorphs have difffernt kinetics, which can be another reason for the absence of DSC signal. The phase transformation will be discussed more in section 2.4.2.1.

Both DSC and TGA data indicate that the dehydrogenation of $Ca(BH_4)_2$ starts at about 320 ˚C. About 8.7 wt % hydrogen is released during heating $Ca(BH_4)_2$. Based on the decomposition reaction 1, the theoretical weight loss is 9.6 wt %. The lower-than-ideal weight loss could be due to the purity of the starting material, exposure to air and moisture during the sample loading stage, or reaction 2 with lower hydrogen capacity occurring at the same time.

TGA and DSC results clearly show that the dehydrogenation reaction takes place in two steps. Two major endothermic peaks in the DSC curve and an inflection point between 320 and 550 ˚C in the TGA curve indicate that

$Ca(BH_4)_2$ desorbs hydrogen at least in two steps. Note that, there is another small endothermic peak at around 320 °C that also appears as a minimum in the differential TGA curve in Figure 2. 7c. The curve-shape at around 320 °C indirectly tells the possibility of the existence of another decomposition step.

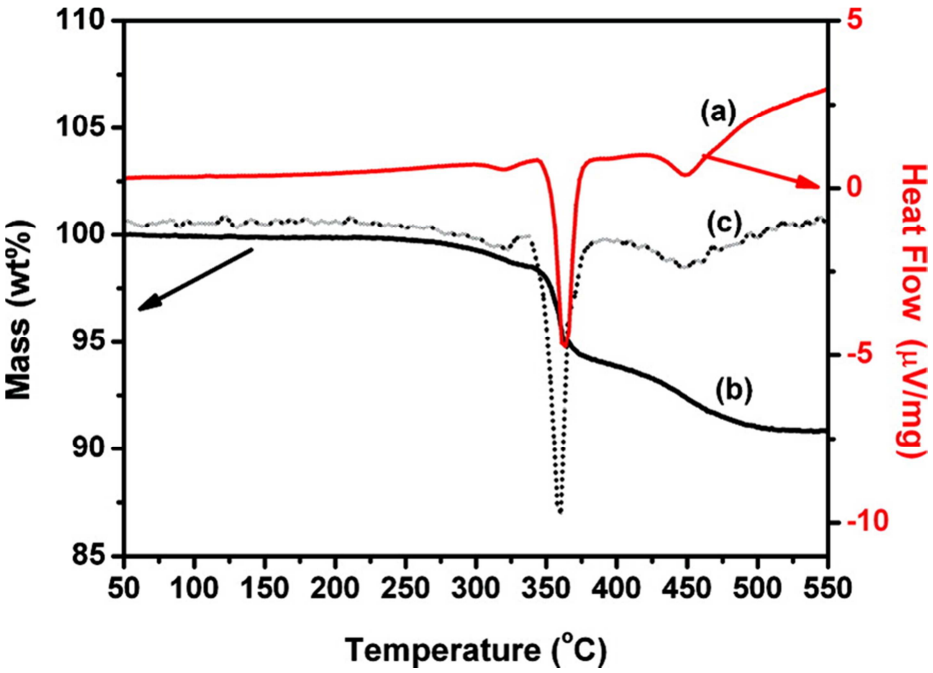

Fig. 2.7. (a) DSC, (b) TGA, and (c) differential TGA curves of a solvent-free $Ca(BH_4)_2$

2.4. 2. Dehydrogenation Reactions of $Ca(BH_4)_2$

2.4. 2.1. Phase Transformation of $Ca(BH_4)_2$

In previous reports, CaB_2H_x[38, 58, 59, 61] and $CaB_{12}H_{12}$[2, 35, 41, 42, 77-80] have been reported as intermediate phases by different research groups. CaB_2H_x was first observed by Kim et al.[59] during the dehydrogenation of $Ca(BH_4)_2$, and Riktor et al.[61] has proposed its crystal structure. The two-step dehydrogenation pathway involving the CaB_2H_x can be given as follows:

$$Ca(BH_4)_2 \rightarrow CaB_2H_x + (8\text{-}x)/2\ H_2 \rightarrow 2/3\ CaH_2 + 1/3\ CaB_6 + 10/3\ H_2 \quad (4)$$

On the other hand, others reported $CaB_{12}H_{12}$ as an intermediate, and the proposed reaction pathway is as follows:

$$Ca(BH_4)_2 \rightarrow 1/6\ CaB_{12}H_{12} + 5/6\ CaH_2 + 13/6\ H_2 \quad (5)$$

Interestingly, both CaB_2H_x and $CaB_{12}H_{12}$ have not been observed simultaneously or consecutively during the dehydrogenation of $Ca(BH_4)_2$. Some research groups only observed CaB_2H_x as a intermediate phase, while others shows the possibility of the formation of $CaB_{12}H_{12}$, and in this case, CaB_2H_x was not detected during dehydrogenation. So, it is believed that the formation is CaB_2H_x is sensitive.

To investigate the dehydrogenation reactions of $Ca(BH_4)_2$, *in situ* synchrotron X-ray diffraction of $Ca(BH_4)_2$ is measured at an isobaric condition of 1bar H_2 pressure. $Ca(BH_4)_2$ is heated to 300 °C in 30 min and

then heated up to 420 ˚C at a rate of 0.2 ˚C/min. Starting sample is mainly β-$Ca(BH_4)_2$ and contains a small amount of α-$Ca(BH_4)_2$.(see figure 2.8) Before dehydrogenation, the phases transformation from α to β-$Ca(BH_4)_2$ occurs in a wide temperature range between 198 and 277 ˚C, which supports the slow kinetics of phase transformation of α phase. Energy difference between the β-$Ca(BH_4)_2$ and α-$Ca(BH_4)_2$ phases at T = 0 K was calcultated by using density-functional theory (DFT), and the static total-energy difference was reported as the value of 10.9 kJ/mol.[81] This calculation result supports no DSC signal for the phase transformation in figure 2.7 and the reasons can be summarized as follows:

1) the exsitance of relatively small mole or weight fraction of α-$Ca(BH_4)_2$,
2) small energy difference between α and β phases,
3) slow kinetics for phase transformation

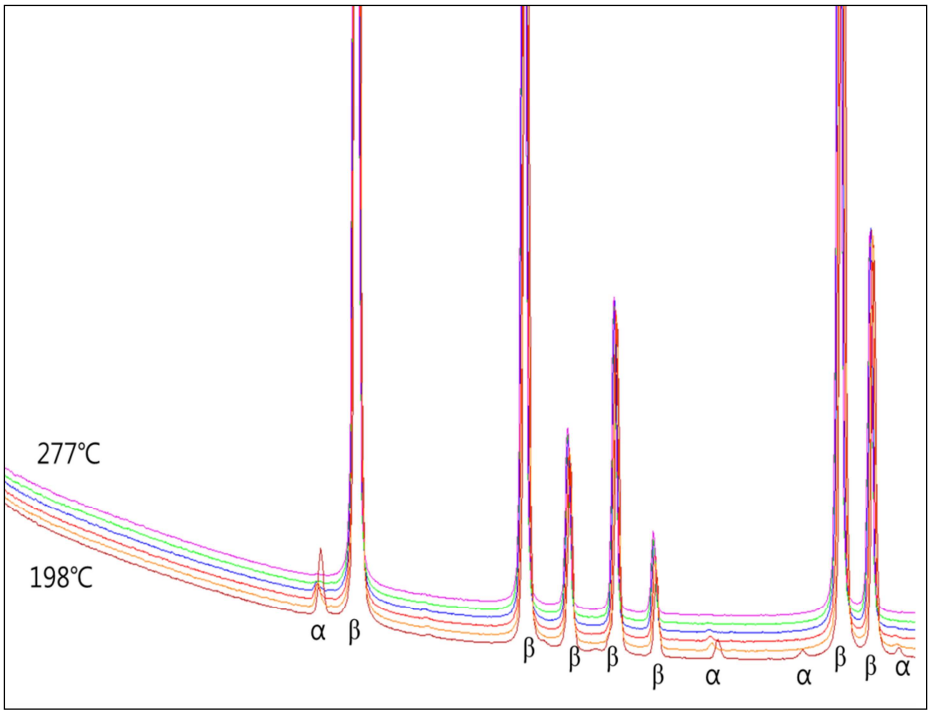

Fig. 2.8. *In situ* Syncrytron powder X-ray diffraction(SR-PXD) of $Ca(BH_4)_2$. α and β represent α-$Ca(BH_4)_2$ and β-$Ca(BH_4)_2$, respectively.

2.4.2.2. *In situ* Synchrotron X-ray Diffraction of $Ca(BH_4)_2$

Figure 2.9 presents *in situ* synchrotron X-ray diffraction data of $Ca(BH_4)_2$, and only shows the strongest peak of β-$Ca(BH_4)_2$ at the temperature range from 299 to 322 ˚C. β-$Ca(BH_4)_2$ starts to disappear approximately at around 300 ˚C. The strongest peaks of β-$Ca(BH_4)_2$ shift to the lower 2θ position at the temperature range of 300-332 ˚C. Rietveld refinement for each data was performed by using a TOPAS software.[63] In general, the calculated XRD pattern[70] from the present β-$Ca(BH_4)_2$ struture agree well with the measured ones. The weighted pattern R factors are almost 5.0 %. From the rietveld results, the unit cell parameters are plotted as a function of temperature in Figure 2.10. At the range of 299 to 332 ˚C, the unit cell parameters a and c (Å) and the unit cell volume ($Å^3$) of the β-$Ca(BH_4)_2$ increase linearly with temperature (˚C): $a = 6.831 + 3.078 \times 10^{-4} T$, $c = 4.2798 + 2.258 \times 10^{-4} T$, $V = 199.407 + 2.984 \times 10^{-2} T$. The peak shift of β-$Ca(BH_4)_2$ is a simple tendency of matter to change in volume in response to a change in temperature.

Figure 2.11 shows the *in situ* SR-PXD patterns of $Ca(BH_4)_2$ for the temperature range between 318 and 380 ˚C. At around 320 ˚C, the intensity of the β-$Ca(BH_4)_2$ starts to decrease rapidly.

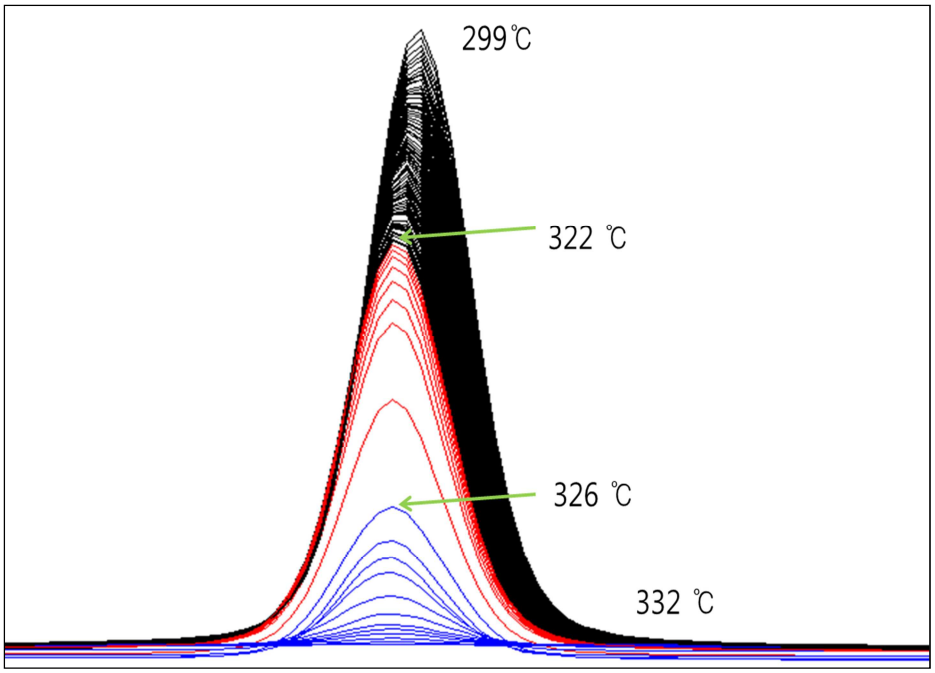

Fig. 2.9. The strongest peak of *in situ* SR-PXD of β-$Ca(BH_4)_2$ at the peak at $2\theta = 11°$

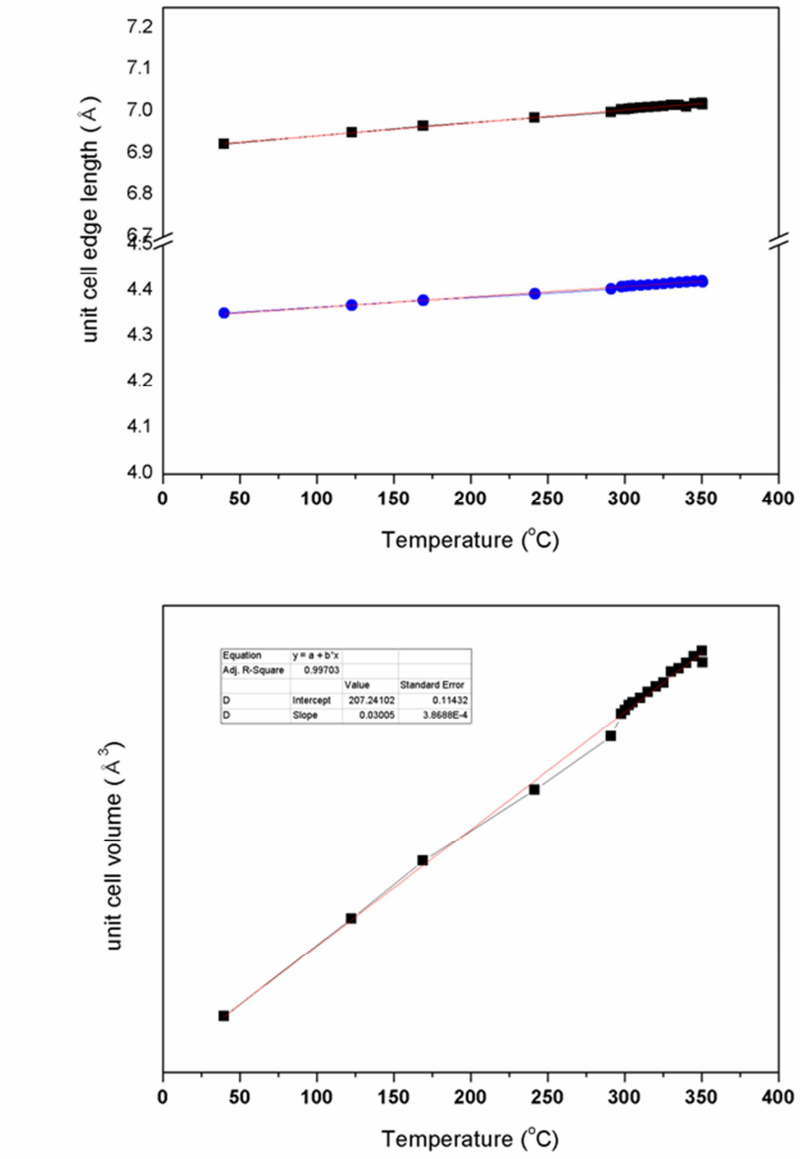

Fig. 2.10. Variation of the unit cell parameters and volume of the β-$Ca(BH_4)_2$ as a function of temperature.

No other new diffraction peaks were observed until β-$Ca(BH_4)_2$ disappeared completely, which indirectly indicates that the reaction product is in an amorphous state to the PXD scanning. After β-$Ca(BH_4)_2$ disappears completely at around 330 °C, CaB_2H_x peaks appeared, reaching to the maximum at 335 °C, and gradually get depleted as the temperature was raised to 380 °C. Formation of CaH_2 took place soon after, and this material increased in the range between 335 and 400 °C, coinciding with the decrease of CaB_2H_x. The peak intensity of CaB_2H_x is, however, relatively weak when compared to that of starting material β-$Ca(BH_4)_2$. The result simply shows that the reaction pathway 4 did occur, but the majority of the crystalline phase β-$Ca(BH_4)_2$ cannot be explained by the CaB_2H_x formation in the crystalline phase.

To investigate in more detail the desorption process of $Ca(BH_4)_2$, five samples were prepared. XRD patterns of $Ca(BH_4)_2$ and samples dehydrogenated at 340, 345, 350, and 500 °C are presented with labels (b), (c), (d), and (e), respectively. (Figure 2.12) Starting material, $Ca(BH_4)_2$ is identified as predominatly β phase according to XRD (Figure 2.12a). The pattern at 340 °C consists of the mixture of β-$Ca(BH_4)_2$ and CaB_2H_x. As temperature increases, the peaks of β-$Ca(BH_4)_2$ and CaB_2H_x disappeared, and those of CaH_2 emerged as shown in Figures 2. 12c~e. The *ex situ* XRD patterns confirm once again *in situ* XRD results. The XRD pattern of Figure 2.12e is composed of peaks from CaH_2, and there is no trace of intermediate

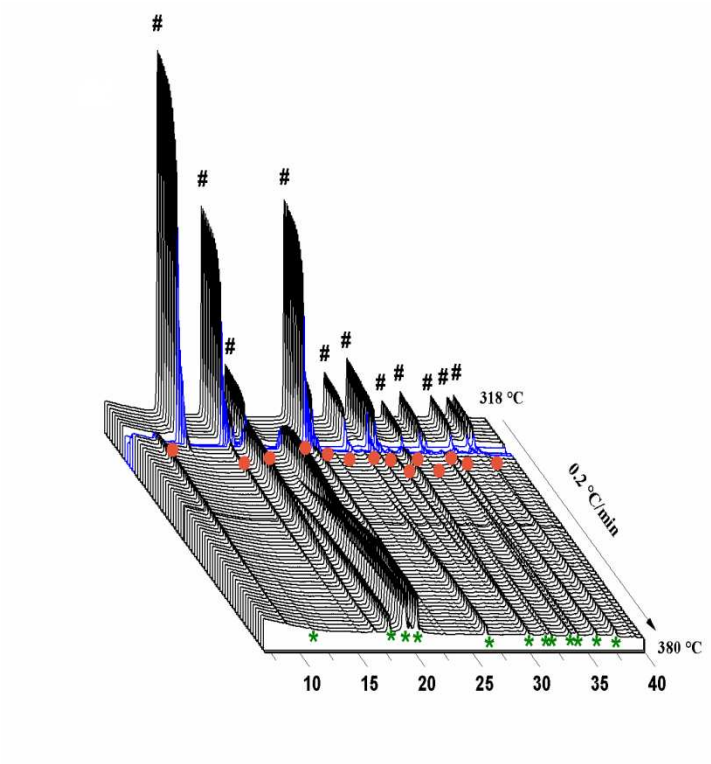

Fig. 2.11. *In situ* SR-PXD patterns (wavelength 1.00001 Å) of $Ca(BH_4)_2$ The sample was heated (0.2 °C/min) under 1 bar of H_2 pressure from 300 to 380 °C. Symbols #, ●, and * represent β-$Ca(BH_4)_2$, CaB_2H_x, and CaH_2, respectively.

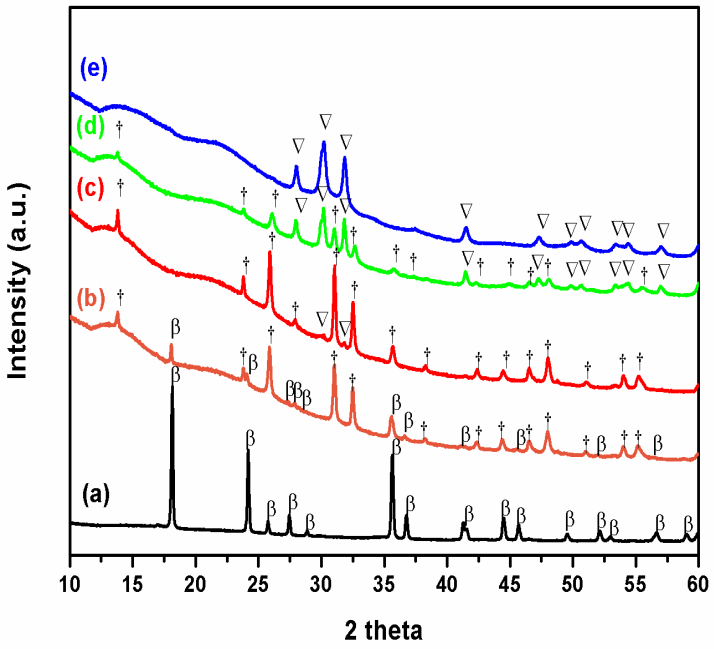

Fig. 2.12. XRD patterns of as-received $Ca(BH_4)_2$ and samples dehydrogenated at 340, 345, 350, and 500 °C, β, cross, and inverted triangle symbols represent β-$Ca(BH_4)_2$, CaB_2H_x, and CaH_2, respectively.

compound. Although it is not as clear as in Figure 2.12e, we can observe the broad hump around the main peak position of CaB_6. So, Rietveld refinement of a final dehydrogenated sample was performed, and lattice parameter and crystallite size are fitted to 4.12 Å (4.15 Å from CaB_6 reference) and 3 nm, respectively. Although CaB_6 is also known to be the final dehydrogenation product, the peaks are not clearly observed by XRD. The reason why boron is thought to be in amorphous form is that no boron-containing phase was detected in XRD. For this reason, the final form of boron and the exact decomposition path have not been fully understood up to now. To confirm CaB_6 clearly, Raman spectroscopy (Figure 2.13) outperforms XRD in detecting nanosized crystallites. The samples shown in figure 2.12c and 2.12e are used. Both spectra was compare with the one obtained from pure CaB_6. Three distinct peaks from CaB_6 are seen in their Raman spectrum. They are T_{2g}, E_g, and A_{1g} Raman active modes of CaB_6 in ascending frequency order.

Combining *in situ, ex situ* XRD and Raman data, we can describe the dehydrogenation reactions of $Ca(BH_4)_2$ at 1 bar H_2 isobaric condition as follows:

$$\begin{aligned} Ca(BH_4)_2 &\rightarrow \text{amorphous phase} \\ &\rightarrow CaB_2H_x + (8\text{-}x)/2H_x \\ &\rightarrow 2/3\ CaH_2 + 1/3\ CaB_6 + 10/3\ H_2 \end{aligned} \qquad (6)$$

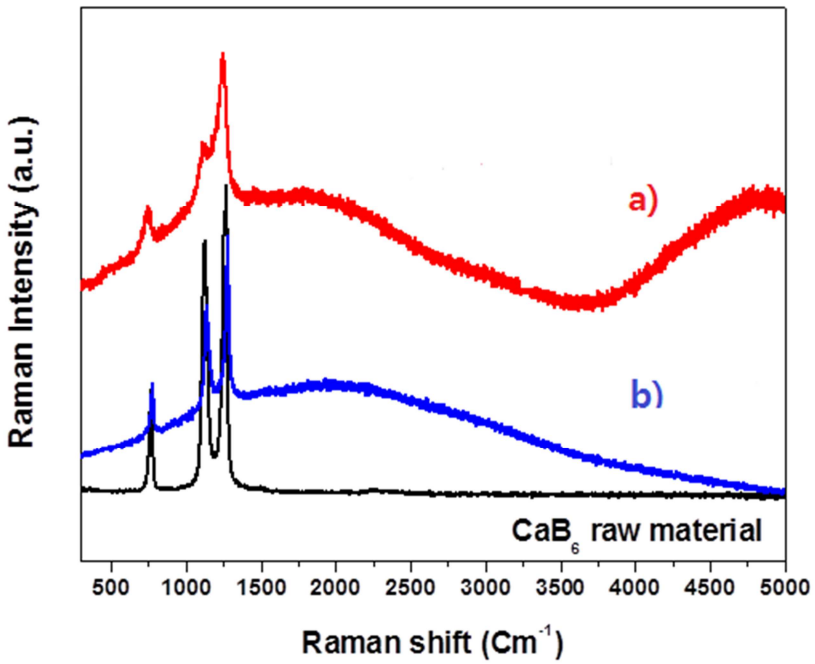

Fig. 2.13. Raman spectra of $Ca(BH_4)_2$ after dehydrogenation under 1 bar H_2 pressure (a) at 345 °C and (b) at 500°C. The Raman spectrum of CaB_6 reference is compared in (c).

2.4.2.3. The Formation of Amorphous Phases During Dehydrogenation of $Ca(BH_4)_2$

To further analyze possible formation of any noncrystalline intermediate phases which do not show up in the XRD patterns, we employed solid state ^{11}B magic angle spinning (MAS) NMR spectra of the dehydrogenated samples. (see Figure 2.14) The starting material (Figure 2.14a) is confirmed as β-$Ca(BH_4)_2$ from the −33.2 ppm peak which is clearly distinguished from the −29.6 ppm peak of the α-$Ca(BH_4)_2$ phase, and the result is consistent with the XRD determination (Figure 2. 12a). Note that NMR signatures have been characterized independently in our laboratory using commercially available product (Aldrich) or home-prepared materials showing the corresponding XRD patterns.[71] However, the values show some discrepancy from the values reported recently,[35] for which XRD patterns were not provided for comparison. For the sample after desorption at 340 °C, four peaks were resolved at 14.6, −18, −31.8, and −33.2 ppm (Figure 2.14b), as manifested by a spectral decomposition using Gaussian lines shown in Figure 2.14f. The relatively sharp peak at −33.2 ppm in the spectrum is readily assigned to the residual β-$Ca(BH_4)_2$ in the crystalline phase as it matches well with the reference spectrum of pure β-$Ca(BH_4)_2$ in Figure 2.14a. The broad peak at 14.6 ppm is likely to come from CaB_6, again in reference to the ^{11}B MAS NMR spectrum of neat CaB_6,[35] which indicates that

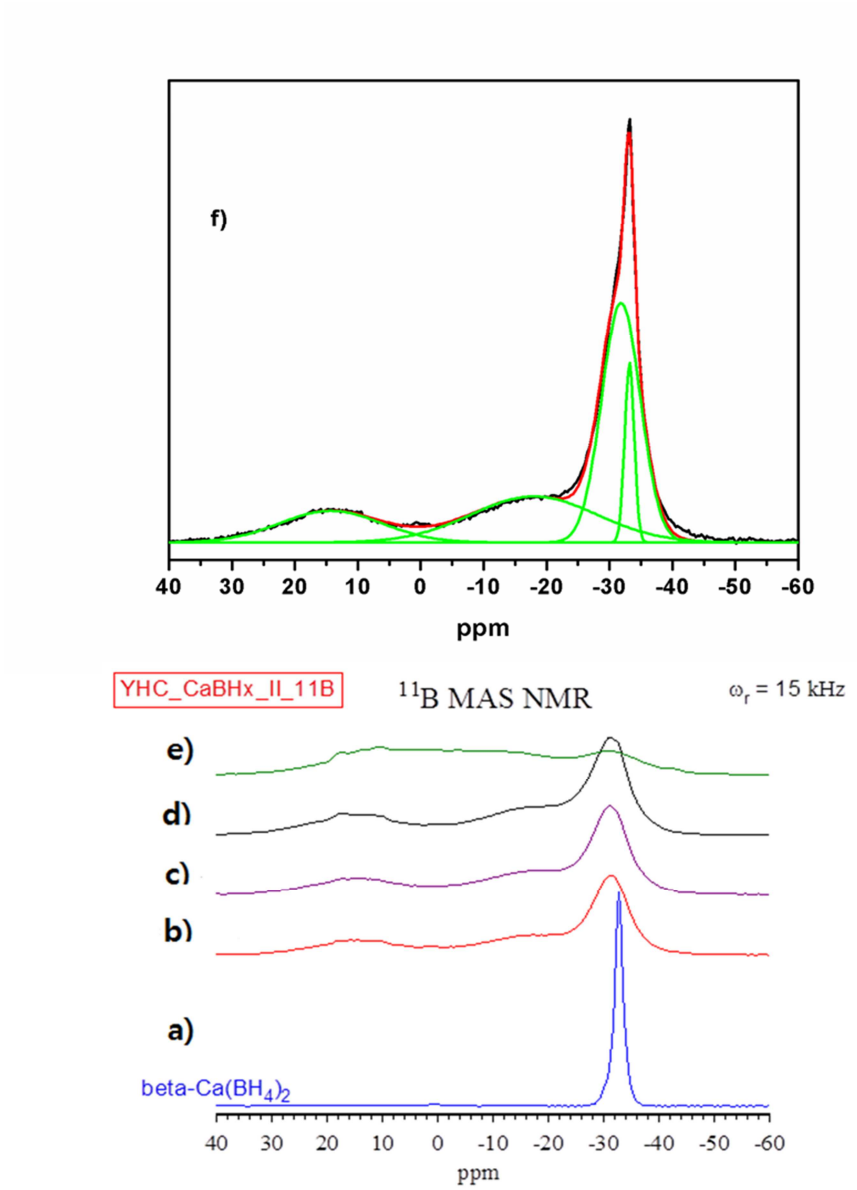

Fig. 2.14. ^{11}B MAS NMR spectra of (a) as-received $Ca(BH_4)_2$, samples at dehydrogenated at (b) 340 °C, (c) 345 °C, (d) 350 °C, (e) 500 °C, and (f) spectrum (b) decomposed into four peaks. The spinning rate is 15 kHz.

$Ca(BH_4)_2$ was partially dehydrogenated to the final dehydrogenation products. Another expected final decomposition product, CaH_2, could not be unambiguously confirmed by ^{1}H MAS NMR. ^{43}Ca NMR[82] could be an option for such a confirmation but was not attempted in the present study. The very broad peak that appeared at ~−18 ppm can be tentatively interpreted as $CaB_{12}H_{12}$ formation since the ^{11}B NMR shift of the center band is close to that of pure $CaB_{12}H_{12}$.[35, 42] In a recent report, Minella et al.[35] also used such a ^{11}B NMR peak to identify $CaB_{12}H_{12}$ formation in a dehydrogenation of the $Ca(BH_4)_2$−MgH_2 system. It is known that the $CaB_{12}H_{12}$ phase is not readily identified by XRD due to its amorphous feature[78] or by Raman because of the high fluorescence background of Ca. It is noteworthy that the formation of $CaB_{12}H_{12}$ in $Ca(BH_4)_2$ desorption studies has not been well addressed because of the lack of other spectroscopic evidence. The remaining issue here is to find the ^{11}B NMR shift of CaB_2H_x, which is one of the major phases identified in this sample as confirmed by the XRD patterns. No report on NMR characterization of the CaB_2H_x phase has been made to date. It is understandable since the formation of CaB_2H_x could be hydrogen back-pressure dependent, and if this is the case, one can observe this intermediate phase[38, 58-61] or not[41, 73] depending on the dehydrogenation conditions. Initially, there was a hope of probing the NMR signature of the CaB_2H_x phase as we start with samples showing the reproducible XRD patterns. The

remaining peak at −31.8 ppm in ^{11}B MAS NMR (Figure 2.14b), however, appears almost at the same position of α- or β-$Ca(BH_4)_2$ with additional broadening (1000 Hz, ~4 times broader compared to the neat $Ca(BH_4)_2$ phase). The same peak appeared for samples heated at 345, 350, and 500 °C (Figure 2.14c, d, and e) with progressive reduction in quantity. Interestingly, a sample heated at 500 °C of which the corresponding XRD is shown in Figure 2.12e did show the same ^{11}B peak despite its markedly reduced signal strength. Note that the CaB_2H_x phase does not survive after heating up to 500 °C (Figure 2.12e). Therefore, the most plausible interpretation could be that the signal at −31.8 ppm represents "an amorphous phase" having almost the same bonding environment with $Ca(BH_4)_2$. While the CaB_2H_x phase is detected as the major crystalline phase in XRD, its quantity might be significantly small compared to other boron-containing species in the amorphous phase. If this is the case, it is reasonable to conclude that the ^{11}B NMR signature of the CaB_2H_x phase could be overlapped with broad signals in the −10 ~ −35 ppm range, not discriminatively revealing its unique ^{11}B NMR feature.

"Amorphous phase" here should be thought of as unidentified noncrystalline phases from an XRD standpoint instead of a definite intermediate phase in the chemical reaction. This phase could be originated from residual $Ca(BH_4)_2$ in non-crystalline form due to its NMR position. Recently, there has been growing interest in $B_3H_8^-$ formation[83, 84] because

of the identification of $Mg(B_3H_8)_2$ in $Mg(BH_4)_2$ thermal decomposition.[83] They assigned the -30.3 ppm peak to $[B_3H_8]^-$ group, which is stable in water. However, in Figure 2. 15c-e, depending on the different time after mixing water, the peaks at ~-32 ppm disappear eventually, indicating that they slowly decompose in water. Therefore, we confirmed to not be attributed to possible $Ca(B_3H_8)_2$ formation from our ^{11}B solution NMR of water dissolution study (see Figure 2. 15) of the reaction products.

The spectrum at 345 °C (Figure 2.14c) makes a difference compared to that at 340 °C, in that the peak of β-$Ca(BH_4)_2$ at −33.2 ppm is no longer present and the hump of CaB_6 is more clear, indicating the further dehydrogenation. The peak at −31.8 ppm is still present as a major one revealing a high amount of amorphous phase to dehydride at this temperature. The spectrum at 350 °C makes no noticeable difference compared to that at 345 °C, except that the dehydrogenation reaction proceeds slightly further, producing more CaB_6 and $CaB_{12}H_{12}$. Along with the slight increase of CaB_6 and $CaB_{12}H_{12}$ signals, the decrease of the amorphous signal at −31.8 ppm is observed. As mentioned above, CaB_6 seems to be the dehydrogenation product of CaB_2H_x (Figure 2.12e). $CaB_{12}H_{12}$ can be formed as the dehydrogenation product of reaction 7.

$$Ca(BH_4)_2 \rightarrow \text{amorphous phase}$$

$$\rightarrow 1/6\ CaB_{12}H_{12} + 5/6\ CaH_2 + 13/6\ H_2 \qquad (7)$$

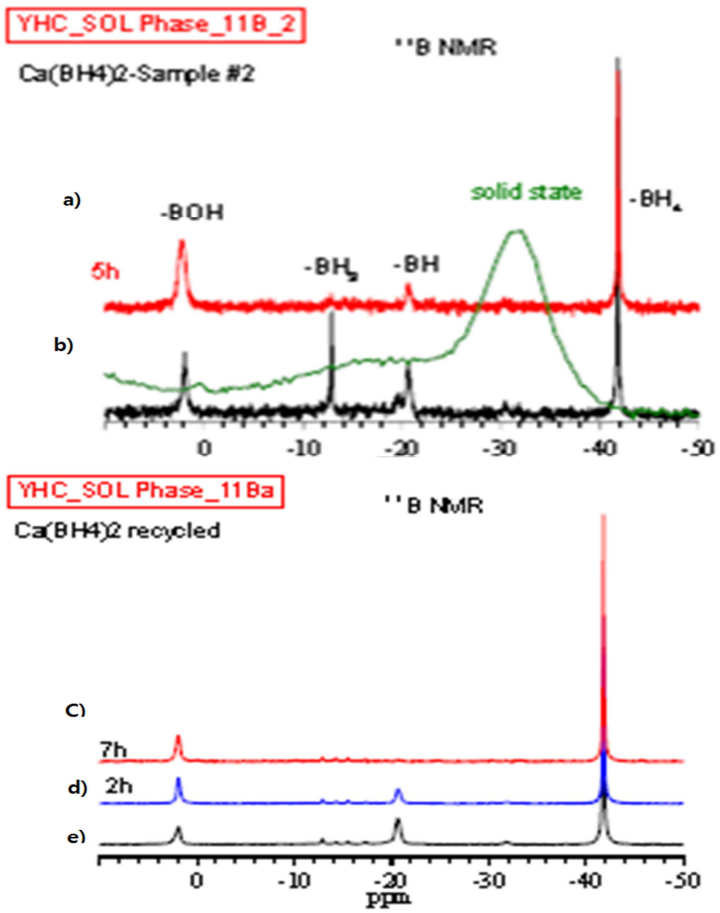

Fig. 2.15. Solution ^{11}B spectra of products resulting from dehydrogenated $Ca(BH_4)_2$ dissolved in aqueous solution showing various species formed during dehydrogenation and hydrolysis. (a) H-coupled ^{11}B NMR spectra and (b) H-decoupled ^{11}B NMR spectra of the dehydrogenated sample at 340 °C. The rehydrogenated sample (α-, β-$Ca(BH_4)_2$, amorphous phase, CaH_2, CaB_6, and $CaB_{12}H_{12}$) is dissolveed in water. ^{11}B NMR spectra is measured at differnet time after mixing water: (c) 7 hours, (d) 2 hours, and (e) 0 hour.

Combining both the XRD and NMR results, it can be concluded that $Ca(BH_4)_2$ readily transforms into the amorphous phase and then decomposes to CaB_2H_x or $CaB_{12}H_{12}$. The spectroscopic data clearly show competition between two different dehydrogenation pathways: reactions 6 and 7.

Observation of CaB_6 in significant quantity further implicates that only a portion of CaB_2H_x could be observed by XRD, and the rest remains invisible/indistinguishable to both XRD and NMR. We have assumed here that a chance of $CaB_{12}H_{12}$ undergoing dehydrogenation to CaB_6 is kinetically limited in our reaction conditions.

2.4.3. Hydroge Back Pressure Effects on the Dehydrogenation of $Ca(BH_4)_2$

2. 4. 3. 1. *in situ* SR-PXD of $Ca(BH_4)_2$

Summarizing above results, the formation of a considerable amount of $CaB_{12}H_{12}$ was also observed during dehydrogenation under 1 bar H_2 pressure. The formation of $CaB_{12}H_{12}$ is not desirable because of its high thermal stability and should therefore be avoided during dehydrogenation, especially when hydrogen storage application is concerned. In the case of the $LiBH_4$+YH_3 composite, it was demonstrated that the formation of intermediate $Li_2B_{12}H_{12}$ could be suppressed when dehydrogenation occurred under an H_2 pressure greater than 3 bar.[84, 85] A similar H_2 back pressure effect was also reported for the $LiBH_4$+MgH_2 composite.[86] The stability of intermediate compounds could be as important as the final products in determining the overall reversibility of the reaction. A systematic study on the effect of the dehydrogenation conditions on the reaction pathway is required.

Therefore, we measure the *in-situ* SR-PXD data of $Ca(BH_4)_2$ under two different pressures ($p(H_2)$=10 and 20 bar). At 1bar hydrogen isobaric conditions, the reactions to form CaB_2H_x and $CaB_{12}H_{12}$ (reaction 6 and 7), occured almost at the same time during dehydrogenation of $Ca(BH_4)_2$. When we increase hydrogen pressure to $p(H_2)$=10 bar (see Figure 2.16a), the dehydrogenation of $Ca(BH_4)_2$ shifts to a higher temperature than that of

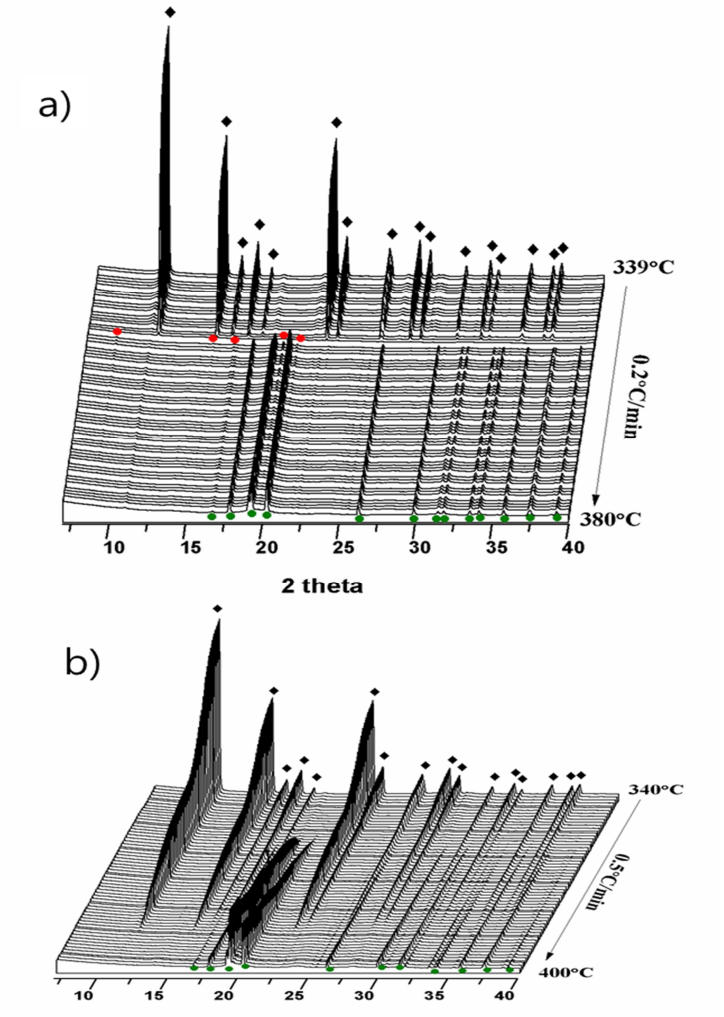

Fig. 2.16. *In situ* SR-PXD of $Ca(BH_4)_2$ in the temperature 310-400 °C under (a) 10 bar H_2, and (b) 20 bar H_2. Symbols; #, ●, and ● represent β-$Ca(BH_4)_2$, CaB_2H_x and CaH_2, respectively.

$Ca(BH_4)_2$ under $p(H_2)$=1 bar. The intensity of $Ca(BH_4)_2$ peaks decrease rapidly and disappear at approximately 350 °C. CaB_2H_x and CaH_2 peaks appear at the same temperature of 350 °C. The peak intensity of CaB_2H_x is relatively small, but the entire dehydrogenation reaction sequence under $p(H_2)$=10 bar are almost similar to those observed at $p(H_2)$=1 bar. At $p(H_2)$=20 bar, however, the CaB_2H_x phase is not detected during the decomposition reaction, while the formation of CaH_2 is still observable. (see Figure 2. 16b) When the hydrogen back pressure is increased, the formation of CaB_2H_x is suppressed, so it is possible to conclude that some $Ca(BH_4)_2$ directly decomposes into CaH_2 and CaB_6, as shown in reaction (1).

2. 4. 3. 2. The Formation of CaB_2H_x and CaH_2

The normalized intensities of *in situ* SR-PXD data are shown in Figure 2. 17. For this plot, we utilized the intensities of the strongest peak, such as the peak at 2θ=10° for β-$Ca(BH_4)_2$, and each identified crystalline phase in the *in situ* SR-PXD data (Figure 2.11 and 2.16) are normalized to the intensity of the highest peak of β-$Ca(BH_4)_2$ at 317 °C. The peak intensity of all other newly formed dehydrogenated species are significantly weaker than that of the starting $Ca(BH_4)_2$, suggesting that the majority of the dehydrogenated intermediate products is amorphous and not being detected in the *in situ* measurements. Nonetheless, Figure 2.17 allows us to extract one important piece of information: the CaB_2H_x formation is noticeable, particularly for low H_2 back pressures (see $p(H_2)$=1 bar), and it markedly diminishes at high H_2 back pressures (barely observed under $p(H_2)$=10 bar and not observed under $p(H_2)$=20 bar). The SR-PXD result indicates that the CaB_2H_x phase, under a high H_2 pressure, is thermodynamically unfavorable or its formation takes places in an invisible manner, such as in an amorphous phase. CaH_2 is commonly observed as a dehydrogenation reaction product, and the profile of the CaH_2 formation in our observation plays a valuable role in determining the reaction routes. Under $p(H_2)$=1 bar, the CaH_2 phase is formed slowly in the range of 335-380 °C, which corresponds well to the slow decrease of the CaB_2H_x phase. From this result, the following

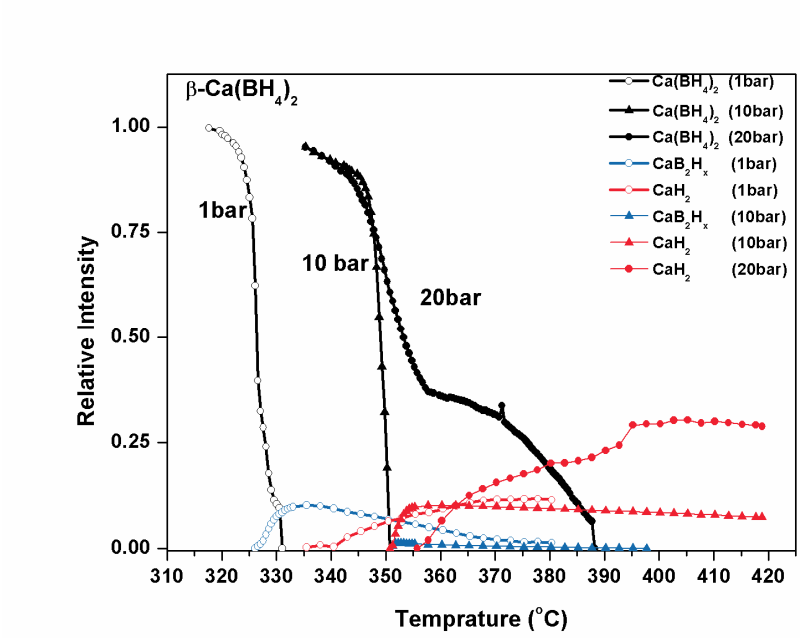

Fig. 2. 17 Normalized intensities of the *in situ* SR-PXD data measured for $Ca(BH_4)_2$ under three different pressures. The open circles, triangles, and solid cicles represent measurements under $p(H_2)$ = 1, 10, and 20 bar, respectively. Additionally, the black, blue, and red lines represent the quantity of the β-$Ca(BH_4)_2$,CaB_2H_x, and CaH_2 phases, respectively.

dehydrogenation route to the CaH_2 formation can be suggested at $p(H_2)$=1 bar:

$$CaB_2H_x \rightarrow 2/3\ CaH_2 + 1/3\ CaB_6 + (x/2-2/3)H_2 \quad (8)$$

Under $p(H_2)$=10 bar, both CaH_2 and CaB_2H_x are produced simultaneously only after the crystalline $Ca(BH_4)_2$ phase disappears completely at approximately 350 °C. After a sudden increase in the CaH_2 peak in the temperature range of 351-355 °C, the intensity remains constant. While the intensity of CaB_2H_x is significantly lower than that at 1 bar, the intensities of the CaH_2 phase obtained under $p(H_2)$=1 and 10 bar are similar. It is not likely that CaH_2 is directly formed by the decomposition of β-$Ca(BH_4)_2$, as evidenced in the in situ SR-XRD observation, but rather that CaH_2 begins to appear after the $Ca(BH_4)_2$ disappears completely. This result allows us to speculate that species in the amorphous phase should participate in the formation of CaH_2. Here, we formulate the dehydrogenation reaction under $p(H_2)$=10 bar as follows:

$$\text{Amorphous phase} \rightarrow xCaH_2 + yCaB_6 + zH_2 \quad (9)$$

Under $p(H_2)$=20 bar, Figure 2. 17 shows that the intensity of CaH_2 increases at the same rate at which the intensity of $Ca(BH_4)_2$ decreases, which supports reaction (1).

In addition to the pressure effects, there could be a temperature effect because significant difference in the CaH_2 formation temperature is present depending on the increase in pressure. These results indicate that the main

reaction route to the formation of CaH_2 can be changed by varying the H_2 back pressure.

2.4.3.3. The Formation of Amorphs Phases

All *in situ* XRD data show a sudden decrease in β-$Ca(BH_4)_2$ without the accompanying increase in any other Bragg peaks, suggesting that the solid-state chemical reaction occurs mainly in the non-crystalline, i.e., amorphous. In addition to the β-$Ca(BH_4)_2$ in the amorphous phase, other species in amorphous phases, such as $CaB_{12}H_{12}$ or elemental boron, are well known as the dehydrogenation products of metal borohydrides. Thus, we prepared four samples dehydrogenated under different hydrogen pressures to confim the formation of amorphous boron, B, and $CaB_{12}H_{12}$ under various back pressure. The sample dehydrogenated under $p(H_2)$=5 bar was also included for the *ex situ* analysis; so samples obtained under $p(H_2)$=1, 5, 10 and 20 bar were analyzed. Each sample was heated up to 420 °C with a slow heating rate of 0.2 °C/min. As the hydrogen pressure increases, the dehydrogenation temperature of $Ca(BH_4)_2$ increases. However, when we look over *in situ* XRD, there are no significant differences in the final decomposition temperature (above which the XRD patterns do not change) up to 20 bar. Thus, we prepared fully dehydrogenated samples at the same temperature (420 °C), so the result will represent only the pressure effects on the dehydrogenation of $Ca(BH_4)_2$.

All XRD patterns show the broad humps in the background around 22°. The humps in each pattern come from the X-ray scattering by the glass

capillary tube. The amorphous "$Ca(BH_4)_2$ related" or elemental boron could also be observed, if any, in the same range as a broad halo, such as the case in $Mg(BH_4)_2$.[87] XRD patterns of the dehydrogenated phases at 420°C show the peaks from CaH_2 and broad humps from CaB_6, which are expected in the $Ca(BH_4)_2$ dehydrogenation reaction (see Figure 2. 18). In contrast, ^{11}B NMR data further show the presence of several noncrystalline phases, as shown in Figure 2.19. For the sample that was dehydrogenated under $p(H_2)$=1 bar, three broad peaks at 14, -16, and -30 ppm are assigned to CaB_6, $CaB_{12}H_{12}$ and the unidentified amorphous phase(s), respectively. The -30 ppm peak appeared closer to the α-$Ca(BH_4)_2$ compared to the -31.8 ppm peak of the amorphous phase observed at a lower decomposition temperature. Because the NMR measurements here are performed *ex situ* and at ambient temperature, the detection of the α-$Ca(BH_4)_2$ phase after cooling is understandable. However, it is still not settled whether the peak represents unreacted α-$Ca(BH_4)_2$ in a highly disordered environment due to the broadening and lack of spinning sidebands, which make it difficult to access the structural information. As shown above, the XRD data do not support the existence of a $Ca(BH_4)_2$ phase. Therefore, we leave the peak unassigned as the "unidentified amorphous phase(s)" observed at the initial dehydrogenation step of $Ca(BH_4)_2$. ^{11}B CPMAS experiments were performed for these samples and plotted together in broken line as shown in Figure 2.19. The -30 ppm peak always appears in

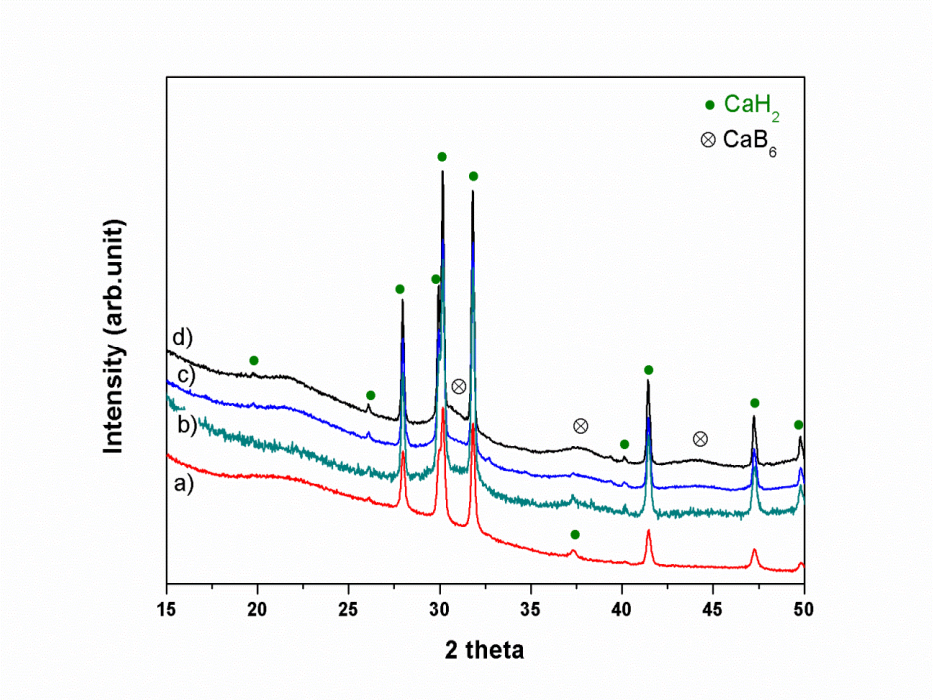

Fig. 2.18. *Ex situ* XRD data of four dehydrogenated samples at 420 °C under (a) $p(H_2)$= 1 bar, (b) $p(H_2)$=5 bar, (c) $p(H_2)$=10 bar, and (d) $p(H_2)$ = 20 bar.

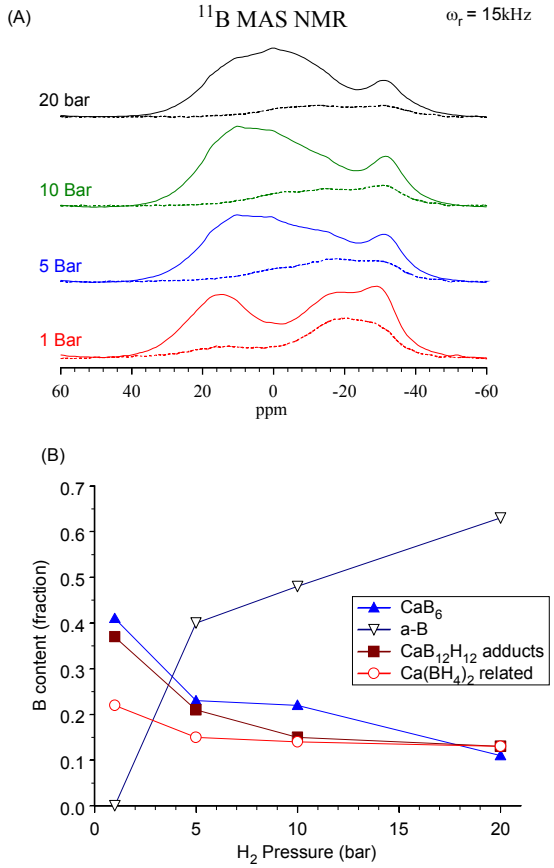

Fig. 2.19. (A) NMR data of three dehydrogenated samples at 420 °C under (a) $p(H_2)$=1 bar, (b) $p(H_2)$=5 bar, (c) $p(H_2)$=10 bar, and (d) $p(H_2)$=20 bar. Broken lines represent ^{11}B CPMAS NMR spectra obtained using 0.075 ms of cross polarization contact time. (B) Relative composition of boron species obtained from the spectral decomposition of ^{11}B spectra in (A) as a function of hydrogen back pressure in the thermal decomposition of $Ca(BH_4)_2$.

the CP spectra (with cross polarization contact time of 0.075 ms), and so from this further characterization it is concluded that the -30 ppm peak is boron species with B-H bonds. Three peaks corresponding to CaB_6, $CaB_{12}H_{12}$, and the unidentified amorphous phase are also observed in the samples dehydrogenated under $p(H_2)$=5, 10 and 20 bar. However, elemental boron is now observed based on the broad peak at ~4.5 ppm and 16 ppm (see Figure 2.18), implying that one of the dehydrogenation products under high H_2 pressures is an amorphous form of elemental boron.[86] By applying a high hydrogen pressure, not only the suppression of $CaB_{12}H_{12}$ but also a decrease in CaB_6 and an increase in elemental boron are observed. Note that in the ^{11}B MAS NMR spectra of these samples, the elemental boron peak appears featurelessly overlapped with the CaB_6 signal at 14 ppm and with $CaB_{12}H_{12}$ at ~-16 ppm. For example, according to ^{11}B CPMAS spectra shown in Figure 2.19, the major part of signal at around -16 ppm (for samples under high H_2 pressure) is boron species without B-H bonds. The result is further supporting the presence of amorphous elemental boron. In our best effort, the presence of a broad resonance at 4.5 ppm and -16 ppm for three samples was analyzed by spectral decomposition (see Figure 2. 19, the method was used in the previous report on the $LiBH_4$ decomposition reaction under various H_2 back pressures[86]). For this process, ^{11}B MAS NMR spectrum of a-B (Sigma-Aldrich) and its decomposition (see Figure 2.21) were closely utilized. The same line widths and the intensity ratio between the two peaks were employed

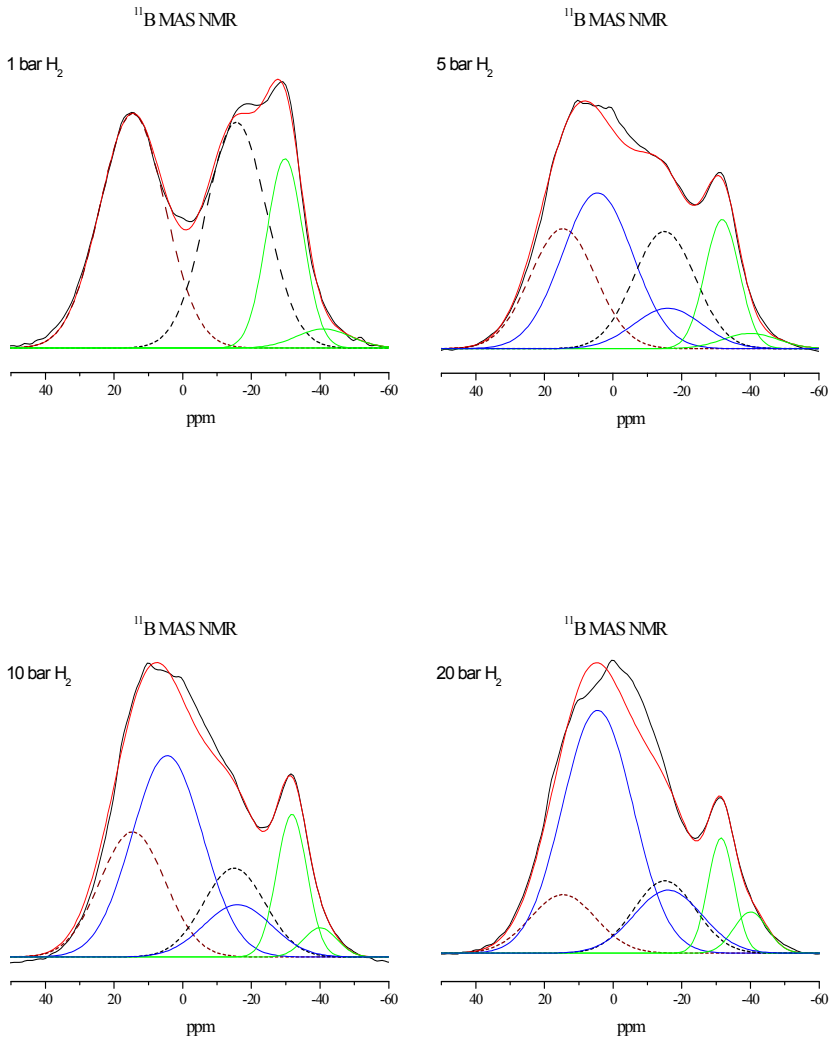

Fig. 2.20. ^{11}B MAS NMR spectra with the decomposition into CaB_6 (broken line at 14 ppm), elemental boron (blue solid line at 4.5 ppm and -16 ppm), $CaB_{12}H_{12}$ (broken line at -15.6 ppm), and $Ca(BH_4)_2$ related unidentified amorphous phase (green solid lines at -32 ppm and -40 ppm)

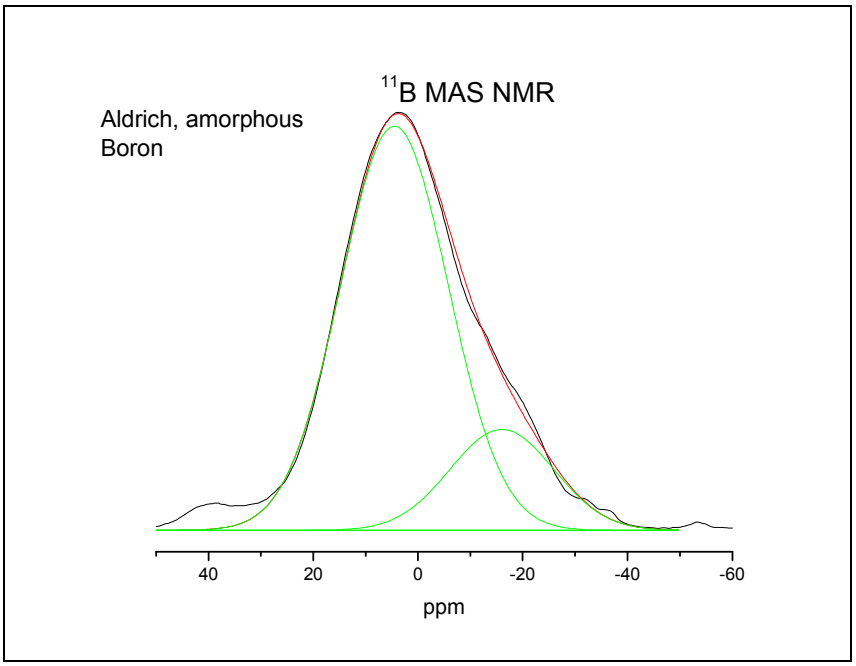

Fig. 2.21. ^{11}B MAS NMR spectrum of amorphous boron (Aldrich) and its spectral decomposition into two major peaks at 4.5 ppm and -16 ppm. The distribution of two peaks is in a 4:1 ratio according to the signal integration.

in all the decomposition attempts in order to draw a reasonable spectral fits. Intensity of the 4 ppm peak was first estimated and the -16 ppm peak was artificially added with the corresponding intensity ratio. The rest of signal was filled with addition of the $CaB_{12}H_{12}$ peak. Therefore, the quantitation of $CaB_{12}H_{12}$ is believed to be particularly inaccurate. In addition, note that the spectral decomposition was performed on the center bands of the central transition of ^{11}B (I=3/2) MAS spectra that were acquired with a small nutation angle. Due to the highly disordered environment of the boron species in this case, no MAS NMR powder line shape is well defined.[78] Consequently, the center band peaks are expected to contribute to the spinning sidebands originating from the satellite transition of ^{11}B nuclei, which is nearly impossible to resolve and can be an additional inaccuracy in the boron quantitation. Because all boron peaks behave in the same manner and there is no well-established method for handling the complexity, we ignored the satellite transitions in the calculation. Nonetheless, the amount of elemental boron species was quantified along with other boron species, and the result is shown in Figure 2.19B as a function of the hydrogen back pressure. In the plot, it is easy to see how quickly the formation of elemental boron increases with increasing H_2 back pressure. Smaller amounts of CaB_6 and $CaB_{12}H_{12}$ species were formed, while they showed a different behavior at high pressures. Note here that the peaks at -32 ppm and -41 ppm (see Figure 2.19) were labeled as "$Ca(BH_4)_2$ related," which correspond to the "unidentified amorphous

phase(s)" mentioned above. Such intermediate species showed a minor decrease under p(H_2)=5 bar and remained unchanged at the higher pressures. While the elemental boron formation and its amount of change under different H_2 back pressures are now better understood as a result of the ^{11}B NMR study, it is not yet clear which reaction pathway is operating. However, from the results, the reaction 2 can be formulated as a separate path under p(H2)= 5, 10 and 20 bar.

DFT calculations[38] predicted that the enthalpies of reactions (1) and (2) were 40.6 and 57.3 kJ/mol H_2, respectively. Based on these results, we plotted the van't Hoff curves in Figure 2.22, which indicate that reaction (1) is more favorable than reaction (2) under our experimental pressures. However, even with the favorable thermodynamics of reaction (1), $Ca(BH_4)_2$ residue was found; in other words, the reaction was not completed. The ^{11}B NMR data (Figure 2.19) support the existence of a "$Ca(BH_4)_2$-related" amorphous phase, and this phase remains, even at the higher temperature of 500°C. (see Figure 2. 14e) This evidence of $Ca(BH_4)_2$ residue might indicate slow kinetics for reaction (1). It is still ambiguous why crystalline $Ca(BH_4)_2$ transforms into an amorphous form during heating and why it decomposes very slowly. However, we can speculate that the slow kinetics provide room for the thermodynamically less favorable reaction (2) to occur.

Elemental boron can also be formed from the dehydrogenation of amorphous $CaB_{12}H_{12}$:

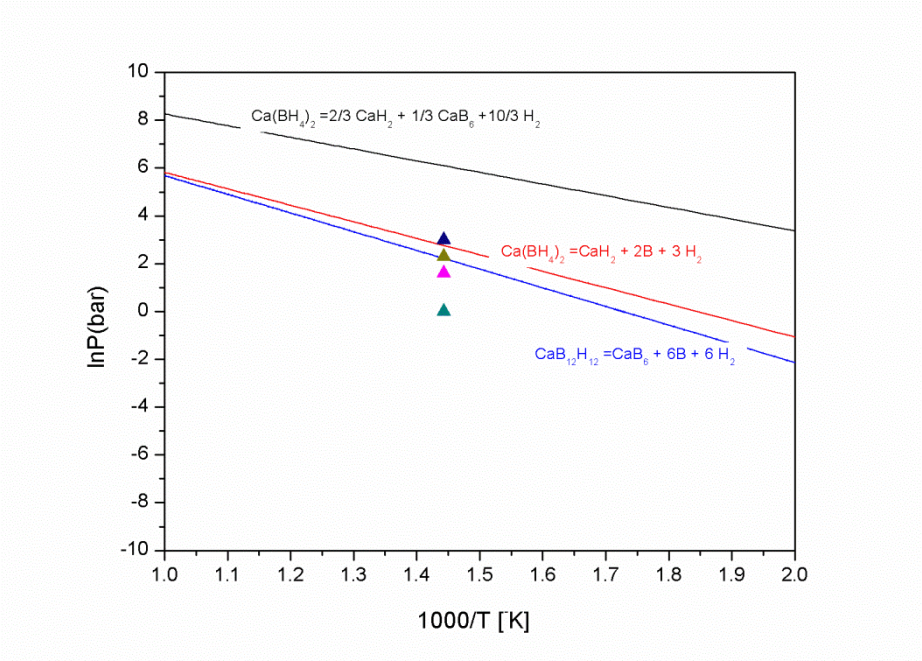

Figure 2. 22. Van't Hoff curves of reactions (1), (2), and (10). Each thermodynamic value is obtained from previously reported paper.[38, 81] The experimental conditions required to obtain the dehydrogenated samples are marked with triangles. The dehydrogenation temperatures of all samples are the same, 420°C. Green, pink, yellow, and blue triangles represent the dehydrogenation under $p(H_2)$=1, 5, 10, and 20 bar, respectively.

$CaB_{12}H_{12} \rightarrow CaB_6 + 6B + 6H_2$ (10)

The enthalpy and entropy change of reaction (10) is 73.7 kJ/mol H_2 and 127.4 J/K mol H_2[81] respectively, which predicted reaction (10) can occur at 420 °C under $p(H_2)$= 5 bar. Reaction (10) becomes thermodynamically unfavorable as $p(H_2)$ increases above 10 bar. Furthermore, it is experimentally observed that the presence of CaH_2 promotes the dehydrogenation of $CaB_{12}H_{12}$ through reaction (11) instead of reaction (10).[42]

$CaB_{12}H_{12} + CaH_2 \rightarrow 2CaB_6 + 7H_2$ (11)

Therefore, we can predict that reactions (10) and (11) are not the main routes to form elemental boron. The reasons for the formation of elemental boron are not clear at this point, but based on the above results, there appears to be a subtle competition among different dehydrogenation reaction paths, depending on the hydrogen back pressure and temperature. A high hydrogen back pressure promotes the formation of a stable compound, such as elemental boron, which is not a desirable dehydrogenation route with respect to the reversibility. As discussed above, the kinetics of the "$Ca(BH_4)_2$-related" amorphous phase appear to play a very important role in the reversible formation of $Ca(BH_4)_2$. Among the intermediate phases, CaB_2H_x is fully reversible under relatively moderate conditions without any catalytic additive. (see chapter 4) With catalytic additive, CaH_2 can be rehydrogenated

by the reaction with CaB_6 [76] or MgB_2[46] under moderate conditions. However, the formation of $CaB_{12}H_{12}$ and elemental boron as final products could lead to a degradation in the reversibility of the dehydrogenation reaction because of their high stabilities. To avoid the formation of unwanted $CaB_{12}H_{12}$ or elemental boron, control of the dehydrogenation reaction pathway is crucial for reversible hydrogen storage. The exact dehydrogenation reaction route and method of controlling the reaction path of $Ca(BH_4)_2$ must be further explored to make $Ca(BH_4)_2$ more reversible under mild conditions for practical applications.

Chapter 3

Dehydrogenation Reactions of $Ca(BH_4)_2$ + MgH_2 Composite

3.1. Introduction

Group I and II metal borohydrides are attractive as solid hydrogen storage materials because they offer large gravimetric and volumetric storage densities.[88-92] However, since no single metal hydride could be found that satisfies both the energy density and efficiency criteria, research has now been concentrated on more complex systems with several interacting components (the so-called reactive hydride composites (RHCs)). Despite the lower total capacity of these systems compared to the component of the system with highest capacity, by careful selection of the components, it is possible to obtain a relatively high total hydrogen capacity with this approach. The progress in this respect has been the discovery of a unique kinetic property of MgB_2,[43-45, 51] through which high capacity light metal complex borohydrides can be hydrogenated with low reaction enthalpy. This kinetic property for the first time provides systems that can operate in the optimal thermodynamic range for hydrogen storage (high-energy efficiency) and, at

the same time, contain high gravimetric hydrogen capacity (high-energy density).

Recently, a more promising result was reported by Barkhordarian et al.[46] who successfully obtained $Ca(BH_4)_2$+MgH_2 starting from CaH_2+MgB_2; the hydrogenation reaction proceeded completely without catalysts, which can be attributed to the recently discovered kinetic effect of MgB_2.[43-45, 51] However, upon dehydrogenation, Mg instead of MgB_2 was produced implying that the unique kinetic effect of MgB_2 might not be easily maintained during cycling. The final form of boron is yet unknown. Here we identify the dehydrogenated product of $Ca(BH_4)_2$ + MgH_2 composite and discuss possible decomposition routes based on our experimental results and theoretical calculations.

3.2. Experimental Procedure

Approximately 2 g of $Ca(BH_4)_2$ + MgH_2 mixture in a molar ratio of 1:1 was charged with 7 × 12.7 mm and 14 × 7.9 mm diameter Cr-steel balls into a hardened steel bowl and sealed with a lid having a Viton O-ring. The mixture was milled using a planetary mill (Fritsch P7) at 600 rpm for 4 h. Again two samples were prepared. Dehydrogenation reactions were done at 350 and 400 °C.

The powder X-ray diffraction (XRD, Bruker D8 with Cu KR radiation, λ =1.5418 Å) data were collected for phase composition analysis. All *ex situ* XRD measurements were performed at room temperature. A dome-shaped, vacuum tight, sample holder was used to prevent contact with air during XRD measurement. XRD data were analyzed by Rietveld refinement using the TOPAS software.[63]

The thermal decomposition behaviors of the samples were characterized using a differential scanning calorimeter (Netzsch DSC 204 F1) and a thermogravimetric analyzer (Netzsch TG 209 F1). For both differential scanning calorimetry (DSC) and thermogravimetric analysis (TGA), ca. 3 mg of sample was heated to 500 °C at a scanning rate of 2 °C/min under flowing argon condition (assay 99.9999%, 50 mL/min). Al crucible was used for measuring both TGA and DSC.

Raman spectroscopy was performed on samples at room temperature

using a Renishaw InVia reflex spectrometer, with a 633 nm excitation laser, and an Instec HCS621V sample hotstage that allowed inert loading. The Raman spectrum of CaB_6 (Sigma-Aldrich) was obtained and used as a reference. Raman measurements was done by the collaborated work with Birminham University.

In situ synchrotron radiation powder X-ray diffraction (SR-PXD) measurements were carried out at the 10B XRD KIST-PAL beamline in the Pohang Accelerator Laboratory (Pohang, Korea). The selected X-ray wavelength was 0.998398 Å, and sapphire capillary tubes with a 1.07 mm inner diameter were used. $Ca(BH_4)_2$ samples were heated from room temperature to 300 °C in 30 minutes and then heated to 420 °C at a rate of 0.2 °C/min. The hydrogen pressure of each sample was maintained at 1 bar during measurement, respectively. XRD patterns were collected every 147 s during the in situ measurements using a MAR 345 image plate detector. The two-dimensional (2D) images were converted into normal diffraction patterns by the FIT2D program.

3.3. Identification of the Dehydrogenated Phases of $Ca(BH_4)_2 + MgH_2$ Mixture

3.3.1 Thermal Decomsition Behavior of $Ca(BH_4)_2 + MgH_2$ Composite

Figure 3.1 shows XRD pattern of the as-milled $Ca(BH_4)_2 + MgH_2$ composite. All observed reflections are identified as the polymorph of $Ca(BH_4)_2$ or MgH_2. Hence we conclude that $Ca(BH_4)_2$ or MgH_2 exist as a physical mixture rather than a new compound or a solid solution. Interestingly, ball-milling with MgH_2 gives a mixture of α-$Ca(BH_4)_2$ and γ-$Ca(BH_4)_2$, but no Bragg reflection can be assigned to β-$Ca(BH_4)_2$ which is usually the majority phase of $Ca(BH_4)_2$ powder dried at 200 °C.

The thermal decomposition process of $Ca(BH_4)_2 + MgH_2$ composite was analyzed by DSC and TGA; the results are shown in Figure 3.2. The DSC curve shows two endothermic peaks from polymorphic transformation of α- and γ-$Ca(BH_4)_2$ at around 170 °C. The third peak between 320 and 400 °C accompanies weight loss as shown in the TGA curve. The $Ca(BH_4)_2 + MgH_2$ composite starts to decompose at 320 °C and releases 8.1 wt % hydrogen when heated up to 400 °C. From the DSC and TGA results in Figure 3.1, $Ca(BH_4)_2 + MgH_2$ seems to undergo a single-step dehydrogenation reaction.

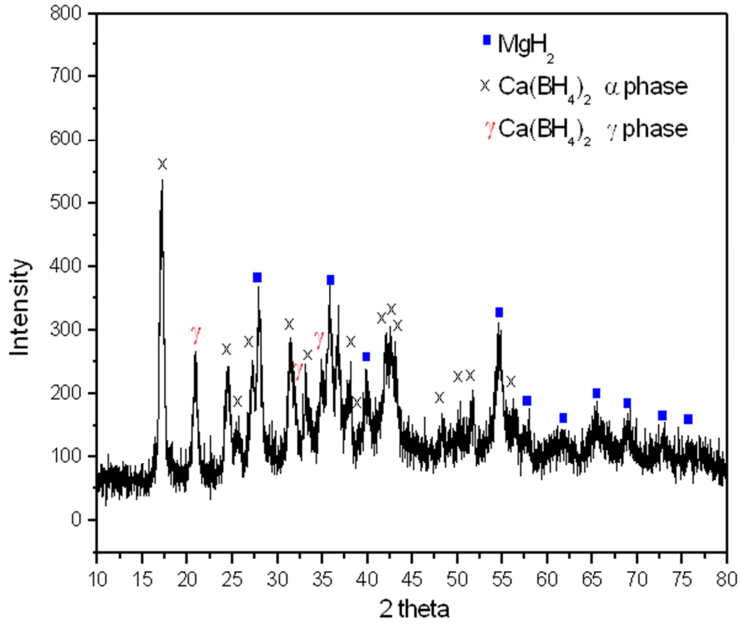

Fig. 3.1. X-ray diffraction (XRD) pattern of the as-milled $Ca(BH_4)_2$ + MgH_2 sample

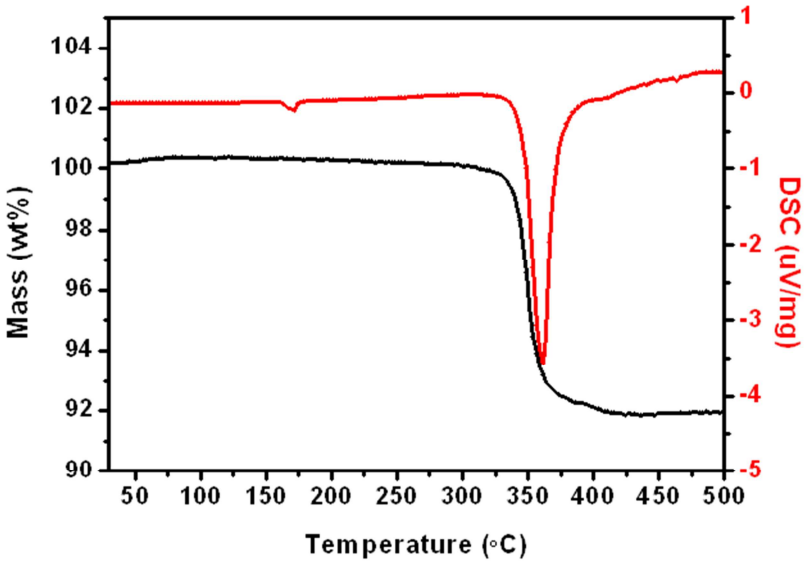

Fig. 3.2. DSC curve (red line) and TG curve (black line) of $Ca(BH_4)_2$

3.3.2. Thermodynamic Assessment of the Dehydrogenation Reactions of $Ca(BH_4)_2 + MgH_2$ Composite

$Ca(BH_4)_2 + MgH_2$ composite release 8.1 wt% hydrogen when heated upto 400 °C. Three possible dehydrogenation reactions can be considered:

$$Ca(BH_4)_2 + MgH_2 \rightarrow 2/3\ CaH_2 + 1/3\ CaB_6 + Mg + 13/3H_2 \quad (12)$$

$$Ca(BH_4)_2 + MgH_2 \rightarrow CaH_2 + MgB_2 + 4H_2 \quad (13)$$

$$Ca(BH_4)_2 + MgH_2 \rightarrow CaH_2 + 2B + Mg + 4H_2 \quad (14)$$

Boron takes a different form in all three cases, and through which reaction hydrogen is released can have a meaningful effect on the reversibility of this composite system. The first question to answer is which reaction is thermodynamically most favorable. Reaction 13 will always be more favorable than reaction 14 since the standard free energy of formation of MgB_2 is negative. Between reactions 12 and 13, there could be a subtle competition depending on hydrogen pressure and temperature. The inspection of the number of hydrogen molecules released tells us that higher temperature and low hydrogen pressure will favor reaction 12. The free energy change of the following reaction will determine which reaction pathway would be taken:[38]

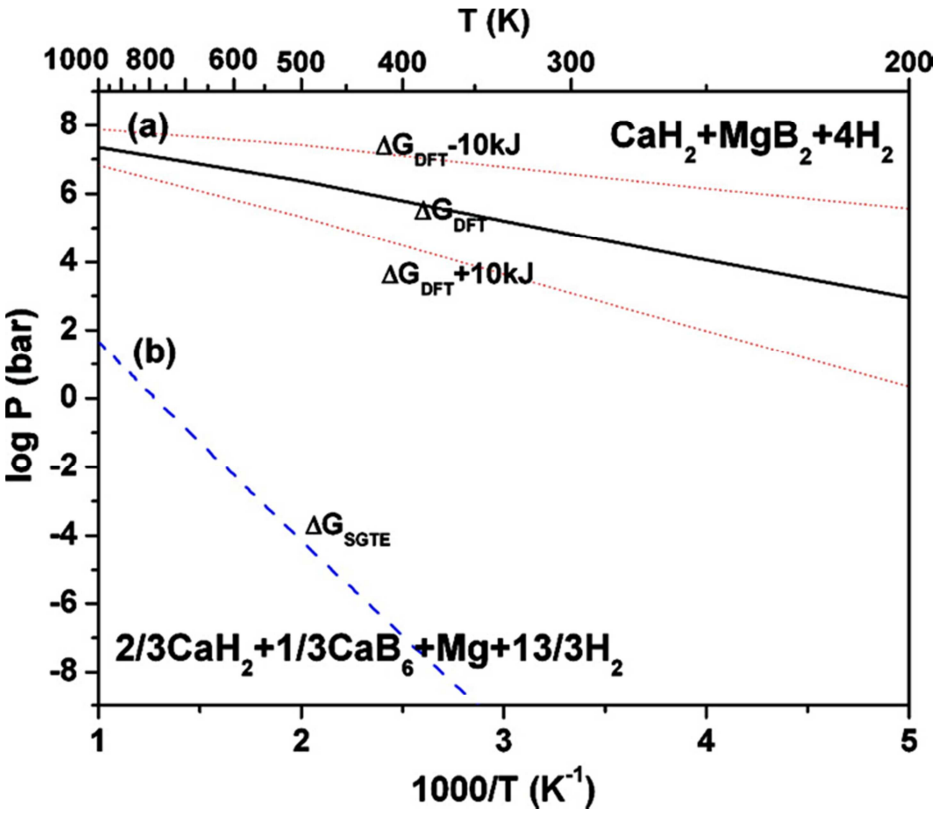

Fig 3.3. Stability region of 2/3 CaH_2 + 1/3 CaB_6 + 13/3 H_2 + Mg and CaH_2 + MgB_2 + $4H_2$ as a function of hydrogen pressure and temperature from (a) first-principles calculations (solid black line) and (b) SGTE thermodynamic database (dashed blue line). The lines indicate the temperature and hydrogen pressure condition where the free energies of the two dehydrogenated products are the same, i.e., $\Delta G = 0$ in reaction 15. The red lines show possible change in the equilibrium pressure when an error of ±10 kJ/mol H_2 in ΔG is considered in DFT calculations.

$$CaH_2 + 3MgB_2 \leftrightarrow CaB_6 + 3Mg + H_2 \quad (15)$$

Figure 3.3 shows van't Hoff plot for reaction 15, predicted by first-principles calculations and by SGTE thermodynamic database.[38] First-principles calculation predicts that reaction 12 is favored under 1 bar of hydrogen pressure at 350 °C, i.e., $Ca(BH_4)_2$ and MgH_2 would dissociate separately,[93] but SGTE predicts the opposite.[38] The deviation between the two predictions is appreciable, and to find out the source of discrepancy we summarize in Table 3.1 ΔH and ΔS of reaction 15 and of each constituent. It can be immediately seen that the enthalpy of formation of MgB_2 differs by 28 kJ/mol between ab initio calculation and the experimental result by Liu et al.[94] Since the formation energy of MgB_2 enters three times in reaction 15, this is the main source of disagreement. It is difficult to say which one is more reliable. Experimental formation energies of borides often show a rather large scattering, and here the Gibbs energy function of MgB_2 was obtained by fitting to a data set that varies as large as 30 kJ/mol,[94] which cannot guarantee the required accuracy. First principles calculation has its own limitation: for example, the dissociation temperature of $Ca(BH_4)_2$ is predicted to be about 100 °C,[93] while the experimental value is about 300 °C.[58, 59, 73] However, even after taking into account an error of (10 kJ/mol H_2)[95] in DFT results, the deviation still remains significant. To better understand the thermodynamics of this composite system, reevaluation of the Gibbs energy

Table 3.1 Standard Enthalpy nad Entropy Change under 1 bar of Hydrogen Pressure at 25 °C and the Temperature at Which the Equilibrium Hydrogen Pressure Becomes 1 Bar[38]

Reaction	$\Delta H°_{DFT}$ (J/K·mol H_2)	$\Delta S°_{DFT}$ (J/K·mol H_2)	T_{DFT} (℃)	$\Delta H°_{SGTE}$ (J/K·mol H_2)	$\Delta S°_{SGTE}$ (J/K·mol H_2)	T_{SGTE} (℃)
$Ca(BH_4)_2 \leftrightarrow 2/3\ CaH_2 + 1/3\ CaB_6 + 10/3\ H_2$	40.6	109.3	98			
$Ca(BH_4)_2 \leftrightarrow CaH_2 + B + 3\ H_2$	57.3	105.7	263			0.31
$Ca(BH_4)_2 + MgH_2 \leftrightarrow 2/3\ CaH_3 + 1/3\ CaB_6 + Mg + 13/3\ H_2$	45.0	114.4	120	144	131	
$Ca(BH_4)_2 + MgH_2 \leftrightarrow CaH_2 + MgB_2 + 4H_2$	46.9	110.1	151	0.31	0.31	
$Ca(BH_4)_2 + MgH_2 \leftrightarrow CaH_2 + 2B + Mg + 4\ H_2$	57.9	112.0	238			
$MgH_2 \leftrightarrow Mg + H_2$	59.7	131.2	179	75.7	132.3	288
$CaH_2 + 3MgB_2 \leftrightarrow CaB_6 + 3Mg + H_2$	22.2	166.3	-148	104.9	128.8	508
$CaH_2 \leftrightarrow Ca + H_2$	173.1	136.0		177.0	130.9	1017
$Mg + 2B \leftrightarrow MgB_2$	-43.9	-8.0		-72.1	1.0	
$Ca + 6B \leftrightarrow CaB_6$	-289.8	6.2		-288.4	1.3	
$4CaH_2 + 3MgH_2 \leftrightarrow Ca_4Mg_3H_{14}$	1.3	14.5				

function of MgB_2 is necessary. In the case of CaB_6, Shang et al.[96] recently argued that experimental stability of CaB_6 is largely underestimated compared to other

divalent alkaline-earth hexaborides and provided a new Gibbs energy function obtained by ab initio quasiharmonic calculation. We adopted their Gibbs energy function instead of the one in the SGTE database. Although it is not at all conclusive, there could be a chance of close competition between reactions 12 and 13 under usual experimental conditions. For example, at 350 °C the SGTE result predicts that dehydrogenation under 1 bar of hydrogen would see the formation of MgB_2 whereas dynamic vacuum condition would find CaB_6.

In order to find out details of the decomposition path, the sample was prepared by heating $Ca(BH_4)_2 + MgH_2$ at 400 °C. The XRD data of the final dehydrogenated sample is plotted in Figure 3.4. The XRD peaks are mainly from CaH_2 and Mg. Rietveld refinement where lattice parameter and crystallite size are fitted to 4.12 Å (4.15 Å from CaB_6 reference) and 3 nm, respectively. Although it is not as clear as in Figure 3.4, we can observe that the Raman spectroscopy is employed to find out boron-containing compound in the final dehydrogenated sample. Raman spectroscopy is employed to find out boron-containing compound, and the result is shown in Figure 3.5. CaB_6 is found instead of MgB_2. We again point out that because of uncertainty in thermodynamic data, it is not clear whether our experimental conditions would favor the formation of CaB_6 or not. If MgB_2 is a more stable specie at

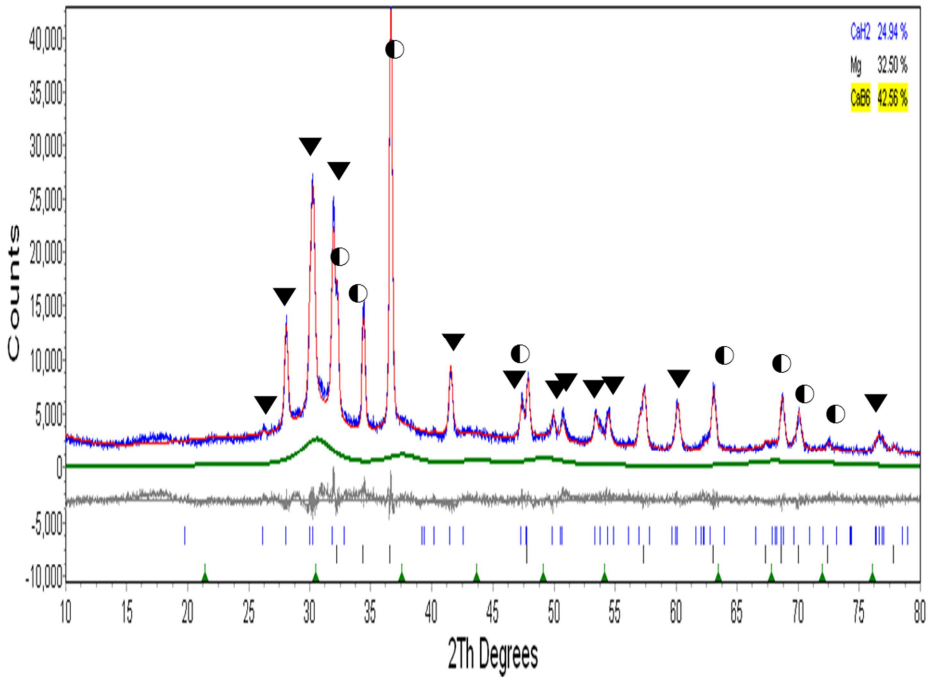

Fig 3.4. XRD patterns of $Ca(BH_4)_2$ + MgH_2 composite after dehydrogenation at 400 °C. The green line indicates the broad background coming from nanocrystalline CaB_6, and red line indicate the fitted data by reitveld refinement.

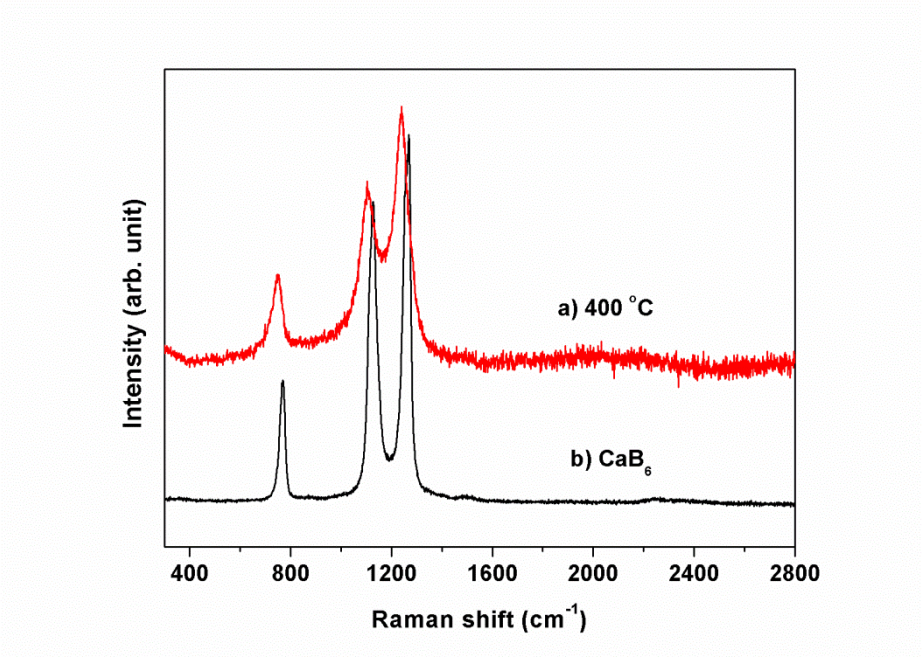

Figure 3.5. Raman spectra of $Ca(BH_4)_2 + MgH_2$ composite after dehydrogenation at 400 °C. The Raman spectrum of CaB_6 reference is compared in b).

the given condition, formation of CaB_6 can be explained by short-range mass transport required when forming Ca-B compound since both Ca and B are from $Ca(BH_4)_2$, whereas formation of MgB_2 would require a longer-range diffusion of Mg or B. Reasoning from what we have found in XRD and Raman data, the reaction 12 to form CaB_6, CaH_2, and Mg can be summarized as decomposition reaction of $Ca(BH_4)_2 + MgH_2$.

The excess amount of MgH_2 would transforms to Mg at the initial dissociation stage.

$$MgH_2 \rightarrow Mg + H_2 \quad (16)$$

Now we turn our attention to the role of MgH_2. If we simply compare the dehydrogenated product of $Ca(BH_4)_2 + MgH_2$ composite with that of the individual constituents, $Ca(BH_4)_2$ and MgH_2, we may conclude that there is no interaction between $Ca(BH_4)_2$ and MgH_2 because CaB_6 was formed instead of MgB_2, which is better described by reaction 12. Note that reaction 12 is a simple sum of reactions 1 and 16. The most important change made by MgH_2 is that the intermediate compound appearing in decomposition of pure $Ca(BH_4)_2$ was not found in the case of $Ca(BH_4)_2 + MgH_2$, which removes the highest-temperature endothermic peak in Figure 3.2, thereby lowering the end point of decomposition. In short, MgH_2 (or Mg) changes the decomposition path instead of the decomposition product, like a catalyst does. A 1:1 ratio of $Ca(BH_4)_2$ to MgH_2 derived from reaction 13 might not be so meaningful if

MgH_2 really behaves like a catalyst, and a small amount of MgH_2 is desirable since it will increase the overall hydrogen capacity. Therfore, we prepared the sample, $2Ca(BH_4)_2 + MgH_2$ composite, and the dehydrogenation reaction path was investigated in part 3.3.3.

3.3.3. Dehydrogenation Reactions of $2Ca(BH_4)_2 + MgH_2$ Composite

Figure 3.6 shows the *in situ* SR-PXD patterns of $Ca(BH_4)_2 + MgH_2$ composite for the temperature range between 329 and 384 °C. At around 330 °C, the intensity of the β-$Ca(BH_4)_2$ starts to decrease rapidly. $Ca_4Mg_3H_{14}$ peaks appeared with decreasing β-$Ca(BH_4)_2$, reaching to the maximum at 340 °C, and gradually get depleted as the temperature was raised to 380 °C. Formation of CaH_2 took place soon after, and this material increased in the range between 335 and 400 °C, coinciding with the decrease of $Ca_4Mg_3H_{14}$. From *in situ* SR-PXD results, the dehydrogenationo path can be summarized as follows:

$$2Ca(BH_4)_2 + MgH_2 \rightarrow 1/3\ Ca_4Mg_3H_{14} + 2/3\ CaB_6 + 20/3\ H_2$$

$$\rightarrow 4/3\ CaH_2 + Mg + 2/3\ CaB_6 + H_2 \qquad (17)$$

It is not clear whether MgH_2 directly reacts with $Ca(BH_4)_2$ to form $Ca_4Mg_3H_{14}$ or reaction 1 precedes and the product, CaH_2, combines with Mg or MgH_2 to form $Ca_4Mg_3H_{14}$. The last stage is dissociation of $Ca4Mg_3H_{14}$:

$$Ca_4Mg_3H_{14} \rightarrow 4CaH_2 + 3Mg + 3H_2 \qquad (18)$$

$Ca_4Mg_3H_{14}$ dissociates at a higher temperature than MgH_2 since the Helmholtz free energy change of the following reaction is predicted to be slightly negative by our first-principles calculations implying that the activity

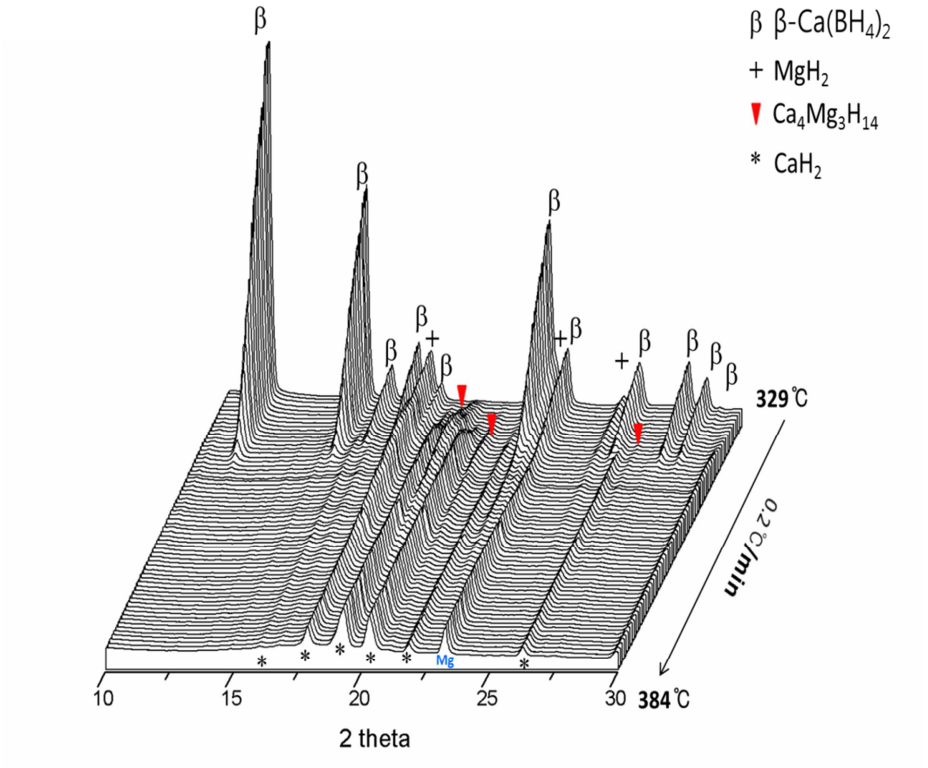

Fig. 3.6. *In situ* SR-PXD patterns (wavelength = 0.998398 Å) of $Ca(BH_4)_2$. The sample was heated (0.2 °C/min) under 1 bar H_2 pressure from 300 to 384 °C. Symbols; β, cross, red inversed triangle, asterisk, and Mg present β-$Ca(BH_4)_2$, MgH_2, $Ca_4Mg_3H_{14}$, CaH_2, and Mg, respectively.

of MgH_2 is lowered by forming $Ca_4Mg_3H_{14}$.

$4CaH_2 + 3MgH_2 \rightarrow Ca_4Mg_3H_{14}$

$$\Delta F = - 7.9 \text{ kJ at } 350 \text{ °C} \quad (19)$$

In the *in situ* SR-PXD, another point can be extract, which is similar with the case of pure $Ca(BH_4)_2$. The peak intensity of $Ca_4Mg_3H_{14}$ is, relatively weak when compared to those of starting materials, β-$Ca(BH_4)_2$ and MgH_2. The result shows that the crystalline phase β-$Ca(BH_4)_2$ + MgH_2 composite cannot be explained by the $Ca_4Mg_3H_{14}$ formation in the crystalline phase, indicating the presence of amorphous phases in the sample. Recently, the formation of $CaB_{12}H_{12}$ during dehydrogenation of a $Ca(BH_4)_2$ + MgH_2 composite was observed by combining of ^{11}B MAS-NMR and *ex-situ* XRD.[97] Once $CaB_{12}H_{12}$ is formed upon desorption, due to its high stability,[41, 98] it is known that this material does not participate in ther reversible reaction to form $Ca(BH_4)_2$ under mild conditions (~100 bar of H_2).

Chapter 4

Revesiblity of Rehydrogenation/Dehydrogenation Reactions of Both $Ca(BH_4)_2$ and $Ca(BH_4)_2 + MgH_2$ Composite

4.1. Introduction

Reversibility of Ti-catalyzed $NaAlH_4$ reported by Bogdanovic et al.[99] opened up the possibility of adopting complex metal hydrides as hydrogen storage materials. Since then, numerous candidates such as alanates, borohydrides, amides, and their mixtures have been explored,[100-102] yet none of them fully satisfies conditions required for practical on-board applications. Among all the difficulties that need to be overcome to meet the requirements, the most challenging part would be reversible rehydrogenation in a reasonable amount of time. Reversibility is sometimes thermodynamically forbidden when an exothermic process is a part of dehydrogenation, but more often is the case where, even without thermodynamic restriction, slow kinetics limits reversibility in practice

In view of reversibility, $Ca(BH_4)_2$ makes an intriguing case. Kim et al.[103, 104] reported about 50 % rehydrogenation of dehydrogenated of $Ca(BH_4)_2$ under 90 bar of H_2 pressure at 350 °C by adding small amount of

Ti and Nb halides. Ro¨nnebro et al.[76] demostrated ca 4 wt% reversibility of $Ca(BH_4)_2$ by hydrogenating commercial CaB_6 and CaH_2 mixed with catalysts under 700 bar of H_2 pressure at 400 °C. This temperature and pressure condition is much milder than the case of $LiBH_4$. Without additive, however, only 1 wt% of $Ca(BH_4)_2$ was re-hydrided. So far, some of the decomposition products have amorphous character and it has thus been difficult to conclude the decomposition. The poor reversibility might be linked to the formation of stable intermediate phases or side products upon decomposition. In chapter 3 and 4, we have already discussed the final dehydrogenated products and decomposition reaction pathway, so, in this chapter, we will disscuss the relation between dehydrogenation products and reversibility.

Barkhordarian et al.[55] successfully obtained $Ca(BH_4)_2 + MgH_2$ starting from $CaH_2 + MgH_2$ and the hydrogenation reaction proceed completely. However, in previous chapter, we confirmed $Ca(BH_4)_2 + MgH_2$ decomposes to form $CaH_2 + CaB_6 + Mg$. The hydrogenation reaction path and reversibility of $CaH_2 + CaB_6$ +Mg and the role of Mg have not understood. As described before, metal borohydrides usually suffer from slow reaction kinetics during dehydrogenation and rehydrogenation. One of the routes to enhance kinetics is by reducing particle size or changing morphology. Smaller particle size will naturally provide larger area for reactions to proceed, and in extreme cases such as nanoconfinementcould even modify thermodynamics.[105] To control the particle size is not an obvious task

since each and every step, e.g., ball-milling condition, reaction temperature and time, could all play a role in determining the final particle size. Therefore, we investigated on how the reaction kinetics is affected by changing reaction conditions together with clarifying the rehydrogenation reaction path.

4.2. Rehydrogenation Reactions of $Ca(BH_4)_2$ and $Ca(BH_4)_2 + MgH_2$ Composite

4.2.1. The Formation of CaB_6, MgB_2, and B: Reversibility

After discovery of the favorable kinetic property of MgB_2, the experiments were performed mainly with respect to the formation of $Ca(BH_4)_2$ and $LiBH_4$. Evidently, the other borides investigated did not show effects similar to those of MgB_2 (i.e., no borohydride could be formed from them), although B_4C, or pure boron, exhibited lower thermodynamic stability than MgB_2. By this comparison, we present two crystal structures[46] in Figure 4.1, which shows the distinct difference in the boron bondings. MgB_2 (Figure 4.1a) has a layered crystal structure where layers of boron are located between layers of magnesium. This structure is similar to that of graphite except that, in the case of MgB_2, magnesium layers are added between boron layers. Boron atoms in each layer are connected by covalent sp^2 bonds, whereas the interlayer bonds between Mg and boron are of metallic type. Compared to other boron-containing reactants tested, no other compound or element has a similar structure. Pure boron, for example, is mostly available in the form of one of its two polymorphs, α- or β-boron. In both of these polymorphs, the common building blocks are icosahedral units. These units consist of 12 boron atoms, and each atom is connected to five other atoms via covalent bonds. In MgB_2, on the other hand, each boron atom is connected to

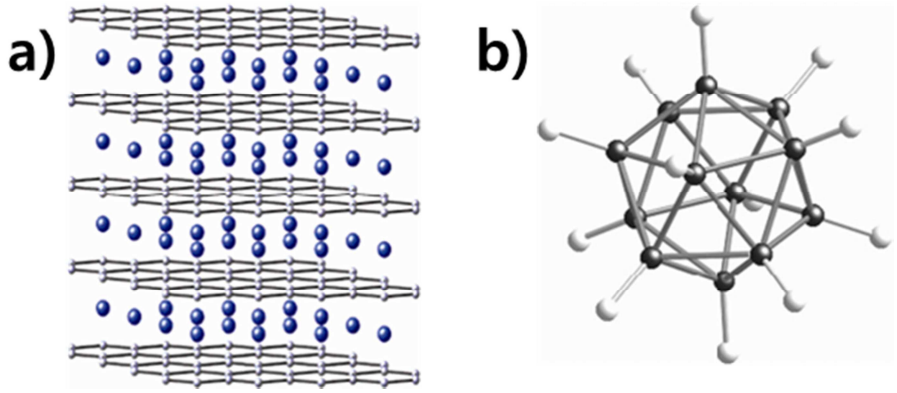

Fig. 4.1. a) Layered structure of B in MgB_2, and b) structure of $[B_{12}H_{12}]^{-2}$ anions in $Li_2B_{12}H_{12}$[46]

a maximum of three other boron atoms. It is well-known that the reactivity of boron depends on its electronic structure, e.g., amorphous boron oxidizes at much lower temperature than the crystalline modification. Therefore, it is reasonable to assume that the reactivity of boron and its compounds depends on the type of boron bonding, the bonding length, and the number of boron neighbors. The DFT-calculated energies[38] required to break these compounds into isolated atoms are 4.76, 6.00, and 6.20 eV/atom for MgB_2, CaB_6, and α-B, respectively. The less energy is needed to detach a boron atom from the boron layers of MgB_2 than other boron forms. In addition, magnesium atoms between boron layers in MgB_2 may also play a role by forming intermediate Mg-B-H bonds. Conversely, it follows that the critical step of the hydrogenation reaction to form complex borohydrides (when starting from pure boron) may be the breakage of the boron bonds, whether they are in pure boron or in an intermediate phase, formed during the reaction.

It is interesting to note that, in the case of pure $LiBH_4$, the intermediate phase during dehydrogenation was shown to be $Li_2B_{12}H_{12}$.[50] The crystal structure of $Li_2B_{12}H_{12}$ consists of $[B_{12}H_{12}]^{-2}$ anions (see Figure 4.1b), in which the boron atoms form icosahedral units, very similar to the icosahedral units in pure boron. The B-B bond lengths in these two structures are also very close, i.e., 1.779-1.811 Å for $[B_{12}H_{12}]^{-2}$ and 1.751-1.806 Å for pure boron. Due to the structural similarity of pure boron and $[B_{12}H_{12}]^{-2}$ complexes, as well as the fact that $Li_2B_{12}H_{12}$ is thermodynamically more

stable than $LiBH_4$ (because it is formed during the dehydrogenation of $LiBH_4$), it may be reasonable to assume that the formation of this phase occurs during the reaction of LiH with B. The intermediate formation of $Li_2B_{12}H_{12}$ may hinder the formation of $LiBH_4$. In turn, besides its higher reactivity, the effect of MgB_2 on the formation of $LiBH_4$ may be explained by the lower chemical potential of B, thus avoiding the formation of this stable intermediate and facilitating the formation of $LiBH_4$ directly.

4.2.2. Reversibility of $Ca(BH_4)_2 + MgH_2$ composite

The formation of CaB_6 instead of a-B can be an important factor in reversibility as is the case for $LiBH_4 + CaH_2$ versus pure $LiBH_4$.[106] Boron ends up with CaB_6 and that higher than 50% reversibility is achieved at relatively milder conditions than $LiBH_4$, the formation of CaB_6 is certainly beneficial for reversibility. CaB_6 may improve reversibility because each B atom is connected to five other B atoms via covalent bond while in α-B each B atom has more than five covalent bondings.

To check the reversibility of the dehydrogenated sample at 400 °C of a $Ca(BH_4)_2 + MgH_2$ composite(see Figure 3.4), we tried rehydrogenation reaction without catalyst under 90 bar of hydrogen pressure at 350 °C for 24 h. The result is shown in Figure 4.1 together with TGA curve of as-milled $Ca(BH_4)_2 + MgH_2$ sample for comparison, and the amount of hydrogen absorbed was measured by TGA. As can be seen in Figure 4.2, the result is very encouraging since 60% reversibility was achieved without catalyst, and we retested whether the same thing can be found for pure $Ca(BH_4)_2$, but the amount of rehydrogenation was negligible even after 48 h under the same temperature and pressure condition. Our tentative conclusion from this result is that Mg (or MgH_2) brings about some catalytic effects during the rehydrogenation reaction.

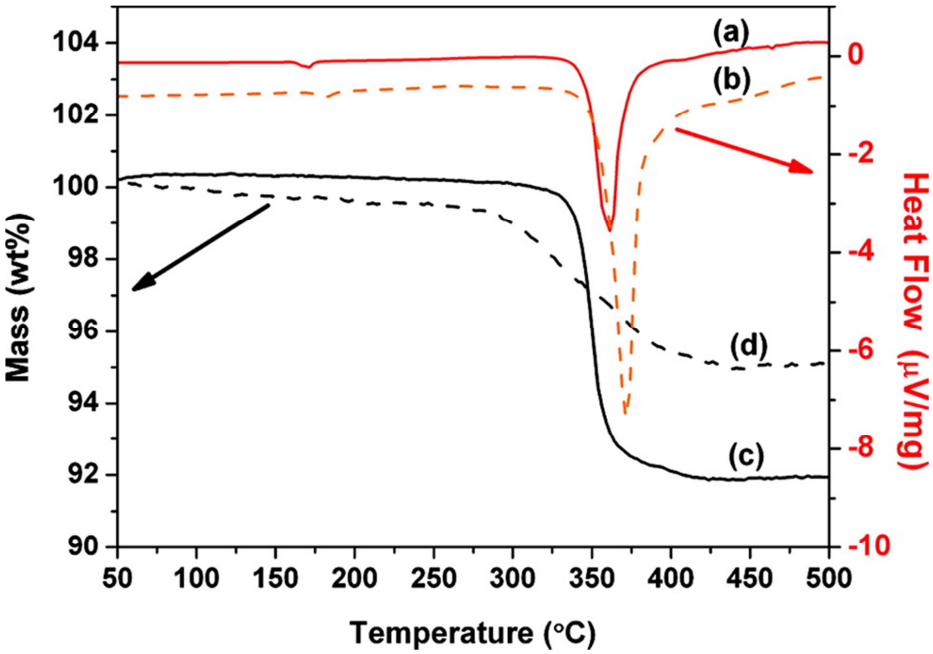

Fig. 4.2. DSC curves of the first dehydrogenation of a) $Ca(BH_4)_2$ + MgH_2 and b) $Ca(BH_4)_2$ + 0.2 Mg composite. TGA curves of c) first and d) second dehydrogenation of $Ca(BH_4)_2$ composite; rehydrogenation was done under 90 bar H_2 pressure at 350 °C for 24 h.

Figure 4.3 shows the evolution of the phase composition with time during hydrogenation of CaH_2 + CaB_6 +Mg mixture, obtained by dehydrogenating $Ca(BH_4)_2$+MgH_2. The initial sample was prepared by heating a mixture of $Ca(BH_4)_2$ and MgH_2 under 1 bar H_2 at 350 °C for 1 h. During hydrogenation, within the first 30 min, Mg was completely hydrogenated to MgH_2. It immediately reacted with CaH_2 to form $Ca_4Mg_3H_{14}$, which completed in about 6 h. In the previous works, it was confirmed that $Ca(BH_4)_2$ could be formed either from CaH_2 and CaB_6 mixture when some catalytic additives are added, [76, 103, 104] or from CaH_2 and MgB_2 mixture with additive.[46] In Figure 4.3, $Ca(BH_4)_2$ did not appear until about 3 h but once it was formed, the amount increased rapidly up to 6 h and then gradually afterwards. The CaH_2 peaks disappeared after 6 h but the intensity of the $Ca(BH_4)_2$ peaks continuously increased up to 24 h, which indicates that $Ca(BH_4)_2$ also was formed from the reaction between $Ca_4Mg_3H_{14}$ and CaB_6.

As the crystal size of CaB_6 is extremely fine in the starting mixture, it is not clearly seen in the XRD pattern, but its existence was already confirmed by Raman spectroscopy under the same experimental conditions (see Figure 3.5). $Ca(BH_4)_2$ might have been formed directly from the reaction between CaH_2 and CaB_6, but as neither catalytic additives nor MgB_2 was present in these samples, this is not likely to have happened. From this observation, the hydrogenation reaction path of a CaH_2 + CaB_6 + Mg mixture can be described as follows:

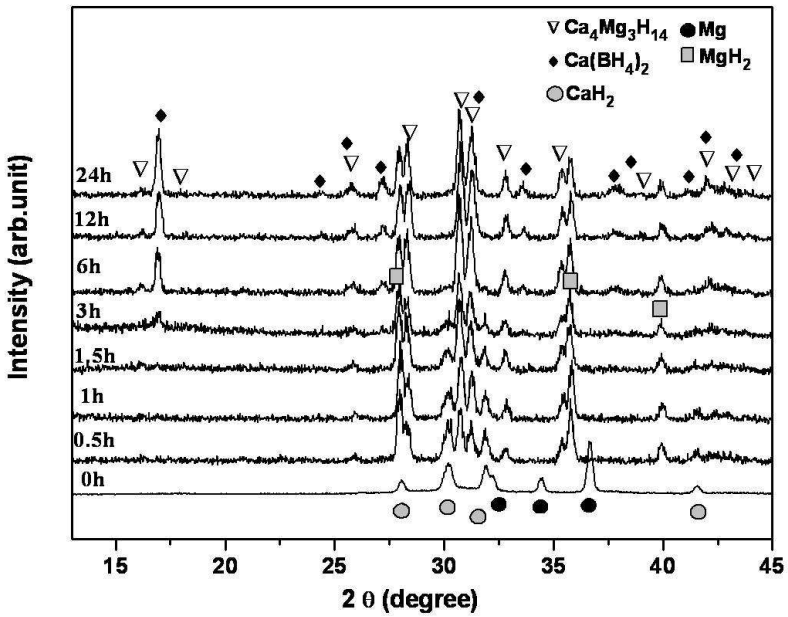

Fig. 4.3. Room temperature XRD patterns of mixed CaH_2 + CaB_6 + Mg samples that had been heated under 90 bar H_2 at 350 °C for different durations.

$$Mg + H_2 \rightarrow MgH_2 \quad (20)$$

$$4/3\ CaH_2 + MgH_2 \rightarrow 1/3\ Ca_4Mg_3H_{14} \quad (21)$$

$$1/3\ Ca_4Mg_3H_{14} + 1/3\ CaB_6 + 10/3\ H_2 \rightarrow 2Ca(BH_4)_2 + MgH_2 \quad (22)$$

The free energy change of reaction 21 has been estimated to be about −3.0 kJ/mol $Ca_4Mg_3H_{14}$ at 25 °C by first-principles calculation.[38] However, the formation of slightly more stable $Ca_4Mg_3H_{14}$ would not hinder the formation of $Ca(BH_4)_2$ since the free energy increase in reaction 22 is only 0.15 kJ/mol H_2. In hydrogenation reaction, Mg might play a role as a catalyst on formation of $Ca(BH_4)_2$. Therefore, we tried to hydrogenate a milled sample of as-received CaH_2 + CaB_6 +Mg mixture, but $Ca(BH_4)_2$ did not form and only $Ca_4Mg_3H_{14}$ and MgH_2 were produced as a result.

Another possibility is that the presence of Mg influences the microstructure of the dehydrogenated product of $Ca(BH_4)_2$+MgH_2 mixture. The particle size of $Ca_4Mg_3H_{14}$ would be fine compared to CaH_2 because it was formed newly by chemical reaction between CaH_2 and hydrogenated Mg. In order to test this possibility, we prepared 6 samples which were treated under different temperatures (see Table 4.1). The reversibility of all samples in Table 4.1 was calculated by comparing the hydrogen content in those samples with that in the starting $Ca(BH_4)_2$+MgH_2 mixture (9.0 wt%) which is slightly less than the theoretical value 9.1 wt%. The TG curves were given in Figure 4.4. The thermogravimetric measurements were repeated up to four

times for each sample and the error in reversibility is less than ±1%. Different reaction temperatures would affect the particle size and microstructure of the products. The reversibility varies strongly between the samples, which highlights the importance of controlling the dehydrogenation and hydrogenation temperature to achieve better reversibility. The reversibility of ca. 60% is particularly encouraging since it was achieved without catalyst and the hydrogen capacity of $Ca(BH_4)_2$+MgH_2 system is as high as 9.09 wt% (see Figure 3.2).We note that dehydrogenation was performed under 1 bar H_2 for 1 h and the dehydrogenated phases of all the samples consisted of CaH_2, CaB_6, and Mg (see Figure 3.4 and 3.5). Figure 4.5 shows the Raman spectra of samples 1 and 2 together with that of reference CaB_6. In Figure 4.5, T_{2g} (768.6cm^{-1}), E_g (1127.0cm^{-1}), and A_{1g} (1268.9cm^{-1}) are Raman active modes of CaB_6 in ascending order. The frequencies corresponding to compounds other than CaB_6 were not found in Raman spectra.

Table 4.1. Dependence of reversibility of $Ca(BH_4)_2$ and MgH_2 mixture on the dehydrogenation and rehydrogenation temperatures. Reversibility: XX/XX* = total reversibility/reversibility of $Ca(BH_4)_2$. The reversibility of $Ca(BH_4)_2$ was calculated assuming that Mg was completely hydrogenated to MgH_2 absorbing theoretical capacity of 7.6 wt%. After subtracting the amount of hydrogen absorbed by Mg, the rest part was then divided by theoretical hydrogen capacity of $Ca(BH_4)_2$.

Sample no	Dehydrogenation temperature (℃)	Hydrogenation temperature (℃) /time (hour)	Reversibility (%)
1	450	350/24h	11.5/0*
2	400	350/24h	54.7/43.2*
3	400	350/48h	57.5/46.0*
4	400	350/24+24h*	65.6/54.1*
5	400	300/24h	43.7/32.2*
6	400	400/24h	51.9/40.4*

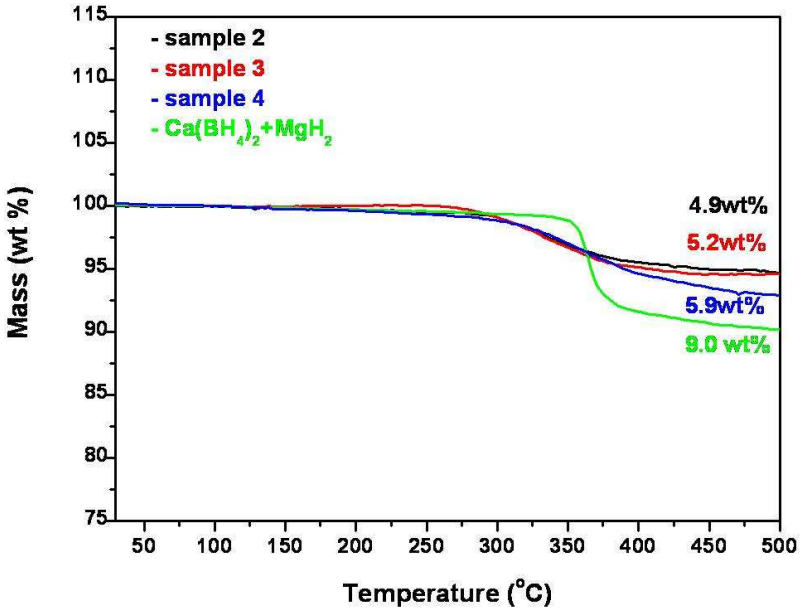

Fig. 4.4. TG curves of samples 2, 3, and 4 were given together with the $Ca(BH_4)_2 + MgH_2$ mixture.

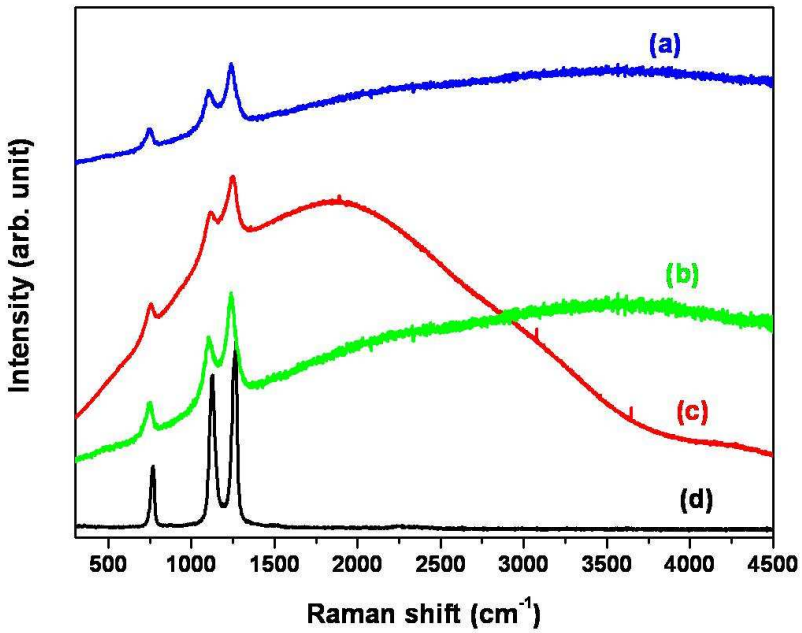

Fig. 4.5. Raman spectra of a) sample 1 dehrogenated at 450 °C, b) sample 2 dehydrogenated at 400 °C, c) sample 2 hydrogenated at 350 °C, and d) reference CaB_6

The phase compositions of the hydrogenation/dehydrogenation products of sample 1 were also analyzed by XRD. From Raman and XRD data, it is confirmed that the final dehydrogenation products of samples 1 and 2 after dehydrogenation are exactly same (see Figure 4. 5a and b, Figure 4.3(0 h), and Figure 4. 6b). $Ca_4Mg_3H_{14}$ and MgH_2 were shown as hydrogenated products of sample 1. $Ca(BH_4)_2$ was not formed and only Mg was hydrogenated to MgH_2. After hydrogenating Mg, subsequently MgH_2 reacted with CaH_2, thereby forming $Ca_4Mg_3H_{14}$. The reversibility of sample 1 was 11.5%, and when we compare the result from sample 2 (see Table 2), apparently an increase in the dehydrogenation temperature of only 50K from 673K to 723K resulted in a dramatic change in the reversibility. Higher dehydrogenation temperature would probably promote the formation of coarser CaH_2, Mg, and CaB_6 in particular during the dehydrogenation process. In most solid–solid–gas reaction systems, it is quite common that the larger the size of the reactants, the slower the reaction kinetics as the contact area between the solid reactant particles decreases with increasing particle size. This might be the reason why $Ca(BH_4)_2$ was not formed in sample 1. As Mg was readily hydrogenated to MgH_2 and subsequently reacted with CaH_2 to form $Ca_4Mg_3H_{14}$, it is most likely that the particle size of CaB_6.

4.2.3. Reversibility of Intermediate Phases of $Ca(BH_4)_2$

The reversibility of the intermediate phase has not been reported yet, although the hydrogenation from $CaH_2 + CaB_6$ to $Ca(BH_4)_2$ with some atalytic additives has been reported.[46, 76, 103, 104] The XRD pattern obtained after rehydrogenating the sample dehydrogenated at 345 °C is given in Figure 4.6. The rehydrogenation was done under 90 bar of hydrogen at 330 °C for 24 h. The rehydrogenation products are α- and β-$Ca(BH_4)_2$ and some CaH_2 together with a trace of $Ca_3(BH_4)_3(BO_3)$,[107] whereas CaB_2H_x disappears completely during the rehydrogenation. The most remarkable thing is that CaB_2H_x is almost fully rehydrogenated without any catalytic additive. When we also tried the rehydrogenation reaction under 50 bar of hydrogen, almost the same result was obtained (not shown here). The peaks of CaH_2 are seen from the grain growth of nanocrystalline or amorphous CaH_2, which were presumably present in the sample before rehydrogenation, during the sample being hydrogenated at relatively high temperature for 24 h. Figure 4.7 presents a ^{11}B NMR spectra of the rehydrogenated sample. The presence of α- and β-$Ca(BH_4)_2$ is indicated by the two separate peaks near −30 ppm, which is consistent with the XRD result. At the same time, the reduction of the CaB_6 peak is clearly noticeable, indicating the partial rehydrogenation reaction of CaB_6 with CaH_2 into $Ca(BH_4)_2$. In reality, it has never been reported that the rehydrogenation reaction from CaH_2 and CaB_6 hardly occurs without any

catalytic additive. Long-range diffusion has been believed to be the main obstacle for the hydrogenation reaction between CaH_2 and CaB_6. However, our NMR result implies that the rehydrogenation reaction of CaB_6 can take place, at least partially, without any catalytic additives and at mild conditions. This is presumably because the crystallite size of CaB_6 and CaH_2 is extremely small in the sample dehydrogenated at relatively low temperatures. Boron oxide contaminants are also seen in the 0−20 ppm region, which agrees with the formation of $Ca_3(BH_4)_3(BO_3)$ observed by the XRD. The broad peak at −18 ppm experiences no significant change after the rehydrogenation, idicating that rehydrogenation of $CaB_{12}H_{12}$ is kinetically hindered similarly to $MgB_{12}H_{12}$.[108] The minor reduction in the signal strength could explain the reduction of CaB_2H_x as its ^{11}B NMR signal was hidden in the region.

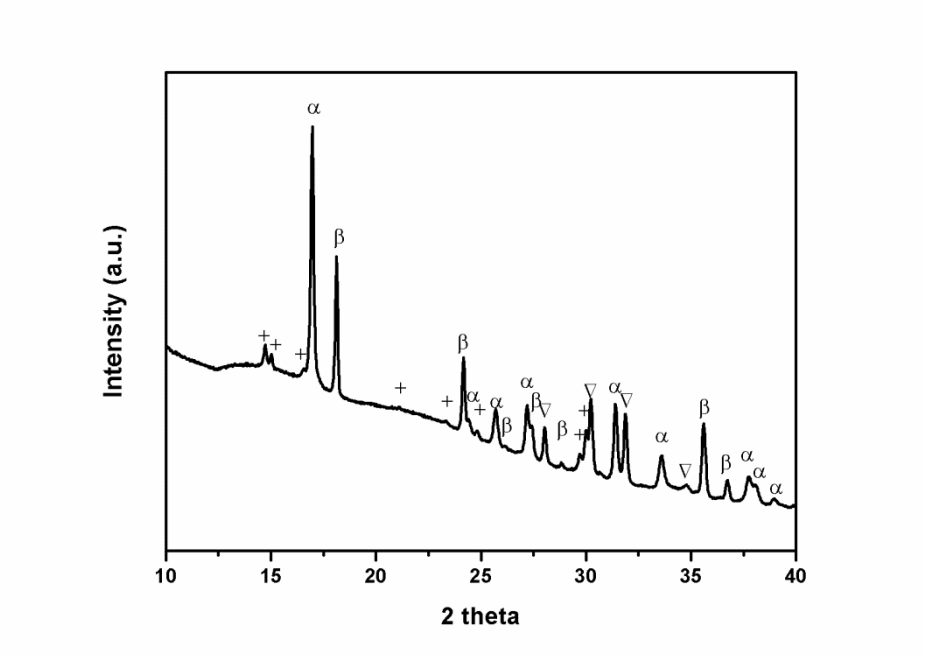

Fig. 4.6. XRD pattern after rehydrogenation at 90 bar of hydrogen and 330 °C for 24h. The sample was initially dehydrogenated at 345 °C. Symbols α and β represent α- and β-$Ca(BH_4)_2$, respective ely. The inverted triangle and cross symbols represent CaH_2 and $Ca_3(BH_4)_3(BO_3)$, respectively.

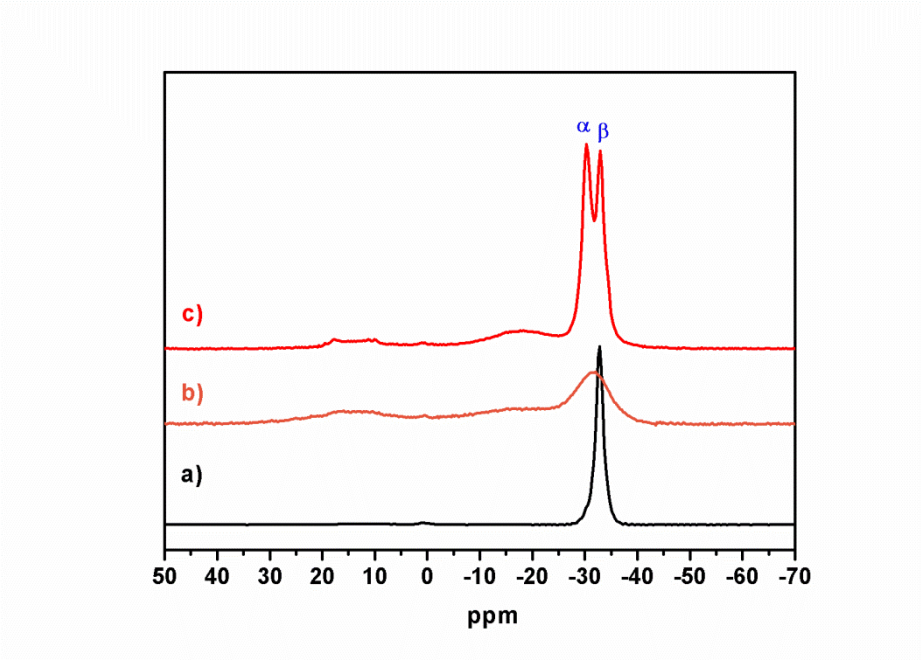

Fig. 4.7. ^{11}B MAS NMR spectra of a) β- $Ca(BH_4)_2$, b)after desorption, and c) after reabsorption

Chapter 5

Conclusions

The decomposition path and reversibility of $Ca(BH_4)_2$ and $Ca(BH_4)_2$ + MgH_2 composite using *ex situ* and *in situ* X-ray diffraction, thermal analysis (TG and DSC), and Raman and NMR spectroscopy. Formation of CaB_6 during dehydrogenation of both systems was confirmed. CaB_6 appears as broad peaks in X-ray diffraction data, but Raman and ^{11}B MAS NMR spectroscopy unambiguously captures the existence of CaB_6. Reversibility of catalyzed $Ca(BH_4)_2$ was previously reported, and here we demonstrate reversibility of $Ca(BH_4)_2$ + MgH_2 composite and $Ca(BH_4)_2$. Dehydrogenated product of $Ca(BH_4)_2$ + MgH_2 is composed of CaH_2, CaB_6, and Mg. About 60% reversibility was achieved after rehydrogenation for 24 h under 90 bar of hydrogen pressure at 350 °C even without the help of catalysts, which makes a good contrast with the case of pure $Ca(BH_4)_2$ where almost negligible dehydrogenation occurs under the same conditions. To understand the difference, the role of Mg in rehydrogenation is worth further investigation. Formation of CaB_6 seems critical in the reversibility of $Ca(BH_4)_2$ containing systems; thecase of other borohydrides is compared.

Dehydrogenation and rehydrogenation reaction routes of both $Ca(BH_4)_2$ and a $Ca(BH_4)_2$ + MgH_2 composite are investigated. For a pure

$Ca(BH_4)_2$, β-$Ca(BH_4)_2$ gradually transforms into the (XRD invisible) amorphous phase at the initial stage. Upon further heating, it decomposes into CaB_2H_x or $CaB_{12}H_{12}$, indicating that there is a subtle competition between two different dehydrogenation routes: (i) $Ca(BH_4)_2 \rightarrow$ amorphous phase $\rightarrow$ $CaB_2H_x + (4 - x)/2H_2 \rightarrow 2/3CaH_2 + 1/3CaB_6 + 10/3H_2$ and (ii) $Ca(BH_4)_2 \rightarrow$ amorphous phase $\rightarrow 1/6CaB_{12}H_{12} + 5/6CaH_2 + 13/6H_2$. It has also been concluded that CaB_2H_x as well as the $CaB_6 + CaH_2$ mixture can be rehydrogenated at 330 °C under 90 bar of hydrogen without any catalytic additive, whereas $CaB_{12}H_{12}$ hardly rehydrogenated under the same conditions.

Among the intermediate phases, it is known that CaB_2H_x is fully reversible, while the more stable $CaB_{12}H_{12}$ with an icosahedral structure hinders reversible reactions. Here, we try to control the dehydrogenation reaction pathway of $Ca(BH_4)_2$ by applying different hydrogen back pressures. The decomposition reaction of $Ca(BH_4)_2$ in the absence of a catalyst was found to be sensitive to the H_2 back pressure. At $p(H_2)$=1 bar, $Ca(BH_4)_2$ decomposes via two competitive dehydrogenation reaction routes to form CaB_2H_x or $CaB_{12}H_{12}$. At $p(H_2)$=10 bar, the overall dehydrogenation reaction remains unchanged. However, the formation of CaB_2H_x is reduced, and amorphous elemental boron is observed as a final dehydrogenation product. At $p(H_2)$=20 bar, the elemental boron formation is significantly increased, and the formation of CaB_2H_x phase is suppressed.

The hydrogenation reaction sequence starting from the dehydrogenated product $CaH_2 + CaB_6 + Mg$ was thoroughly followed using X-ray diffraction, and that can be summarized as (i) $Mg+H_2 \rightarrow MgH_2$, (ii) $4CaH_2 + 3MgH_2 \rightarrow Ca_4Mg_3H_{14}$, (iii) $Ca_4Mg_3H_{14} + 2CaB_6 + 20H_2 \rightarrow 6Ca(BH_4)_2 + 3MgH_2$. The steps (i) and (ii) proceeded rather fast, and the total amount of reabsorbed hydrogen was governed by the step (iii). The kinetics of the step (iii) was critically affected by the temperature of dehydrogenation/hydrogenation reaction, which we mainly attributed to the microstructure of the dehydrogenated product such as particle size. We indirectly proved our hypothesis by showing that inserting high-energy ball-milling process during hydrogenation is more effective than simply increasing the reaction time. Optimal reversibility was achieved from the sample which was dehydrogenated at 400 °C and hydrogenated at 350 °C.

References

[1] Jean-Marie Martin-Amourous, IEPE, Grenoble, France, private communication (2003).

[2] A.D. Kulkarni, L.-L. Wang, D.D. Johnson, D.S. Sholl, J.K. Johnson, Journal of Physical Chemistry C, 114 (2010) 14601-14605.

[3] H2ydropole, http://www.hydropole.ch/index.php?go=hydrogen_carrier.

[4] C.W. Michael Felderhoff, Rittmar von Helmolt, and Ulrich Eberle, Phys. Chem. Chem. Phys., 9 (2007) 2643-2653.

[5] A. Teoh, http://www.greenprospectsasia.com, june 30 (2011).

[6] T.K.N. Line H. Rude, Dorthe B. Ravnsbæ, Ulrike Bösenberg, Morten B. Ley, Bo Richter, Lene M. Ambjerg, Martin Dornheim, Yaroslav Filinchuk, Flemming Besenbacher, and Torben R. Jensen, Phys. Status Solidi A, 208 (2011) 1754-1773.

[7] http://victoriastaffordapsychicinvestigation.wordpress.com, (2012) 10/16.

[8] J.J. Reilly, Z. Phys Chem. N. F.,, 117 (1972).

[9] B.R. Berube, G. Dresselhaus, M. , Int. J. Energ. Res., 31 (2007).

[10] D.R. Chandra, J. J., Chellappa, R., JOM, 58 (2006).

[11] M. Fichtner, Adv. Eng. Mater., 7 (2005).

[12] W. Grochala, Edwards, P.P., Chem. Rev. , 104 (2004).

[13] H. Kohlmann, Metal hydrides, in Encyclopedia of Physical Science and Technology, Academic press, San diego, 2002.

[14] A. Leon, Green Energy and Technology, Springer, 2009.

[15] A.J. Maeland, Hydrides for ohydrogen storage, in rRecent Advances in Hydride Chemistry, in, Elsevier, 2001, pp. 531.

[16] A.K. Pundt, R. , Adv. Eng. Mater., 7 (2006).

[17] A.K. Pundt, R., Annu. Rev. Mater. Res., 36 (2006).

[18] B. Sakintuna, Lamari-Darkrim, Farida, Hirscher, Michael. , Int. J. hydrogen Eneregy 32 (2007).

[19] F. Schuth, Bogdanovic, B., Felderhoff, M., Chem. Commun., (2004).

[20] A.W.C. Van den Berg, Arean, C.O., Chem. Commun., (2008).

[21] R.A. Varin, Czujko, T., Wronski, Z. S., Nanomaterials for solid state hydrogen storage, Springer, 2009.

[22] A. Zuttel, Mater. Today, , 6 (2003).

[23] A. Zuttel, Naturwissenschaften, 91 (2004).

[24] G.G. Libwitz, The hydrogen storage materials, batteries, and electrchemistry,, in: S.S. D.A. Corrigan (Ed.) Electrochemical Society,

Arizona, 1991, pp. 3.

[25] G.G. Libowitz, The solid-state chemistry of binary metal hydrides, , W.A. Benjamin,, New York.

[26] D.G. Ivey, Northwood, D. O., J. Mater Sci., 18 (1983).

[27] A.J. Maeland, Hydrides for energy storage, , in: A.J.M. A. F. Andresen (Ed.) Pergamon, Norway, 1977.

[28] B. Bogdanovic, Schwickardi, M., J. Alloys compd., 253-254 (1997) 1.

[29] G.G. Ch. Lexcellent, Intermetallics, 15 (2007) 934-044.

[30] L. Schlapbach, Anderson, I., Burger, J.P., Hydrogen in metals, in: K.H.J. Buschow (Ed.) Electronic and Magnetic properties of ometals and ceramics part 2, VCH, Weinheim, 1994, pp. 271.

[31] M. Yamaguchi, Akiba, E. , Ternary hydrides, in: Electronic and Magnetic Properties of oMetals and Ceramics part 2, VCH, Weinheim, 1994, pp. 333.

[32] K.M. Y. Nakamor, A. Ninomiya, H. Li, N. Ohba, S. Towata, A. Zuttel S. Orimo, , Phys. Rev. B, 74 (2006).

[33] K.O. Miwa, N. Towata, S. Nakamori, Y. Zuttel, A. Orimo, S., J. Alloys Compd., 446-447 (2007).

[34] H.E. Kissinger, Anal. Chem, 29 (1957).

[35] C. Bonatto Minella, S. Garroni, C. Pistidda, R. Gosalawit-Utke, G. Barkhordarian, C. Rongeat, I. Lindemann, O. Gutfleisch, T.R. Jensen, Y. Cerenius, J. Christensen, M.D. Baró, R.d. Bormann, T. Klassen, M. Dornheim, The Journal of Physical Chemistry C, 115 (2011) 2497-2504.

[36] J.-H. Kim, S.-A. Jin, J.-H. Shim, Y.W. Cho, Journal of Alloys and Compounds, 461 (2008) L20-L22.

[37] Y. Kim, S.-J. Hwang, J.-H. Shim, Y.-S. Lee, H.N. Han, Y.W. Cho, The Journal of Physical Chemistry C, 116 (2012) 4330-4334.

[38] Y. Kim, D. Reed, Y.-S. Lee, J.Y. Lee, J.-H. Shim, D. Book, Y.W. Cho, Journal of Physical Chemistry C, 113 (2009) 5865-5871.

[39] J.Y. Lee, D. Ravnsbak, Y.-S. Lee, Y. Kim, Y. Cerenius, J.-H. Shim, T.R. Jensen, N.H. Hur, Y.W. Cho, Journal of Physical Chemistry C, 113 (2009) 15080-15086.

[40] M.D. Riktor, M.H. Sørby, K. Chłopek, M. Fichtner, B.C. Hauback, Journal of Materials Chemistry, 19 (2009) 2754.

[41] L.-L. Wang, D.D. Graham, I.M. Robertson, D.D. Johnson, Journal of Physical Chemistry C, 113 (2009) 20088-20096.

[42] V. Stavila, J.-H. Her, W. Zhou, S.-J. Hwang, C. Kim, L.A.M. Ottley, T.J. Udovic, Journal of Solid State Chemistry, 183 (2010) 1133-

1140.

[43] G. Barkhodarian, Klasse, T., Bormann, R., in: P.I. Patent (Ed.) Pending International Patent, 2006.

[44] T.K. G. Markhordarian, R. Bormann, J. Alloys Compd., 440 (2006) L18.

[45] F.O.M. J. J. Vajo, S.L. Skeith, M.P. Balogh, in: P.I. Patent (Ed.) Pending International Patent, 2005.

[46] G. Barkhordarian, T.R. Jensen, S. Doppiu, U. Bosenberg, A. Borgschulte, R. Gremaud, Y. Cerenius, M. Dornheim, T. Klassen, R.d. Bormann, Journal of Physical Chemistry C, 112 (2008) 2743-2749.

[47] Y.N. S. Orimo, G.Kitahara, K. Miwa, N.Ohba, S. Towata, A. Zűttel, J. Alloys Compd., 404-406 (2005) 427-430.

[48] F.B. Philippe Mauron, Oliver Friedrichs, Arndt Remhof, Michael Bielmann, Christoph N. Zwicky, and Andreas Zűttel, J. Phys. Chem. B, 112 (2008) 906-910.

[49] F.M. John J. Vajo, Channing C. Ahn, Robert C. Bowman, Jr., and Brent Fultz, Journal of Physical Chemistry B, 108 (2004) 13977-13938.

[50] Y.N. Shin-Ichi Orimo, Nobuko Ohba, Kazutoshi Miwa, Masakazu Aoki, Shin-ichi Towata, Andreas Zűttel, Applied physics letters, 89 (2006) 021920.

[51] S.L.S.M. John J. Vajo, J. Phys. Chem. B, 109 (2005) 3719-3722.

[52] I.A. Pablo Palacios, Perla Wahńon, and Jossé C. Conesa, J. Phys. Chem. C, 112 (2008) 9525-9529.

[53] A.S. Jun Yang, and C. Wolverton, J. Phys. Chem. C, 111 (2007) 19134-19140.

[54] M.S.M. F.E. Pinkerton, J. Alloys Compd., 464 (2008) L1-L4.

[55] T.K. Gagik Barkhordarian, Martin Dornheim, Rűdiger Bormann, J. Alloys Compd., 440 (2007) L18-l21.

[56] J.-H.S. Seon-Ah Jin, Young Whan Cho, Kyung-Woo Yi, Oleg Zavara, Maximilian Fichtner, Scripta Materialia, 58 (2008) 963-965.

[57] S.C. Ulrike Bösenverg, Lene Mosegaard, Gagik Barkhordarian, Nico Eigen, Andreas Borgschulte, Torben R. Jensen, Yngve Cerenium, Oliver Gutfleish, Tomas Klassen, Martin Dornheim, Rűdiger Bomann, Acta Mater., 55 (2007) 3951.

[58] K. M. Aoki, Miwa, T. Noritake, N. Ohba, M. matsumoto, H.-W. Li, Y. Nakamori, S. Towata, S. Orimo, Appl. Phys. A, 92 (2008) 601-605.

[59] S.-A.J. Jae-Hun Kim, Jae-Hyeok Shim, Young Whan Cho, J. Alloys Compd., 461 (2008) L20-L22.

[60] D.R. Ji Youn Lee, Young-Su Lee, Yoonyoung Kim, Yngve

Cerenium, Jae-Hyeok Shim, Torben R. Jensen, Nam Hwi Hur, Young Whan Cho, J. Phys. Chem. C, 113 (2009) 15080-15086.

[61] M.H.S. M. D. Riktor, K. Chlopek, M. Fichtner, B.C. Hauback, J. Mater. Chem. , 19 (2009) 2754-2759.

[62] D.D.G. Lin-Lin Wang, Ian M. Robertson, Duane D. Johnson, J. Phys. Chem. C, 113 (2009) 20088-20096.

[63] TOPAS version 4.1, Bruker AXS GmbH, Karlsruhe, Germany, (2003-2008).

[64] R.C.B. Son-Jong Hwang, Jr., Joseph W. Reiter, Job Rijssenbeek, Grigorii L. Soloveichik, Ji-Cheng Zhao, Houria Kabbour, Channing C. Ahn, J. Phys. Chem. C. Lett., 112 (2008) 3164-3169.

[65] Y.F. M.D. Riktor, P. Vajeeston, E.G. Bardaji, M. Fichtner, H. Fjellvag, M.H. Sorby, B.C. Hauback, J. Mater. Chem. , 21 (2011) 7188.

[66] K.C. M. Fichtner, M. Longhini, H.hagemann, J. Phys. Chem. C, 112 (2008) 11575-11579.

[67] M.A. Kazutoshi Miwa, Tatsuo Noritake, Nobuko Ohba, Yuko Nakamore, Shin-ichi Towata, Andreas Zűttel, Shin-ichi Orimo, Phys. Rev. B, 744 (2006) 155122.

[68] N.O. Kazutoshi Miwa, Shin-ich Towata, Yuko Nakamori, Shin-ichi Orimo, 2004, 69 (2004) 245120.

[69] F. Buchter, Z. Lodziana, A. Remhof, O. Friedrichs, A. Borgschulte, P. Mauron, A. Zuttel, D. Sheptyakov, L. Palatinus, K. Chlopek, M. Fichtner, G. Barkhordarian, R.d. Bormann, B.C. Hauback, Journal of Physical Chemistry C, 113 (2009) 17223-17230.

[70] Z.L. F. Buchter, A. Remhof, O. Friedrichs, A. Borgschulte, Ph. Mauron, A Zuttel, D. Sheptyakov, G. Barkhordarian, R. Bormann, K. Chlopek, M. Fichtner, M. Sorby, M. Riktor, B. Hauback, S. Orimo, J. Phys. Chem. B, 112 (2008) 8042-8048.

[71] Y. Filinchuk, E. Ronnebro, D. Chandra, Acta Materialia, 57 (2009) 732-738.

[72] K. Miwa, M. Aoki, T. Noritake, N. Ohba, Y. Nakamori, S.-i. Towata, A. Züttel, S.-i. Orimo, Physical Review B, 74 (2006).

[73] M.D. Riktor, M.H. Sørby, K. Chłopek, M. Fichtner, F. Buchter, A. Züttel, B.C. Hauback, Journal of Materials Chemistry, 17 (2007) 4939.

[74] E.R. E.H. Majzoub, J. Phys. Chem. C, 113 (2009) 3352-2258.

[75] I. Llamas Jansa, O. Friedrichs, M. Fichtner, E.G. Bardaji, A. Zuettel, B.C. Hauback, The Journal of Physical Chemistry C, (2012) 120601184214006.

[76] E. Ronnebro, E.H. Majzoub, Journal of Physical Chemistry B, 111 (2007) 12045-12047.

[77] J.-H. Her, W. Zhou, V. Stavila, C.M. Brown, T.J. Udovic, Journal of Physical chemistry C, 113 (2009) 11187-11189.

[78] S.-J. Hwang, R.C.J. Bowman, J.W. Reiter, J. Rijssenbeek, G.L. Soloveichik, J.-C. Zhao, H. Kabbour, C.C. Ahn, Journal of Physical Chemistry C, 112 (2008) 3164-3169.

[79] V. Ozoliņš, E.H. Majzoub, C. Wolverton, Journal of Americal Chemicstry Society, 131 (2009) 230-237.

[80] N. Verdal, W. Zhou, V. Stavila, J.-H. Her, M. Yousufuddin, T. Yildirim, T.J. Udovic, Journal of Alloys and Compounds, (2010).

[81] Y.-S. Lee, Y. Kim, Y. Cho, D. Shapiro, C. Wolverton, V. Ozoliņš, Physical Review B, 79 (2009).

[82] A.P.H. R. Dupree, S.C. Kohn, Chem. Phys. Lett, 276 (1997) 399-404.

[83] M. Chong, A. Karkamkar, T. Autrey, S.-i. Orimo, S. Jalisatgi, C.M. Jensen, Chemical Communications, 47 (2011) 1330.

[84] J.-H.L. Jae-Hyeok Shim, Sami-ullah Rather, Young-Su Lee, Daniel Reed, Yoonyoung Kim, David Book, Young Whan Cho, The Journal of Physical chemictry Letters, 1 (2010) 59-63.

[85] K.B. Kim, J.H. Shim, Y.W. Cho, K.H. Oh, Chem Commun (Camb), 47 (2011) 9831-9833.

[86] H. Noth, Zeitschrift Fur Naturforschung Section B-a, 37 (1982).

[87] Y. Filinchuk, B. Richter, T.R. Jensen, V. Dmitriev, D. Chernyshov, H. Hagemann, Angewandte Chemie-International Edition, 50 (2011) 11162-11166.

[88] S.R. A. Zuttel, P. Fischer, P. Wenger, P. Sudan, Ph. Mauron, Ch. Emmenegger, J. Alloys Compd., 356-357 (2003) 515-520.

[89] G.L.O. J. J. Vajo, Scr. Mater., 56 (2007) 829-834.

[90] S.Y.K. J.K. Kang, Y.S. Han, R.P. Muller, W.A. Goddard Ⅲ, Appl. Phys. Lett, 87 (2005).

[91] G.R. J.-Ph. Soulie, R. Cerny, K. Yvon., J. Alloys Compd., 346 (2002) 200-2053.

[92] P.P.E. W.Grochala, Chem. Rev., 104 (2004) 1283-1316.

[93] D.J. Siegel, C. Wolverton, V. Ozoliņš, Physical Review B, 76 (2007) 134102.

[94] Y.Z. Zi-Kui Liu, D.G. Schlom, X.X.Xi., Qi Li, Calphad, 26 (2001) 299-303.

[95] J.D.J. Sudhaker V. Alapati, David S. Sholl, J. Phys. Chem. C, 111 (2007) 1584-1591.

[96] S. Shang, T. Wang, Z. Liu, Calphad, 31 (2007) 286-291.

[97] C. Bonatto Minella, S. Garroni, D. Olid, F. Teixidor, C. Pistidda, I.

Lindemann, O. Gutfleisch, M.D. Baró, R.d. Bormann, T. Klassen, M. Dornheim, The Journal of Physical Chemistry C, 115 (2011) 18010-18014.

[98] Y. Zhang, E. Majzoub, V. Ozoliņš, C. Wolverton, Physical Review B, 82 (2010).

[99] M.S. Borislav Bogdanovic, J. Alloys Compd., 253-254 (1997) 1-9.

[100] M.L.S. Gregory P. Meisner, Michael P. Balogh, Frederick E. Pinkerton, Martin S. Meyer, J. Phys. Chem. B, 110 (2006) 4186-4192.

[101] K. Miwa, N. Ohba, S. Towata, Y. Nakamori, S. Orimo, Journal of Alloys and Compounds, 404-406 (2005) 140-143.

[102] Y.N. Shin-Ichi Orimo, Jennifer R. Eliseo, Andreas Zűttel, Craig M. Jensen, Chem. Rev., 107 (2007) 4111-4132.

[103] J. Kim, S. Jin, J. Shim, Y. Cho, Scripta Materialia, 58 (2008) 481-483.

[104] J.-H. Kim, J.-H. Shim, Y.W. Cho, Journal of Power Sources, 181 (2008) 140-143.

[105] M. Fichtner, Hydrides on the Nanoscale- physics, examples, and research direction, in: Metal hydrides (MH), Iceland, 2008.

[106] J. Lim, J. Shim, Y. Lee, Y. Cho, J. Lee, Scripta Materialia, 59 (2008) 1251-1254.

[107] M.D. Riktor, Y. Filinchuk, P. Vajeeston, E.G. Bardají, M. Fichtner, H. Fjellvåg, M.H. Sørby, B.C. Hauback, Journal of Materials Chemistry, 21 (2011) 7188.

[108] R.J. Newhouse, V. Stavila, S.J. Hwang, L.E. Klebanoff, J.Z. Zhang, Journal of Physical Chemistry C, 114 (2010) 5224-5232.

국문 초록

Ⅰ, Ⅱ족 금속 붕수소화물[$M(BH_4)_n$]은 고체 수소 저장물질로서 최근 많은 연구가 되고 있는 고체 수소저장 물질로 낮은 수소 방출온도와 높은 수소저장 밀도로 인하여 연료전지 자동차용 수소저장 물질로 유망하다. 그 중, $Ca(BH_4)_2$는 11.5 wt%, 130 kg/m^3의 수소 저장 밀도를 지니며, $Ca(BH_4)_2 \rightarrow 2/3\ CaH_2 + 1/3\ CaB_6 + 10/3H_2$와 같이 분해 되었을 때, 9.6wt%의 수소가 방출되는 것으로 보고되었다. 그러나, $Ca(BH_4)_2$의 정확한 수소 방출 반응에 대해서는 아직 알려지지 않았고, CaB_2H_x, 비정질상, $CaB_{12}H_{12}$와 같은 중간 생성물에 대해서는 아직까지 논란이 많다. 수소방출에 대한 표준 실험 조건이 없었으므로 각기 다른 실험 조건(수소압력과 온도)하에서의 수소 방출연구가 진행되었고, 이것이 $Ca(BH_4)_2$의 탈수소화 반응과 중간 생성물에 대한 논란을 야기시켰다. 따라서 본 연구에서는 수소 1 bar의 등압 상태에서 온도에 따른 $Ca(BH_4)_2$의 탈수소화 반응을 연구하고, 수소 압력에 따른 탈수소화 반응 경로의 변화에 대해서도 조사 하였다. 또한, 금속 붕수소화물과 금속수소화물의 혼합물의 경우, 수소흡수화 반응에 효과가 있다고 보고되었다. 따라서, $Ca(BH_4)_2$와 MgH_2를 균일하게 섞은 혼합물의

경우 수소 1bar에서의 탈수소화 반응과 수소화 반응에 대해서 조사하였고 본 연구의 결과는 다음과 같다.

첫째, 수소 1 bar의 등압상태에서 온도를 올리며 $Ca(BH_4)_2$의 탈수소화 반응을 연구하였다. β-$Ca(BH_4)_2$는 300℃에서 unidentified amorphous phase로 서서히 변하고, 330℃에서 이중 일부는 CaB_2H_x를 형성하고, 나머지는 $CaB_{12}H_{12}$를 형성하였다. CaB_2H_x는 더 가열하면 CaH_2와 CaB_6로 변하며, 반면에 $CaB_{12}H_{12}$는 500℃까지 안정하게 유지되었다. 따라서, ⅰ) β-$Ca(BH_4)_2$ → amorphous phase → CaB_2H_x + (8-x)/2H_2 → 2/3 CaH_2 + 1/3 CaB_6 + 10/3 H_2, ⅱ) β-$Ca(BH_4)_2$ → amorphous phase → 1/6 $CaB_{12}H_{12}$ + 5/6 CaH_2 + 13/6 H_2 의 두 반응이 1bar 등압 상태에서 경쟁적으로 일어난다는 것을 보였다. 여기서 흥미로운 것은 CaH_2+ CaB_6와 $CaB_{12}H_{12}$는 촉매 없이 역반응 즉, 수소화 반응이 수소 90 bar, 350 ℃에서 일어나지 않았지만, $Ca(BH_4)_2$의 중간 생성물인 CaB_2H_x는 수소 90 bar, 350℃에서 촉매 없이 수소화 반응이 100% 진행되었다. 따라서, 탈수소화 반응을 조절하여 두 경쟁반응에서 CaB_2H_x가 주로 형성되도록 하기 위하여, 수소 압력 변화에 따른 $Ca(BH_4)_2$의 탈수소화 반응경로 변화에 대한 연구를 진행하였다.

둘째, $Ca(BH_4)_2$의 탈수소화 반응을 수소 1bar~20bar의 범위에서 온도의 증가에 따라 연구하였고, 그 결과 $Ca(BH_4)_2$의 탈수소화 반응이 수소 압력에 민감하게 변함을 관찰하였다. 수소 1bar에서는 앞의 결과에서와 같이 반응 ⅰ), ⅱ) 두 반응이 경쟁적으로 일어났으나, 수소 압력이 증가할수록 CaB_2H_x가 형성되는 반응 ⅰ)이 감소되었다. 수소 20 bar에서는 $Ca(BH_4)_2$의 탈 수소화 반응 ⅰ)이 전혀 일어나지 않았다. 반면, 수소 압력이 5bar가 되자, ⅲ) $Ca(BH_4)_2 \rightarrow CaH_2 + 2B + 3H_2$의 탈수소화 반응이 진행되었고, 압력이 증가함에 따라 반응 ⅲ)의 비율을 점점 증가하였다. 따라서, 수소 20bar에서는 탈수소화 반응 ⅱ), ⅲ)이 일어남을 보였다.

마지막으로, $Ca(BH_4)_2$와 MgH_2의 혼합물은 $2Ca(BH_4)_2 + MgH_2 \rightarrow 1/3\ Ca_4Mg_3H_{14} + 2/3CaB_6 + 20/3\ H_2$의 경로로 분해되어 수소를 방출하고, 이 분해 생성물은 수소 90 bar 350℃의 조건에서 촉매없이 수소를 60% 재흡수하였다. 여기서 MgH_2는 $Ca_4Mg_3H_{14}$를 형성하도록 하여 탈수소화, 수소화 반응의 촉매 역할을 하였다.

따라서, 본 연구에서는 수소 등압상태에서의 $Ca(BH_4)_2$와 $Ca(BH_4)_2 + MgH_2$의 탈수소화반응에 대해 연구하였고, 수소 압력을

증가함에 따라 탈수소화 반응의 경로 변화에 대해서도 연구하였다. 또한, $Ca(BH_4)_2$와 $Ca(BH_4)_2$의 중간생성물, $Ca(BH_4)2+ MgH_2$의 분해산물에 대한 수소화 반응에 대한 연구를 통하여, 촉매 첨가제 없이 비교적 낮은 압력에서 위 물질이 수소를 재흡수 한다는 것을 보였다. 이로써 $Ca(BH_4)_2$와 $Ca(BH_4)_2+ MgH_2$이 고체 수소저장물질로서 가능성 있다는 것을 보여주었다.

핵심어: 수소저장, 칼슘 보로하이드라이드, 열역학적 조정, X-선 회절법, 적외선 분광법, 라만 분광, 탈수소화 반응, 수소화 반응, 핵자기공명 분광, 압력-성분-등온 곡선, 반트호프 방적식, 수소흡착, 수소탈착, 열분석, 방사광 X-선 회절

Student number: 2009-30147

Brief Curriculum Vitae

Yoonyoung Kim

(C.P.) +82-10-6210-0430
(E-mail) sholangju@snu.ac.kr
sholangju@gmail.com

Employment

Korea Institute of Science and Technology (KIST) High Temperature Energy Materials Center (1/2004-8/2006, 12/2007-presesnt)	Seoul 136-791 Republic of Korea Research scholar

Education

Seoul National University Department of Materials Science & Engineering (3/2009-2/2013)	Seoul 151-744 Republic of Korea Ph.D. in Engineering
Sogang University Department of Chemistry (9/2004-8/2006) (9/1998-2/2000)	Seoul 151-744 Republic of Korea M.S. in Chemistry B.S. in Chemistry

Publications (international journal)

8	**Yoonyoung Kim,** Son-Jong Hwang, Young-Su Lee, Jae-Hyeok Shim, Jin-Yoo Suh, Heung Nam Han, and Young Whan Cho, "Hydrogen Back Pressure Effects on the Dehydrogenation Reactions of $Ca(BH_4)_2$," *J. Phys. Chem. C*, 116(9) (2012) 25715-25720.
7	**Yoonyoung Kim,** Son-Jong Hwang, Jae-Hyeok Shim, Young-Su Lee, Heung Nam Han, and Young Whan Cho, "Investigation of Dehydrogenation Reaction Pathway of $Ca(BH_4)_2$, and Reversibility of Intermediate Phases" *J. Phys. Chem. C*, 116(6)

	(2012) 4330-4334
6	Jae-Hyeok Shim, Jae-Hag Lim, Sami-ullah Rather, Young-Su Lee, Daniel Reed, **Yoonyoung Kim**, David Book and Young Whan Cho, " Effect of Hydrogen Back pressure on Dehydrogenation Behavior of $LiBH_4$-Based Reactive Hydride Composites," *J. Phys. Chem. Lett.,* 1(1) (2010) 59-63
5	**Yoonyoung Kim,** Daniel Reed, Young-Su Lee, Jae-Hyeok Shim, Heung Nam Han, David Book, Young Whan Cho, " Hydrogenation reaction of CaH_2-CaB_6-Mg mixture," *J. Alloys Compd.*, *492* (2010) 597-600
4	Ji Youn Lee, Dorthe Ravnsbæk, Young-Su Lee, **Yoonyoung Kim,** Yngve Cerenius, Jae-Hyeok Shim, Torben R. Jensen, Nam Hwi Hur and Young Whan Cho, " Decomposition Reactions and Reversibility of the $LiBH_4$-$Ca(BH_4)_2$ Composite," *J. Phys. Chem. C*, *113* (33) (2009) 15080–1508.
3	**Yoonyoung Kim**, Daniel Reed, Young-Su Lee, Ji Youn Lee, Jae-Hyeok Shim, David Book and Young Whan Cho, " Identification of the Dehydrogenated Product of $Ca(BH_4)_2$," *J. Phys. Chem. C*, *113* (14) (2009) 5865-5871.
2	Young-Su Lee, **Yoonyoung Kim,** Young Whan Cho, Daniel Shapiro, Chris Wolverton, and Vidvuds Ozoliņš, "Crystal structure and phonon instability of high-temperature β-$Ca(BH_4)$," *Phys. Rev. B,* 79 (2009) 104107.
1	**Yoonyoung Kim,** Eung-Kyu Lee, Jae-Hyeok Shim, Young Whan Cho, Kyung Byung Yoon, " Mechanochemical synthesis and thermal decomposition of $Mg(AlH_4)$," *J. Alloys Compd.*, *422*(1-2) (2006) 283-287.